UNIVERISTY OF SOUTHAMPTON
Faculty of Physical Sciences and Engineering
Optoelectronics Research Centre

Interference lithography with extreme ultraviolet light

by

Kim, Hyun-Su

Dissertation for the degree of Doctor of Philosophy

2016

Interference lithography with extreme ultraviolet light

Der Fakultät für Mathematik, Informatik und Naturwissenschaften der RWTH Aachen University vorgelegte Dissertation zur Erlangung des akademischen Grades eines Doktors der Naturwissenschaften

von
M. Sc.
Kim, Hyun-Su
aus
Seoul, die Republik Korea

Abstract

Discipline

Dissertation for the degree of Doctor of Philosophy

INTERFERENCE LITHOGRAPHY WITH EXTRME ULTRAVIOLET LIGHT

Kim, Hyun-Su

In photolithography, increasing pattern density is a key issue for development of semiconductor devices. Extreme ultraviolet (EUV) radiation is the next generation light source for overcoming the resolution limit of conventional photolithography in order to obtain nanostructures of higher density. In this thesis, we focus on investigating resolution limits of interference patterns produced by EUV radiation. Optical properties of interference fringes obtained using different types of compact EUV sources are studied with regard to increasing pattern density. Rigorous simulations of optical wave propagation of EUV radiation are performed to investigate the resolution limits of interference fringes for the fractional Talbot effect, the achromatic Talbot effect, and an image of Talbot carpet that has an optical property of ever-decreasing size of interference fringes. In experiments, interference lithography has been performed with three different types of compact EUV sources including a gas discharge produced plasma, a plasma based EUV laser, and a high-harmonic generation source. We analyze optical characteristics of particular EUV sources resulting in different capabilities of patterning. Also different optical system designs capable of overcoming the limitations of optical properties of EUV radiation are investigated. We expect that the study of EUV interference lithography can be helpful for understanding the upcoming photolithography resolution and also can be useful as a technology for fabricating very fine structures.

Contents

Acknowledgments

My PhD study was not possible without the indispensable support, advice and encouragement of many people, who have contributed in various ways to the completion of this dissertation.

I would like to express my sincere gratitude to my supervisor Prof. Dr. Larissa Juschkin, who has supported me throughout my studies with her patience, passion, and knowledge. Her careful guidance helped me a lot to finish this project. I would like to express my sincere gratitude also to my co-supervisor Prof. Dr. William S. Brocklesby for his indispensable support of my studies. He helped me with his patience and knowledge to complete this dissertation.

My advisor Dr. Serhiy Danylyuk, who has enthusiasm and knowledge, was always helping me a lot. He gave me valuable advices and engaged in fruitful discussions. I indebted to the numerous members of EUV group, TOS group at RWTH Aachen University and Juelich EUV group involving particularly C. Dittberner, Sascha Brose, Aleksey Maryasov, Girum Beyene, R. Freiberger, D. Rudolf, D. Vicario, M. Tryus, D. Wilson, J. Bussmann, V. Deuter, J. Tempeler, S. Herbert, F. Melsheimer.

I indebted to my colleagues of ultrafast X-ray group in University of Southampton, particularly Peter Baksh, Michal Odstrčil, Magdalena Miszczak, Prof. Dr. Jeremy G. Frey and Dr. P. Horak for their remarkable help and support.

My sincere gratitude also goes to Prof. Dr. Peter Loosen, and Dr. Klaus Bergmann for their special supports at the Fraunhofer Institute for Laser Technology.

I wish to acknowledge people from Helmholtz Nano-Facility in Juelich research center, who provided me with technical support. Particularly I would like to thank to Dr. Elmar Neumann for his remarkable help.

My PhD project was supported by the Education, Audiovisual and Culture Executive Agency (EACEA) European Union Erasmus Mundus Joint Doctorate Programme (FP7 FPA-2012-0033, EXTATIC). I would like to thank to all the people of EXTATIC, which gives me a special sense of belonging, particularly my cohort. I also acknowledge that my PhD study was partially supported by European cooperation in science and technology (MP1203).

My special thank goes to my advisor Prof. Mario C. Marconi, Prof. Jorge Rocca, Prof. Carmen Menoni, and Wei Li from Colorado State University, who provided amazing support, help, and discussion.

I would like to thank Prof. Hye-keun Oh, who has supervised my master thesis in Hanyang university, where I started my graduate studies.

I would like to thank my thesis committee involving Prof. Carsten Honerkamp (RWTH Aachen) agreed to chair my PhD exam, Prof. T. Taubner (RWTH Aachen), Prof. L. Juschkin, Prof. D. Shepherd (Univ. of Southampton), Dr. Y. Ekinci (Paul Scherrer Institute).

Last but not least, none would have been possible without love and patience of my family: my father Seung-Bea Kim, my mother Sung-Su Jin, and my sister Hyun-Jin Kim. I would like to thank to my grandfather Su-Min Kim for his endless support.

Thank you very much to everyone.

Hyun-Su Kim
Aachen, 2016

Definitions/Abbreviations

AFM: atomic force microscope

CD: critical dimension

CCD: charge-coupled device

CW: continues wave

DLW: direct laser writing

DOF: depth of field

DPP: discharge produced plasma

EBL: electron beam lithography

EMF: electromagnetic field

EUV: extreme ultraviolet

F-K: Fresnel-Kirchhoff

FDTD: finite difference time domain

FFT: fast Fourier transform

FIB: focused ion beam

FWHM: full width at half maximum

HHG: high harmonic generation

HVM: high-volume manufacturing

IL: interference lithography

LER: line-edge roughness

LPP: laser produced plasma

ML: multilayer

MSDS: material safety data sheet

M_{sf}: spatial frequency multiplication

NA: numerical aperture

N_F: Fresnel number

OPC: optical proximity correction

OPD: optical path difference

Pitch: spatial period of fringes

Resist: photoresist

RS: Rayleigh-Sommerfeld

SEM: scanning electron microscope

TE: transverse electric polarization

TM: transverse magnetic polarization

z_T: Talbot length

Introduction

Review of the Background

The fabrication of small structures of integrated circuits (IC) is a key technology in the semiconductor industry. IC is a compact set of electronic circuits, which is composed of individual electronics components, such as transistors, capacitors, or diodes on one small plate (chip). During past decades, there has been a rapid growth of the technologies focused on high circuit integration in small silicon pieces. Moores's law has predicted that the density of transistors and computing power doubles every two years. Photolithography is a key technology to realize his predictions until the time that quantum physics may define a future limit of electronic miniaturization and ever-increasing computing power [1965 Moore, 2008 Powell].

Semiconductor device fabrication is the process used to create the ICs. The first IC was printed using contact lithography, i.e. the image to be printed is obtained by illumination of a photomask in contact. The fundamental limit to the resolution that can be obtained when light is propagating through gratings is achieved in the evanescent near field regime of a grating with finite thickness. Sufficient intensity and contrast exists for periods down to λ/20, indicating that the evanescent near field is ripe to be harnessed for low-cost nanolithography [2000 Mcnab].

Since contact lithography has defect and contamination issues, instead, proximity lithography is used. It has lower resolvability due to the image blur by diffraction at a certain gap distance from the mask. The resolution of proximity lithography is given by:

$$Res \propto \sqrt{g \cdot \lambda} \tag{01}$$

where g is the proximity gap, λ is the exposure wavelength.

Projection lithography

The fabrication of very-large-scale integration (VLSI) circuit is performed with projection lithography systems. A photomask covers an entire field, which is imaged onto the wafer in a single exposure or scanning procedure. The fundamental limit of the resolution of an optical projection exposure tool is given by:

$$CD = k1\frac{\lambda}{NA} = k1\frac{\lambda}{n \sin\theta} \tag{02}$$

CD is critical dimension that is generally twice the half-pitch (period), k1 is called a process factor (typically k1 > 0.25), NA is the numerical aperture of the lens given by n·sinθ, n is the refractive index of the medium, θ is half of the opening angle (angular aperture) of the lens. Depth of focus (DOF) is given by the following [2007 Mack, 2010 Levinson]:

$$DOF = \pm k2 \frac{\lambda}{NA^2} \tag{03}$$

where k2 is another process factor of lithography.

In order to improve the resolution limit, projection lithography has been developed with radiation of shorter wavelengths. Fig. 01 shows the trend in the wavelength of radiation used to reduce the feature size [2010 Tallents]. The light production tool has changed from conventional lamps and lasers to high temperature emitting plasmas. Gas-discharge lamps using mercury (Hg) produce radiation with a broad spectrum with several strong peaks in the ultraviolet (UV) range. From the early 1960s through the mid-1980s, Hg lamps have been used in lithography for their spectral lines at 436 nm (g-line), 405 nm (h-line) and 365 nm (i-line) for resolution down to 200 nm.

Excimer lasers were used after the i-line lithography had reached the resolution limit. Krypton fluoride (KrF) laser with wavelength of 248 nm and argon fluoride (ArF) laser with the wavelength at 193 nm are used in consecutive order. The F_2 laser with wavelength of 157 nm was not suitable to follow the KrF laser owing to several optical issues. Instead, the ArF 193 nm immersion lithography is used, which can reduce the resolution by increasing NA. Recently, extreme ultraviolet (EUV) systems have been considered as a follow up to ArF immersion lithography for the next step.

Maskless lithography

Maskless lithography is used to fabricate masks for mask-based lithography such as contact, proximity, projection, and Talbot lithography. In maskless lithography, the radiation is focused to a narrow beam. The beam writes the image onto the photoresist directly. Maskless lithography includes electron beam (e-beam) lithography, direct laser writing (DLW), focused ion beam (FIB), dip-pen nanolithography, and multi-beam interference lithography. Non-photon/non-particle based maskless lithography includes nanoimprint lithography (NIL), or directed self-assembly (DSA).

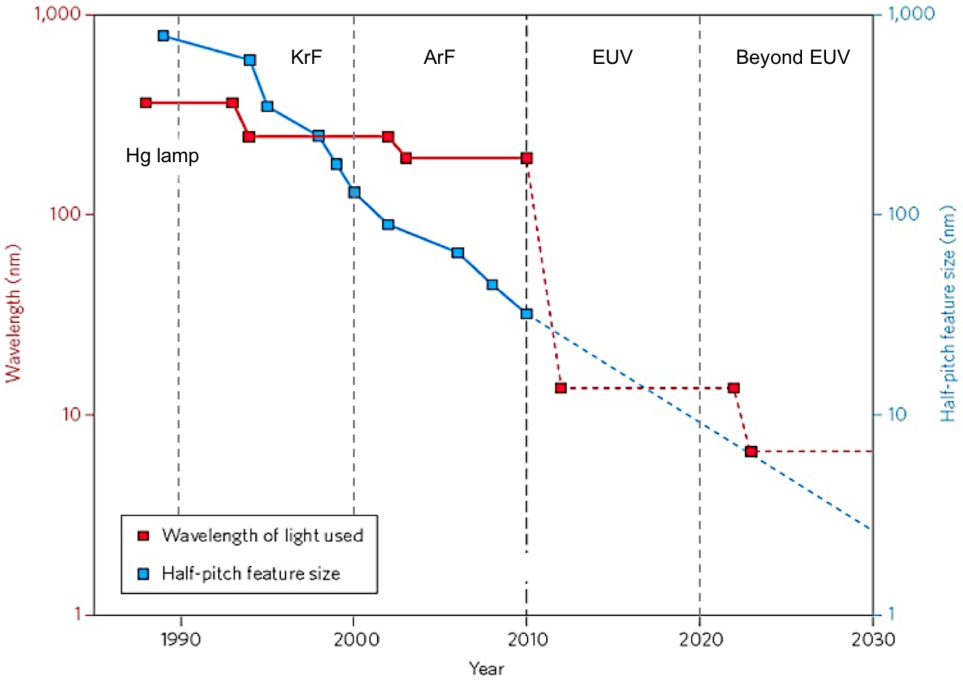

Fig. 01 Lithography trend showing the improvement of resolution by reducing the wavelength of the light over the past and future [2010 Tallents]

X-ray lithography

At the end of the XXth century, one of the most promising alternatives was x-ray proximity lithography using wavelengths below 1 nm [1997 Cerrina]. With this short wavelength, the influence of the diffraction limit on resolution is negligible and high-resolution patterns are possible. Further reduction of the wavelength was found to be ineffective due to increased photoelectron blur in photoresist [1993 Guo, 1995 Okazaki]. Unfortunately, with this method, no demagnification with lenses is possible, and mask to wafer distance should be kept at sub-μm level in order to achieve sub-30 nm resolution. Due to these strong challenges and rapid development of the immersion lithography, this technology has not progressed past the pre-production state. However, during the last decade, it was shown that it is possible to improve resolution of the proximity printing utilizing Fresnel diffraction of short wavelength radiation [1999 Vladimirsky]. This allows the achievement of sub-30 nm resolution with mask to wafer gap reaching 30 μm, which is much more feasible in an industrial environment.

EUV Lithography

Despite numerous forecasts claiming that optical lithography will soon hit its limit, the industry so far successfully managed to overcome apparent barriers by continuous reduction of wavelength of the radiation, increase of the numerical aperture (NA) of lithography systems, and implementation of multiple patterning techniques.

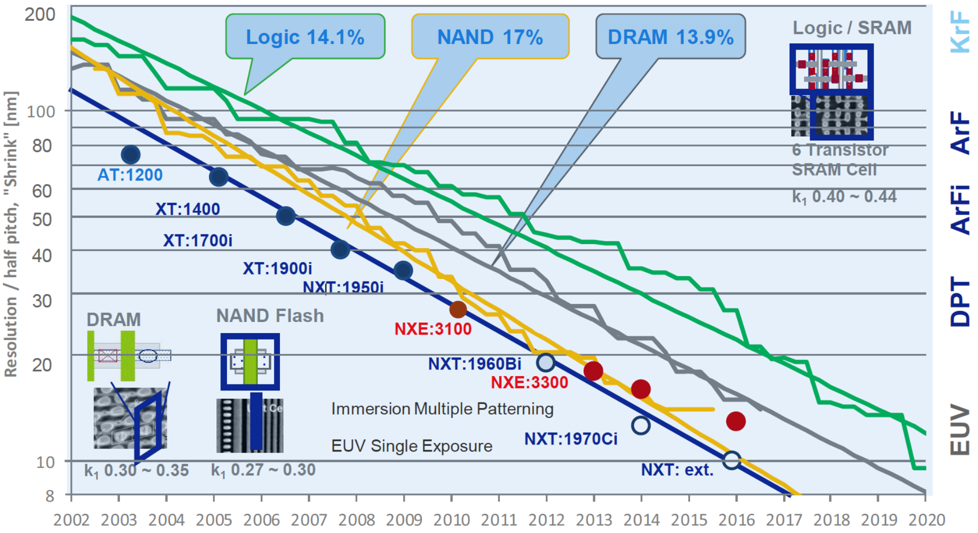

Fig. 02 Industry roadmap towards sub 10 nm resolution [2013 Peeters]

The next step in the development history of the optical lithography is a radical reduction of the wavelength from current 193 nm to 13.5 nm, which should enable scaling below 10 nm half-pitch levels [2013 ITRS]. This radiation lies in the so-called extreme ultraviolet (EUV) wavelength range, where photon energy is significantly higher and, as a consequence, the interaction mechanisms between light and matter differ from well-studied ultraviolet radiation [2010 Tallents, 2010 Wagner]. Fig. 02 shows the presentation of the industry roadmap towards sub 10 nm resolution with EUV technology [2013 Peeters].

Beyond the technical challenges which are induced by the wavelength change, such as development of high power radiation sources and high efficiency optical systems and defect-free masks, a major hurdle for reaching sub 10 nm resolution is the need to develop resists that would demonstrate simultaneously high-resolution, low line-edge roughness and high sensitivity [2008 Gallatin].

EUV-IL

To support the development of EUV lithography, EUV interference lithography (EUV-IL) is very useful method. In contrast to usual exposure tools, where the resulting aerial image is a demagnified image of a mask and strongly influenced by mask defects and errors in the optical system, in EUV-IL the whole area of the mask contributes to every point in the aerial image, enabling predictable intensity profiles. This allows for investigation of pure resist properties all the way down to a quarter of the illumination wavelength, well into the sub 10 nm region.

Typical parameters of nanofabrication methods

It is important to use the proper technique for the specific purpose because most of techniques have their own advantages and disadvantages among other techniques. For example, e-beam lithography is useful for precise single device fabrication and projection lithography is proper for high volume manufacturing. IL has an advantage in production of periodic structures over a large area. It requires only simple optical devices to achieve high-density structures on photoresists. The following table roughly compares the advantages and disadvantages of popular nanofabrication techniques. The comparison is made with regards to the following parameters including: 1st Shaping – the method can print complex structures or only simple periodic patterns, 2nd Throughput – method prints large field in a single exposure for the high volume manufacturing (HVM), 3rd Resolution – pitch of patterns or density of structures, 4th Material – the method can print on variable materials or only on photoresists, 5th Usability – the method is easy to utilize, 6th Maskless – the method can write the feature itself or support of master objects required, e.g. photomask.

	ebeam Litho	**FIB**	**UV DLW**	**coherent EUV-IL**	**plasma EUV-IL**	**nano-imprint**	**EUVL**
Shaping	☺	☺	☺	😐	☹	☺	☺
Throughput	☹	☹	😐	😐	😐	☺	☺
Resolution	50 nm	10 nm	10 µm	10 nm	50 nm	20 nm	10 nm
Material	😐	☺	☺	😐	😐	😐	😐
Usability	😐	☺	☺	😐	☺	☺	☹
Maskless	☺	☺	☺	😐	😐	☹	😐

Table 01 Strengths and weaknesses of nanofabrication methods for IL: Resolution is roughly estimated. (*DLW: direct laser writing)

Motivation and scope

In photolithography, increasing pattern density is a key issue for improving performance of semiconductor devices. Utilizing extreme ultraviolet (EUV) radiation is the next step to overcome the resolution limit of conventional photolithography in order to obtain patterns of higher density. This thesis focuses on investigating optical properties and resolution limits of interference patterns produced by EUV radiation.

Rigorous simulations of optical wave propagation of EUV radiation are performed to investigate the resolution limits of interference fringes for the fractional Talbot effect, the achromatic Talbot effect, and the image of Talbot carpet that has an optical property of ever-decreasing size of interference fringes.

In experimental demonstration, interference lithography is demonstrated utilizing three different types of compact EUV sources. The 1st one is a Xenon gas discharge plasma (DPP) generating light of wavelength at around 11 nm. The 2nd one is a highly coherent EUV source of wavelength at 46.9 nm generated by a capillary discharge Ne-like Ar laser. The 3rd one is a short pulse EUV source of wavelength at 29 nm, generated by a high-harmonic generation (HHG). We analyze optical characteristics of particular EUV sources resulting in different capabilities.

Particular optical designs of interference lithography capable of overcoming the limitations of optical properties of particular EUV radiation are investigated. Contact lithography, proximity lithography, and quasi-monochromatic Talbot lithography are demonstrated with a DPP source having quasi-broadband EUV spectrum. Coherent Talbot lithography is demonstrated with the EUV laser for fractional Talbot effect. And Lloyd's mirror interference lithography is demonstrated with the HHG source. Also transmission mask fabrication techniques for mask based Talbot lithography are demonstrated in experimental demonstrations.

We expect that interference lithography can be useful for fabricating very fine structures in order to meet current and future requirements of lithography trends.

Chapter 1

EUV Radiation for Interference Lithography

1.1 THEORETICAL REVIEW: OPTICAL PROPERTIES OF EUV LIGHT

Extreme ultraviolet light

The extreme ultraviolet (EUV or XUV) is an optical region of the electromagnetic spectrum in the wavelength range from around 5 nm to 50 nm, with corresponding photon energy[§] from around 25 eV to 250 eV (Fig. 1.1.1). EUV light is highly absorbed by most states of matter including gas, solid, liquid, and plasma, requiring a vacuum environment in the whole optical system [1999 Attwood].

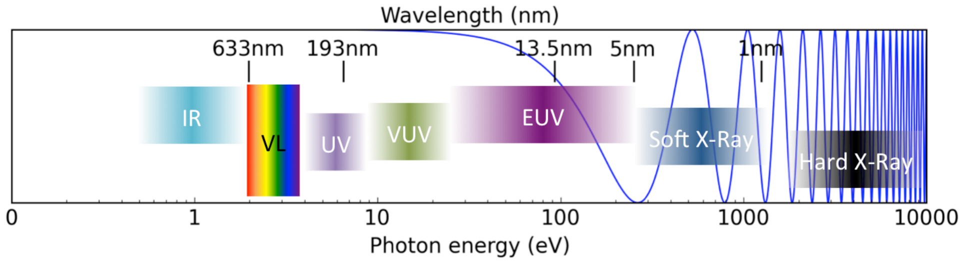

Fig. 1.1.1 The optical region of the electromagnetic spectrum

Due to its strong interaction with matter and its short-wavelength nature, EUV radiation is used for applications of high-resolution imaging or photolithography.

The index of refraction

The complex refractive index slightly deviates from unity in the EUV range; the form "1-δ+$i\beta$" is commonly used instead of the traditional form "n+$i\beta$" as shown in the following equation:

$$n = n + i\beta = 1 - \delta + i\beta \qquad (1.1.1)$$

where the real part is associated with the phase velocity, and the imaginary part is the extinction coefficient that determines attenuation, which is associated with the amount of intensity attenuation when electromagnetic wave propagates through matters. The δ and β

[§] $\hbar\omega \cdot \lambda = hc = 1239.842\ eV\ nm, 1\ J = 5.034 \times 10^{15} \lambda[nm] photons$

can be derived from the complex atomic scattering factor, $f^{0}(\omega)$[**] [1999 Attwood], and are given by:

$$\delta = \frac{n_a r_e \cdot \lambda^2}{2\pi} \cdot f_1^0(\omega)$$
$$\beta = \frac{n_a r_e \cdot \lambda^2}{2\pi} \cdot f_2^0(\omega) \tag{1.1.2}$$

where n_a is the atomic number density (atoms per unit volume), r_e is the classical electron radius. The complex atomic scattering factors can be found in [1993 Henke].

The refractive index strongly depends on the frequency of electromagnetic wave near the natural resonant frequencies of the electron's oscillation (ω_s) in extreme ultraviolet range. The refractive index is used for the diffraction image calculation, e.g. of diffraction grating masks composed of multiple thin layers of membrane or absorbers.

[**] The complex atomic scattering factor: $f^0(\omega) = f_1^0(\omega) + if_2^0(\omega)$

Attenuation length of solid layers

For the fabrication of transmission masks, the material can be chosen in consideration of attenuation length at particular wavelength of light, see Fig. 1.1.2. The typical binary amplitude transmission mask is efficient when absorber part blocks and substrate transmits more light, whereas a phase shift mask requires higher light transmission. For example, using radiation with wavelength around 29 nm, materials with attenuation length of below 10 nm such as gold (Au), tungsten (W), and niobium (Nb) are good candidates as an absorber. And for the substrate of the mask, Si with thickness of 100 nm is a good candidate.

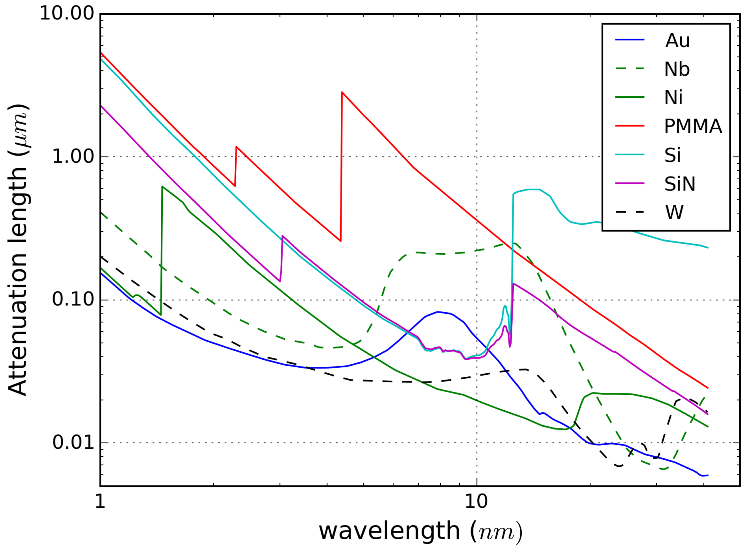

Fig. 1.1.2 Absorption in solids for EUV and soft x-rays [1993 Henke]

Reflectivity of thick mirrors

In the EUV range, reflectivity is very low for grazing incidence angles higher than 30 degrees for all materials. Therefore, the wavelength range is very narrow for choosing suitable materials for optical components such as mirrors, membranes, and absorbers. Fig. 1.1.3 plots the reflectivity of a thick mirror for several materials as a function of grazing angle with s-polarized light of around 29 nm wavelength.

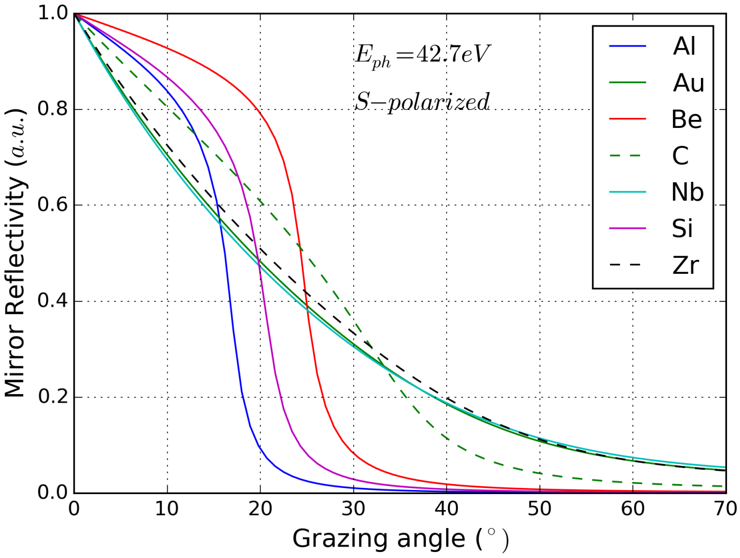

Fig. 1.1.3 The reflectivity of a thick mirror for radiation with wavelength at 29 nm, which depends on angle and materials, calculated using optical constants [1993 Henke]. (Note that Beryllium (Be) is highly toxic.)[††]

Coherence of EUV radiations

Table-top EUV sources differ in their beam characteristics from each other. One of the key characteristics for the successful demonstration of interference lithography is coherence of radiation. The dictionary defines coherence as the quality of being well-organized and consistent, or the quality of forming a unified whole. In optics, coherence of light is defined as the degree of the correlation between states of phases. Interference fringes can be formed when the phases of two electromagnetic waves are stationary over time. The degree of coherence can be determined from the visibility of interference fringes. Coherence has to be considered both in space and in time, which are called spatial and temporal coherence respectively.

In the direction of propagation, temporal (longitudinal) coherence describes sustainability of phase relationships. One can define a coherence length as the distance that the wave of wavelength λ travels in phase correlation with the spectrally shifted wave, λ+Δλ [1999 Attwood]:

[††] Nanomaterial environmental, health, and safety research should be communicated efficiently to the government, regulatory or industrial decision making process through peer reviewed publications, workshops and conferences. [2014 Seal]

$$l_{coh} = N\lambda = \frac{\lambda^2}{2\Delta\lambda} \tag{1.1.3}$$

A large number of waves, N=λ/(2Δλ) travelling coherently, is obtained by the narrow spectral width (Δλ).

Spatial (transverse) coherence is related to the finite source size and divergence of the radiation. In this case, phase correlation in planes orthogonal to the direction of propagation is described. Full spatial coherence can be obtained by a spherical wave-front generated from a point source. We can obtain a simple estimation based on Heisenberg's uncertainty principle, $\Delta x \cdot \Delta p \geq \hbar/2$, where Δx and Δp are the uncertainties in position and in momentum respectively. For small angles, $\Delta p = \hbar k \Delta\theta$, where Δθ is transverse to k. And the estimation is given by:

$$d \cdot \theta = \lambda/2\pi \tag{1.1.4}$$

where d is a Gaussian beam $1/\sqrt{e}$ diameter (~0.6) and θ is the Gaussian beam half angle [1985 Attwood]. One prefers to introduce spatial coherence length rather than angle, θ. If the condition of $l_{transverse} \sim z \cdot \theta$ is satisfied, where z is the distance between an observer and the source, the coherence length is given by:

$$l_{transverse} = \frac{z\lambda}{2\pi d} \tag{1.1.5}$$

All sources generate radiation of space-angle product larger than this [1999 Attwood]. Largely incoherent radiation is often spatially and spectrally filtered for applications that required a high degree of coherence. A pinhole or a slit filter is used to obtain spatially coherent radiation and to remove aberrations of optical components. A color filter is used to attenuate unwanted wavelengths, thus providing temporally coherent radiation. The complex degree of coherence of spatially incoherent radiation is described by the van Cittert-Zernike theorem that the propagation of a wave of a finite sized source to the image plane is considered precisely to estimate spatial coherence [2003 Wolf, Appendix].

1.2 COMPACT EUV SOURCES

Compact-size sources generating EUV light are summarized in this section. Large-scale electron accelerating facilities such as synchrotrons, free electron lasers (FEL) are out of the scope in this thesis. Instead, we consider three different types of compact EUV sources including a plasma-based source, a plasma-based laser source, and a high harmonics source. We expect that sources generating with high-degree of coherence are required for applications utilizing interference effects. When we determine the coherence of the source, we have to consider the whole optical system of the source because there are techniques to make the beam coherent.

At first, the coherence of the plasma pinch has to be taken into account. The hot-dense plasma generates mostly broadband spectrum due to the various ionization states and their exited transitions. Particularly, the atoms of high-z number emit EUV radiation with a large number of ionization states and transitions resulting in a broadband spectrum. However, for atoms of low-z number the spectrum is characterized rather by line emission than a broad continuum. A plasma based EUV laser emits radiation with high degree of coherence. The coherence properties of EUV radiation generated by a high harmonics generation source depend on the optical properties of incident laser. Both the coherent and partially coherent illumination can be used for interference lithography depending on various techniques.

Plasma based EUV sources

A plasma is a gas that has been ionized. Plasma emits radiation widely from the deep UV (DUV) to visible, e.g., the low-pressure gas discharge lamps such as the fluorescent tube, or high-pressure lamps such as the xenon arc lamp. Hot-dense plasmas composed of multi-charged ions and electrons are able to emit radiation with high photon energies up to EUV and soft X-ray range. The light emission from plasma consists of a broad continuum and narrow emission lines as shown in Fig 1.2.1 [1999 Attwood]. A broad continuum is given by free electrons accelerated by ions (bremsstrahlung) and recombination between ions and free electrons. Narrow line emission is given by bound-bound transitions in the ions of various charge states (L-shell, K-shell, M-shell…)[♯]. The emitted radiating power (P_{Rad}) of a plasma contains contributions of bremsstrahlung radiation (P_{Br}), recombination radiation (P_{Rec}), and line radiation (P_{Line}):

$$P_{Radiation} = P_{Line} + P_{Recombination} + P_{Bremsstrahlung} \tag{1.2.1}$$

Two basic methods to obtain the hot-dense plasma that can emit EUV radiation include a laser-produced plasma (LPP) and a discharge-produced plasma (DPP). Xenon and Tin are widely used as target materials (fuel) for both methods.

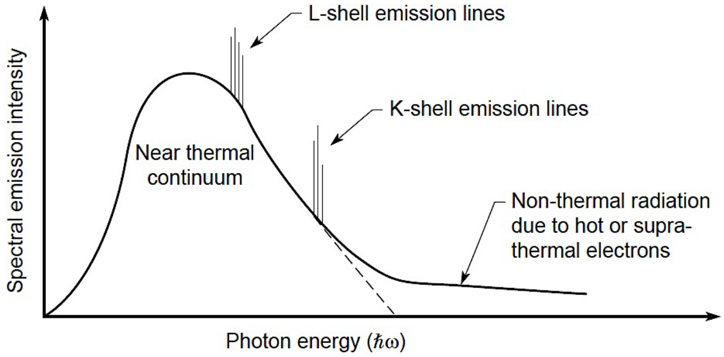

Fig. 1.2.1 Line and continuum radiation from a hot dense plasma. Highly ionized ions with outer-shell transitions in XUV [1999 Atwood]

The laser-produced plasma (LPP) uses inverse Bremsstrahlung, which is the absorption mechanism utilized to transfer energy from the incident laser to plasma. The target material is heated and evaporated by the intense focused laser pulse resulting in plasma of optimum density and temperature for emitting EUV radiation. The size of plasma from LPP is small due to the focused laser beam, which leads to high brilliance of EUV radiation.

[♯] Bremsstrahlung (free-free transitions): Free electrons are accelerated in the Coulomb potential of ions and emit radiation due to the accelerated movement.

Recombination radiation (free-bound transitions): Free electrons are attracted by the coulomb potential of the ions and recombine. The released bound energy is delivered to recombination radiation.

Line radiation (bound-bound transitions): Bound electrons emit line radiation by transition from upper to lower energy level. The wavelength of the emitted line radiation depends on the involved exited levels and the ionization degree of the emitting atom.

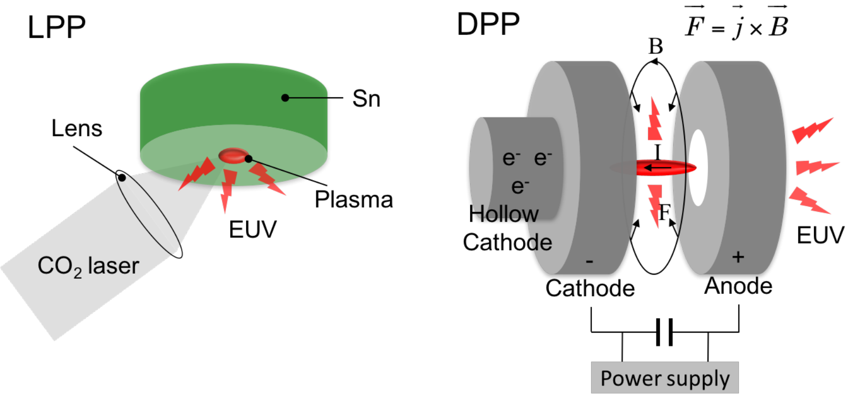

Fig. 1.2.2 Plasma based EUV sources: (LPP) laser-produced plasma and (DPP) discharge-produced plasma

The DPP operates with discharges of gases such as O_2, N_2 or Xe. A high voltage (typically 1-10 kV) across two electrodes leads to an electrical breakdown in the low-pressure gas. The current between the two electrodes produces a magnetic field. The low temperature plasma becomes gradually hotter by the magnetic pinching effect, where pinching is the compression of ions and electrons (plasma) by the magnetic force (F). The compression results in increase of density and temperature, where the plasma will be populated by ions emitting EUV radiation. In Fig. 1.2.2, the basic schemes of the LPP and the DPP are illustrated. The plasma is ionized up to around 11 times e.g. Xe^{11+}. Fig. 1.2.3 plots the data of EUV spectra produced by the DPP source in the Fraunhofer institute for laser technology with different gases. Broad continuum and line emission are seen, as discussed [2009 Bergmann].

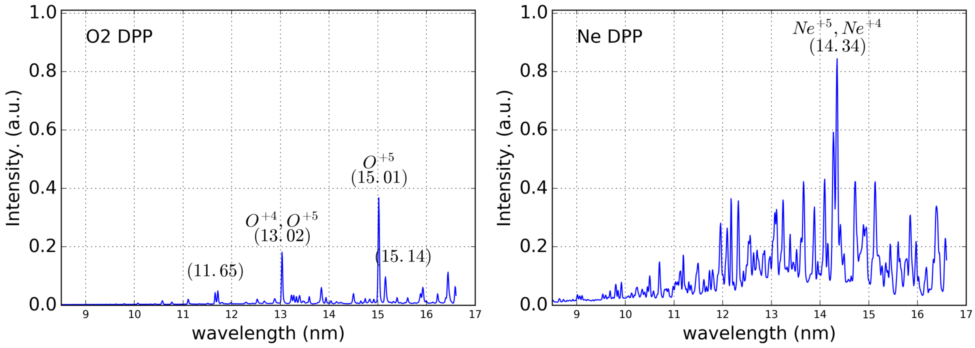

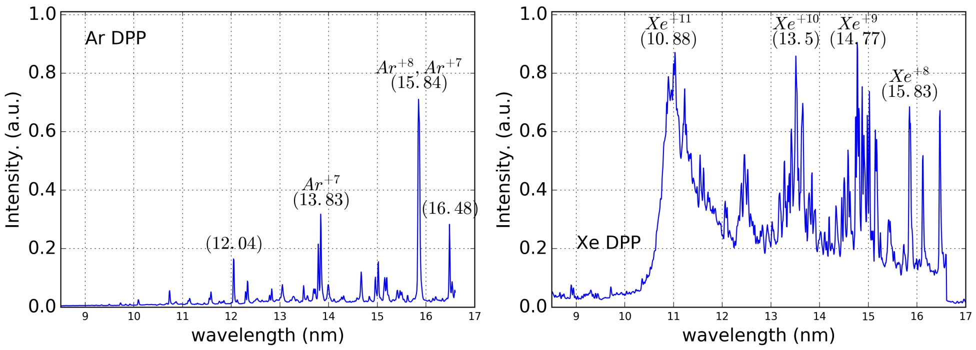

Fig. 1.2.3 EUV Spectrum emitted by DPP with different gases

A capillary discharge EUV Laser

A laser is a device that uses stimulated emission to generate or amplify the radiation. Stimulated emission is the process by which an incoming photon of a specific frequency can interact with an excited atomic electron, causing it to drop to a lower energy level. Lasing in the EUV spectral range is obtained in highly ionized plasmas that can be created in a gas filled capillary discharge (e.g. argon) [1998 Benware, 1999 Macchietto]. Capillary discharge plasma utilizes a several centimeters long capillary made of resistant material.

The discharge-pumped EUV laser benefits from the efficient deposition of electrical energy into a plasma. The discharge plasma in the capillary is compressed by electromagnetic force, resulting in a dense, narrow line plasma, in which lasing is generated in transitions of Ne-like Ar ions (Ar^{8+}). This laser operates at a wavelength of 46.9 nm and the average power is around 1mW operating at repetition rate of up to 10 Hz [2006 Rocca]. The pulse duration of the beam is 1.2 – 1.8 ns. The narrow line-width of the spectrum, $\Delta\lambda/\lambda \approx 3.5\times10^{-5}$, corresponds to a coherence time of ~ 2 ps [1997 Marconi, 2001 Liu, 2012 Urbanski].

High Harmonic Source with a femtosecond laser

Atoms driven by the strong electric field of a laser can produce coherent harmonic radiation. High-order harmonic generation (> 5 harmonics) in an atomic gas ionized by a femtosecond laser pulse has been successful for generating coherent extreme-ultraviolet radiation. The high harmonic generation source is a tunable EUV source synchronized with the driving laser and produced with the same repetition rate. The pulse duration of the envelope of the harmonics, and the spatial coherence are similar to those of the laser.

HHG can be explained with a three-step model describing the response of a single atom in a strong laser field. The binding potential of the atom is suppressed by the linearly polarized electric field allowing for an electron to tunnel out of the barrier. Then the free electron is accelerated away from the atom and back again by the electric field of the laser. And the electron recombines with the ionized atom emitting radiation.

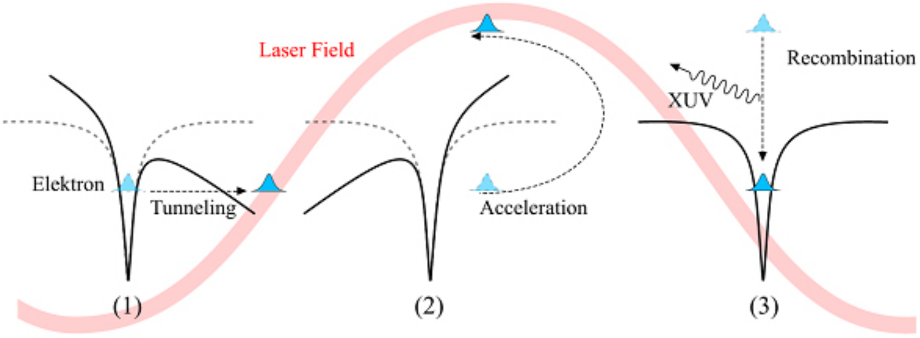

Fig. 1.2.4 Three step model of high harmonics generation process: (1) Tunneling, (2) Acceleration, and (3) Recombination [2014 HZB]

The properties of high-harmonics depend on properties of driving laser. The breadth of the harmonic spectrum extends to a cutoff harmonic at a photon energy equal to:

$$(\hbar\omega)_{max} \cong I_P + 3.2U_P \tag{1.2.2}$$

where I_P is an ionization potential of atom, U_P is the laser cycle-averaged kinetic energy of the electron. U_P is called ponderomotive potential for the laser field (E_0) at frequency (ω_0), or for the laser field intensity (I_L), and the classical electron radius (r_e):

$$U_P = \frac{e^2E_0^2}{4m\omega_0^2} = 2\pi c r_e I_L/\omega_0^2 \tag{1.2.3}$$

A well-established HHG can be based on Ti:Sapphire chirped pulse amplifiers delivering several-milli-Joule, femtosecond pulses (10-50 fs) with several kilohertz repetition rate with the tunable incident laser of around 800 nm wavelength. The application to interference lithography, which requires the field area around (50 μm)^2 illuminated with the intensity of more than a few μJ/cm^2/pulse, can be realized [2011 G.-Jacob].

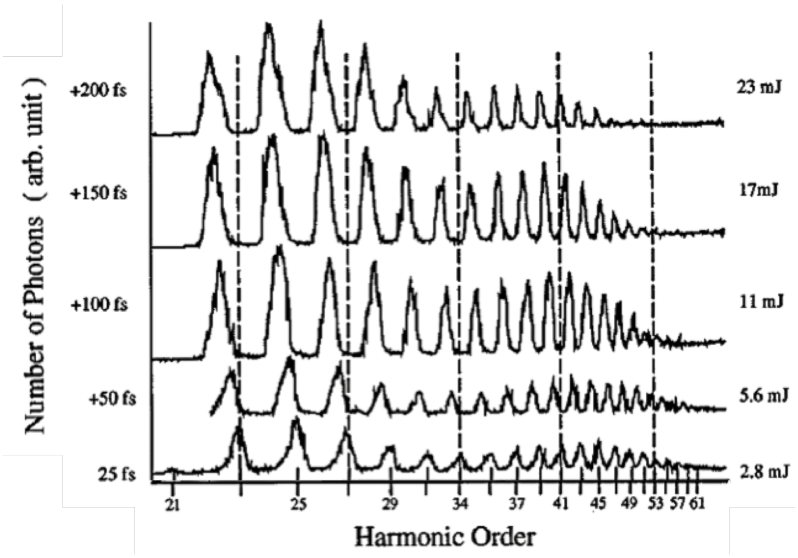

Fig. 1.2.5 Harmonic spectra generated in Ar gas with laser intensity of 5×10^{14} W/cm^2 and for various laser pulse chirps [1996 Zhou]

Typical parameters of compact EUV sources

The three different types of compact EUV sources have their own advantages with regard to pulse energy, temporal-/spatial- coherence, pulse duration, divergence, or available wavelength range. The following table consists of roughly estimated parameters of the LPP (tin), the gas based DPP (xenon), the capillary discharge EUV laser (argon), and the gas-cell based HHG source (argon).

Parameter	LPP	DPP	EUV Laser	HHG
$Ø_{\mathrm{PLASMA}}$	50-100 μm	100-500 μm	100-200 μm	5-20 μm
$\mathrm{duration}_{\mathrm{PULSE}}$	0.1-50 ns	10-1000 ns	2 ns	20-100 fs/envelope ~0.3 fs/harmonic
$L_{\mathrm{COHERENCE}}$ (at sample)	20 μm	10 μm	300 μm	150 μm
divergence	$\Omega=2\pi/4\pi$	$\Omega=2\pi$	1 mrad	1 mrad
pulse energy	0.1-1 J/pulse	1-10 J/pulse	50 μJ/pulse	1 μJ/pulse
stable rep.rate **max. rep.rate**	10 kHz 50 kHz	2 kHz 40 kHz	4 Hz 10 Hz	1kHz 1MHz
$\lambda/\Delta\lambda$	~10^1@13.5 nm (Sn droplet)	~10^2@11 nm (Xe/Ar)	~10^4@47 nm (Ar, capillary)	~10^3@29 nm (a harmonic)

Table. 1.2.1 Typical parameters of compact EUV sources (Note that parameters are only approximated, and the values are design and application dependent.)

Chapter 2

Reflective Interference Lithography

2.1 EUV INTERFERENCE LITHOGRAPHY

2.1.1 INTRODUCTION

Interference lithography (IL) is a technique for patterning regular arrays of fine structures over a large area. It is also called holographic lithography sharing the basic principle, which is to record the interference pattern formed by two or more coherent light waves on a photo-sensitive material. IL has been performed with radiation for a wide spectral region including X-rays [1994 Wei], UV [2013 Wathuthanthri, 2015 Miyazaki], VUV (Vacuum-UV) [1974 Bjorklund, 1989 Tatchyn], and recently EUV [1999 Solak]. The structure density of the array is dependent on the wavelength. However, the attempts with X-rays are limited due the edge blurring effect in the photoresist [1995 Okazaki]. Instead, EUV radiation is utilized successfully and has demonstrated sub 20 nm resolution with an undulator source (EUV-IL) [2015 Mojarad].

EUV-IL aims to fabricate sub 50 nm patterns depending on the source's characteristics. EUV-IL has been performed in several schemes such as IL with reflective beam splitters [1999 Solak, 2007 Ritucci, 2007 Wachluak], IL with diffraction gratings, and IL with Talbot effects [1996 Solak, 2015 Mojarad].

2.1.2 REVIEW OF TWO BEAM INTERFERENCE LITHOGRAPHY

The basic concept of two-beam interference lithography is illustrated in Fig. 2.1.1. The interference fringes are obtained when the interaction of the reflected wave with the direct wave alternates between constructive and destructive interference at an observation plane. Two coherent plane waves with the transverse electromagnetic (TE) polarization are incident on a photoresist layer. The two beams interfere during the pulse duration of each pulse. When the pulse duration is in the range of nanoseconds to picoseconds, a quasi-continues wave (CW) approximation is applied for the micro-scale field of interference area. If the radiation has pulse duration below 100 fs, precise arrangements are required in the demonstration of interference lithography.

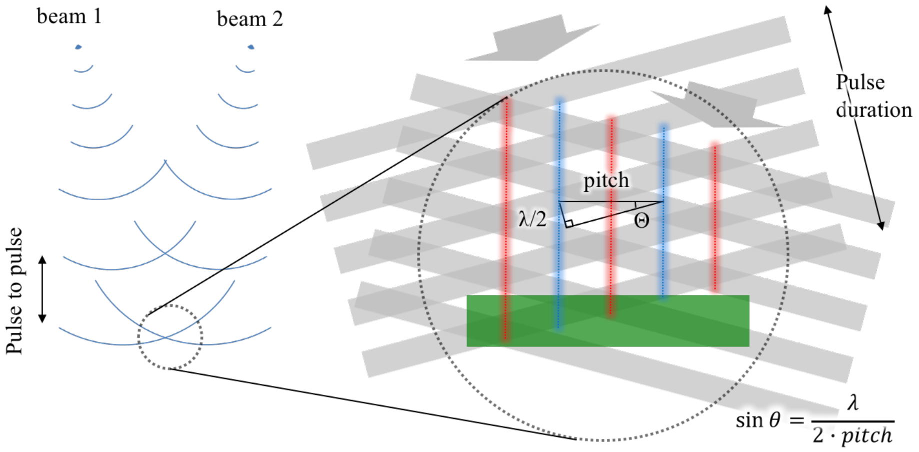

Fig. 2.1.1 Schematic of the two beams interference lithography with pulsed beams

The pitch (period) of the interference fringes is dependent on the angle between two beams of the monochromatic radiation:

$$pitch = \lambda / 2 \sin(\theta_1 + \theta_2) \tag{2.1.1}$$

where the θ_1 is a half-angle of direct beam, and θ_2 is a half-angle of reflected beam both from normal angle of photoresist plane[§§]. The minimum pitch is a half of the wavelength in theory. The number of pitches (N) is limited by temporal coherence of the incident beam given by:

$$N \leq \lambda / \Delta\lambda \tag{2.1.2}$$

owing to the phase delay of a wave interacting with another wave. In the case of the Llyod's mirror scheme, the reflected wave is delayed compared to the direct wave. In the case of a symmetric two beam interference scheme from a point source, the phase will be delayed as a function of the distance from the center of interference area.

The intensity profile of the interference fringes with the two partially coherent light beams is given by as following:

$$I = I_1 + I_2 + 2\sqrt{I_1 I_2} \cdot Re[\gamma_{12}(\tau)] \tag{2.1.3}$$

where I_1 and I_2 are the irradiances of two electric fields respectively. $\gamma_{12}(\tau)$ is interference term, where the τ is the time difference of two optical paths. $\tau = (s_1 - s_2)/c$, where the s_1 and

---

[§§] θ is a half-angle between two wave beams, or $\theta = \theta_1 + \theta_2$

s_2 are the light paths from two points, and c is the velocity of light in vacuum. $\gamma_{12}(\tau)$ is called the degree of partial coherence [1957 Thompson]. The formula (2.1.3) is the general interference law for stationary optical fields [2003 Born, Max]. The significance of $\gamma_{12}(\tau)$ may best be seen by expressing (2.1.3) in a somewhat different form as following [2003 Born, Max].

$$I = I_1 + I_2 + 2\sqrt{I_1 I_2} \cdot |\gamma_{12}(\tau)| \cdot \cos[\alpha_{12}(\tau) - \delta] \tag{2.1.4}$$

where the phase difference δ has the value of $2\pi\nu'\tau = 2\pi(s_2 - s_1)/\lambda'$, where ν' and λ' are the mean frequency and mean wavelength of the quasi-monochromatic light source respectively[***].

The degree of coherence can be measured by the visibility of interference [1974 Fowles].

$$\begin{aligned} |\gamma_{12}| = 1 \quad & : \text{coherent completely} \\ 0 < |\gamma_{12}| < 1 \quad & : \text{coherent partially} \\ 0 = |\gamma_{12}| \quad & : \text{completely incoherent} \end{aligned} \tag{2.1.5}$$

The appearance of fringes is limited by the degree of coherence. It is expressed with the visibility of interference fringes given by:

$$V = \frac{I_{max} - I_{min}}{I_{max} + I_{min}} = \frac{2\sqrt{I_1 I_2}|\gamma_{12}|}{I_1 + I_2} \tag{2.1.6}$$

In interference lithography particularly, visibility of fringes can be obtained from results of response of photoresist. The depth of grooves is dependent on exposure energy (mJ/cm^2). With partially coherent light, the groove is gradually reduced as a function of the first Bessel function given by Van cittert and Zernike theorem [Appendix].

2.1.3 RESOLUTION OF EUV INTERFERENCE LITHOGRAPHY

The minimum pitch achievable within a single exposure is a half of the wavelength. With a 193 nm ArF excimer laser source, the resolution is limited to ~ 96 nm. The use of a suitable fluid, e.g. water, between the imaging object and the wafer allows for an improvement of the optical resolution by a factor of the refractive index of the immersion

---

[***] $\gamma_{12}(\tau) = |\gamma_{12}(\tau)| \cdot e^{i[\alpha_{12}(\tau) - 2\pi\nu'\tau]}$, where $\alpha_{12}(\tau) = 2\pi\nu'\tau + \arg[\gamma_{12}(\tau)]$

fluid. With a 193 nm excimer laser and H_20 immersion (n = 1.44), the limiting dimension is reduced to the pitch of ~64 nm. At shorter wavelengths in UV, e.g. 157 nm (F_2 excimer laser), CaF_2 optics, water immersion technique and atmospheric air environment cannot be used anymore due to the high absorption. Thus, ArF immersion lithography is the latest lithography technology using refractive optics. However, there are alternative techniques to overcome the resolution limit of ArF immersion lithography such as multiple exposures with lateral shift (double patterning). This method requires precise control of an overlay to repeat the following exposures [2005 Brueck].

Resolution limit of EUV Interference Lithography

One way to print out the pattern below pitch = 20 nm is to use radiation in the EUV spectral range. The immersion or multiple exposure techniques are not required to achieve such a high resolution pattern. However, EUV interference lithography is limited by several conditions of system. The efficiency of the EUV beam splitter is very low in comparison to the visible (prism) or UV beam splitters (glass plate and mirror). In the case of UV-IL, there is no significant loss of intensity, so the flexible arrangement of multiple-beams on the target plane is possible. In contrast, EUV-IL operates only in high-vacuum chamber and no such beam-splitter without intensity loss exists. Also achieving high-reflectivity at high angle on the mirror is very limited. Nevertheless, EUV-IL can enable printing with the better resolution than other ILs techniques with the X-ray or the UV radiation due to the short-wavelength nature comparing to UV radiation and low photon blurring effect comparing to X-ray [1995 Okazaki].

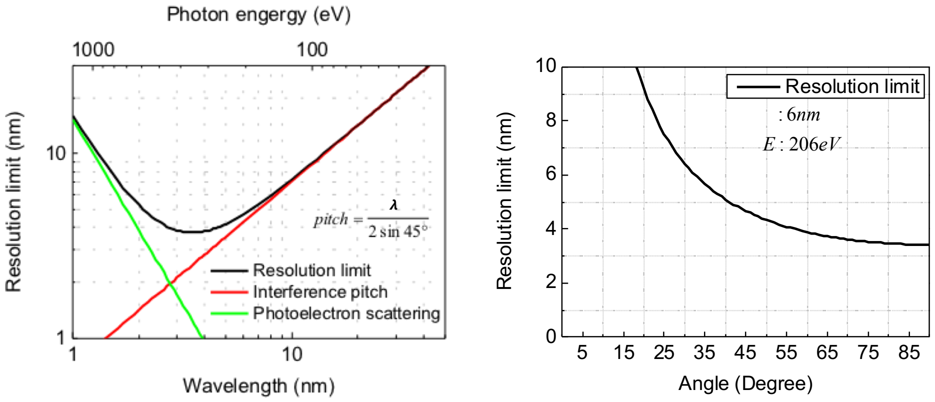

Fig. 2.1.2 The resolution of IL: The resolution curve for the angle of 45° as a function of the wavelength (left) and the resolution curve for the light wavelength of 6 nm as a function of the angle (right). The photoelectron scattering curve is dependent on the type of photoresist.

The resolution limit of EUV-IL at an angle of 45° (as an example) as a function of the wavelength is plotted in Fig 2.1.2 (L). The resolution limit is in the range of the photon energy yielding the photoelectron scattering (resist blur) around 1 nm[†††]. The resolution down to around 3 – 4 nm is seen in the parabolic curve in the figure (Fig. 2.1.2 L). The resolution with the wavelength of 6 nm as a function of the incident angle is plotted in Fig. 2.1.2 (R). The photoelectron scattering is negligible at this photon energy. The resolution limit is at around 4 nm with the angle of around 50°.

[†††] The data of photoelectron scattering blur in X-ray and soft X-ray range in Fig. 2.1.2 is from the data of X-ray scattering blur in [1995 Okazaki]. The secondary electron blur has to be considered in addition to the photoelectron scattering blur in order to obtain more precise resolution result [2009 Lee].

2.2 LLOYD'S MIRROR INTERFERENCE LITHOGRAPHY

Lloyd's mirror interference lithography with the EUV radiation from a high-harmonic source

In this chapter, we demonstrate interference lithography using a high-harmonic source. The benefits of using a high-harmonic source include increased range of extreme ultraviolet (EUV) wavelengths and the use of much shorter pulses and the exploration of the role of peak power as well as illumination energy. EUV radiation is produced by high-harmonic generation with 800 nm light from a femtosecond Ti:Sapphire laser (40 fs pulses, 1 kHz, 2 W average power) in an argon gas-cell. Interference patterns created using a Lloyd's mirror setup and monochromatized radiation at the 27th harmonic (29nm) are recorded using a ZEP-520A photoresist, producing features with pitch of < 200 nm. The effect of the use of femtosecond pulsed EUV radiation on the recorded pattern is investigated. The capability of the high-harmonic source for high-resolution patterning is discussed.

2.2.1 INTRODUCTION

Extreme ultraviolet (EUV) interference lithography (IL) is a powerful method of fabricating a high-resolution pattern over a large area without a complex imaging system. The main requirement for EUV-IL is high intensity coherent plane wave illumination in order to deliver a sufficient exposure dose to the photoresist plane. A particular issue is the availability of appropriate optical components such as beam splitters and reflective or spectrally filtering mirrors for the particular optical wavelength used. Those components can be obtained easily in the case of using radiation in the spectral range over deep ultraviolet, ultraviolet, and IR lasers where refractive optical elements are available. [2005 Brueck, 2013 Wathuthanthri, 2015 Miyazaki]

When using EUV or soft X-ray radiation, different strategies to split and recombine parallel beams have been demonstrated such as those using a reflective beam splitter [1999

Solak, 2007 Ritucci, 2007 Wachulak, 2009 Zuppella] or multiple diffraction gratings [2006 Solak, 2014 Mojarad]. These demonstrations were performed with both a synchrotron radiation source and a plasma based EUV laser. In the demonstration performed using synchrotron radiation, the monochromatized and spatially filtered light at a wavelength of 13.5 nm from an undulator provided the necessary temporal and spatial coherence with sufficient intensity flux [1999 Solak]. The plasma based EUV laser is also a suitable radiation source for IL as it was demonstrated using a compact Ne-like Ar capillary discharge laser at wavelength of 46.9 nm producing an EUV radiation of around 0.2 mJ with a maximum repetition rate of several Hz (< 10) [2007 Wachulak].

Interference lithography has also been performed in the UV and IR spectral ranges with femtosecond pulsed lasers [2015 Miyazaki, 2001 Kondo, 2004 Nakata]. The second harmonic of femtosecond pulses (380 nm, 80 fs, 82 MHz) was split by a diffractive beam splitter and overlapped with two lenses [2001 Kondo]. A femtosecond laser pulse (800 nm, 90 fs) was used for lithographical laser ablation to fabricate a homogeneous metal nanograting [2015 Miyazaki, 2004 Nakata]. The EUV-IL demonstrations using a synchrotron radiation source and a plasma-based EUV laser have used radiation with a pulse duration of around 1-2 ns. The effect of high-density ionization using ultra-short EUV pulses generated by a free electron laser (FEL) on the sensitivity of a non-chemically amplified resist was investigated [2012 Okamoto]. It was shown that multiple reactions with ultrahigh-brightness pulses provided by EUV-FEL radiation changes the sensitivity of the resist.

High-harmonic generation (HHG) provides coherent radiation in a wide EUV spectral range (10-40 nm) with emission peaks at the odd harmonics of the driving laser field ω. The degree of temporal coherence of each individual peak is on the order of $\Delta\lambda/\lambda \sim 10^{-3}$. The spatial coherence length depends on the HHG phase-matching process in the gas-cell-based high-harmonic source. The high spatial coherence and low divergence of the HHG beam were already presented [1996 Zhou, 2002 Bartels].

In this work, we demonstrate Lloyd's mirror IL with EUV radiation generated by a HHG source. The demonstration was performed with a monochromatized radiation centered at a wavelength of around 29 nm, and small angle in the Lloyd's mirror allows us to achieve fringes with sub-200 nm pitches. We analyze the expected optical properties of the interference fringes in the photoresist.

2.2.2 METHODOLOGY

Interference fringe

The interference fringes are formed owing to the constructive and the destructive interferences between the split beams of the reflected wave and the direct wave in the Lloyd's mirror arrangement (Fig 2.2.1.). The period (pitch) of the interference fringes, which is determined by the angle between two beams, is given by:

$$pitch = \lambda / [2\sin(\theta)] \tag{2.2.1}$$

where the θ is the half-angle between two interfering waves. The number of pitches (N) in the interference field in this demonstration is estimated to N = λ/Δλ ≈ 250 approximately. Lloyd's mirror arrangement is a special case of two beams interference set-up with the scheme that the reflected wave is delayed compared to the direct wave.

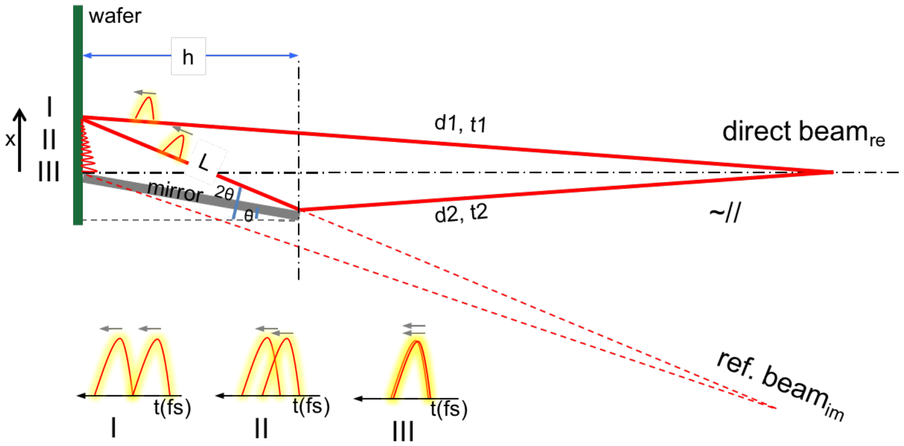

Fig. 2.2.1 Schematic of the Lloyd mirror IL with a focusing beam: reflected and direct beams having different optical paths (d) and arrival times (t) are illustrated. The angle of the mirror is θ from normal. The visibility of fringes decreases away from the edge owing to the optical path difference between two short pulses

Fig. 2.2.1 illustrates the Lloyd's mirror IL set-up of the experiment. The divergence of the EUV beam after the gas cell is around 1-2 mrad, and after the spherical mirror, it is around 5-15 mrad in Fig. 2.2.4. In the analysis, we assume that the incidence angle of the direct beam is approximated to a normal angle, and the angle of the reflected beam is approximated to be twice the mirror's angle (2θ). In the Lloyd's mirror system, a reflective mirror splits part of the incident beam, and redirects the reflected part to generate a second beam. During this separation, an optical path difference (OPD) between two beams occurs. Using fs-pulsed radiation, the OPD has to be controlled in the range of only a few micrometers. The fringe profile visibility[⌗] decreases away from the edge (the line shared by the photoresist and mirror planes) owing to the increase in OPD.

Interference with short-pulsed EUV radiation

The OPD yields time delay for the reflected beam arriving at the target plane. It is approximately L-h, as illustrated in Fig. 2.2.1, and increases with the angle (θ). In the photoresist plane, the delay increases proportionally with the distance (x in Fig. 2.2.1) from the edge. The field length of the fringe along the x-direction is estimated to be $\{OPD\times[\tan(2\theta)-\tan(\theta)]/[1/\cos(2\theta)-1]\}$ from a geometrical approximation. The time difference between two pulses is OPD/c (c: speed of light in vacuum), which must not exceed the pulse duration, $L-h = OPD < \text{pulse duration} \times c$. The temporal overlap of two pulses, which determines the interference term, decreases with the OPD. Also the interference region depends on the angle θ and pulse duration. A rapid reduction in visibility is predicted when $\theta > 15°$.

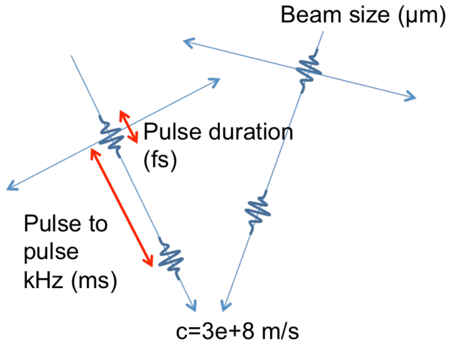

Fig. 2.2.2 The scheme of the interference of two pulsed beams

In Fig. 2.2.2, the situation of interference of two pulsed beams is illustrated. The possibility of interference between two beams depends on the pulse duration and the lateral size of two beams.

[⌗] In the lithographic performance, fringe visibility depends on the response of photoresist to photons. The depth of radiation-induced grooves depends on the fluence (mJ/cm^2).

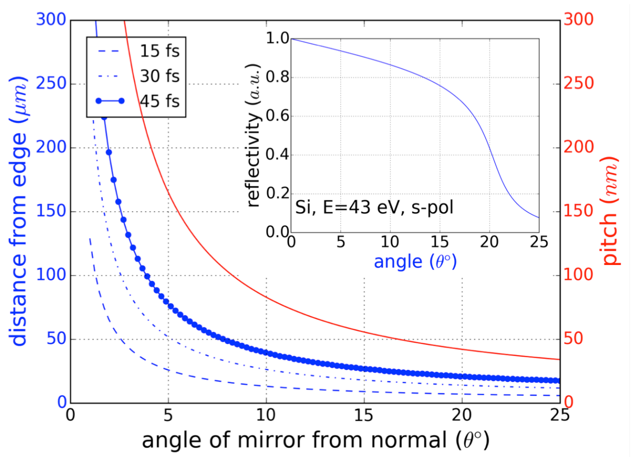

Fig. 2.2.3 Angle dependency of interference region (left axis) for certain pulse durations (15-45 fs) and period of pattern (right axis, red solid line): The inset image is the reflectivity of Silicon mirror as function of the angle with photon energy of 43 eV.

With EUV radiation, the interference region (x) is also affected by the mirror's reflectivity. The maximum angle is limited to around 20° with a thick Si mirror for radiation with a wavelength of 29 nm. Fig. 2.2.3 plots the interference area (distance from edge) depending on the pulse duration as a function of the angle of the mirror in the Lloyd's mirror interference scheme. We use a Si mirror at $\theta \approx$ 3-4°, providing reflectivity of ~95 % for the EUV wavelengths used in this demonstration as shown in inset image in Fig. 2.2.3.

2.2.3 EXPERIMENTAL DEMONSTRATION

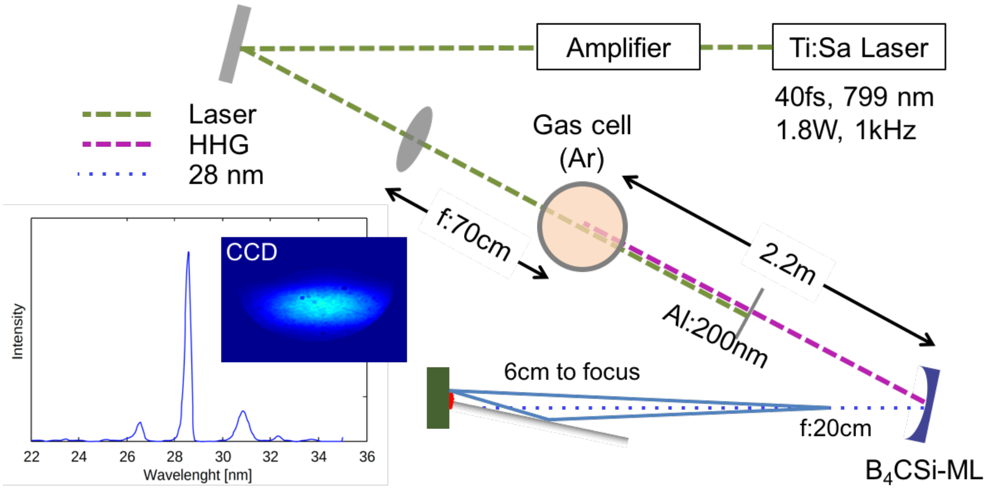

Fig. 2.2.4 HHG and Lloyd mirror interference lithography setup: the laser is s-polarized: the inset image plots the spectrum after the ML with the CCD image of the beam spot. The monochromatic

EUV wave after the ML filter illuminates the Lloyd mirror scheme and photoresist at 6 cm away from the focus of ML.

Our experimental setup is illustrated in Fig. 2.2.4. We use HHG system based on Ti:Sapphire laser (800 nm, 40 fs) amplified by a regenerative chirped pulsed amplifier (CPA). The laser beam (10^{14} W/cm^2 at the gas cell position, 1.8 mJ/pulse, 1 kHz repetition rate) is focused into a 3-mm-long gas cell filled with argon gas at 60 mbar. The strong E-field has a pulse duration of around 40 fs. A single Al foil (200 nm thickness) is used to block the fundamental laser and transmit the EUV radiation about 30 %. Then, in order to suppress the unwanted EUV spectral range, the beam is spectrally filtered by a curved B_4C/Si multilayer (ML) mirror, which reflects and focuses the main wavelength at ~ 29 nm (27th harmonic, $\Delta\lambda/\lambda \sim 4\times10^{-3}$) and ±1 harmonics from the main wavelength with very low intensity. The spectrum after the ML mirror is shown in the inset image in Fig. 2.2.4. The Gaussian-shaped illumination profile measured using an EUV-sensitive CCD camera (Andor DX-434, 1024×1024 pixels) is shown in the inset CCD image in Fig. 2.2.4. The estimated photon flux is ~1.86×10^9 photons/s in the whole area of the spot. [§§§]

Exposure test

Before performing the IL, we conducted exposure tests for a photoresist sample. We used a positive-tone photoresist (dilution ratio: ZEP-520A:Anisole=1:3). The photoresist (resist) was spin coated (5000 rpm, 1 min.) on a silicon wafer for the target thickness of ~ 40-60 nm and baked for 2 min at 180 °C on a hotplate. In the setup (vacuum chamber), the photoresist-coated wafer was mounted perpendicularly to the beam. The exposure time was varied from 0.5 to 15 s at several positions between ±5 mm from the EUV focus in order to record the cross-sectional profile of the beam. After the exposure, the wafer was developed with ZED N50 for 90 s and rinsed with 2-propanol for 30 s. The obtained result was investigated with an optical microscope (Nikon-Eclipse-L200) to measure the

---

[§§§] The number of photons per second is determined by: $N_{ph/s} = \frac{S_{CCD}\cdot\sigma}{\eta_{QE}\cdot(E_{ph}/3.65\ eV)\cdot t_{exp}}$, where S_{CCD}: counted signal on the CCD, σ: CCD sensitivity in electrons per count, η_{QE}: quantum efficiency of the CCD, E_{ph}: photon energy, and t_{exp}: exposure time, (σ: 2, η_{QE}: 0.3, E_{ph}: 43 eV, t_{exp}: 0.05 s, $S_{CCD} = 1.6*10^8$).

intensity profile of the beam (Fig. 2.2.5). It was analyzed in terms of the dependence of the removed resist thickness on the radiant fluence (exposure dose), which is related to the lithographic sensitivity of the photoresist with the EUV radiation. The thickness dependence of the removed photoresist (depth from the surface) on fluence is plotted in Fig. 2.2.6.

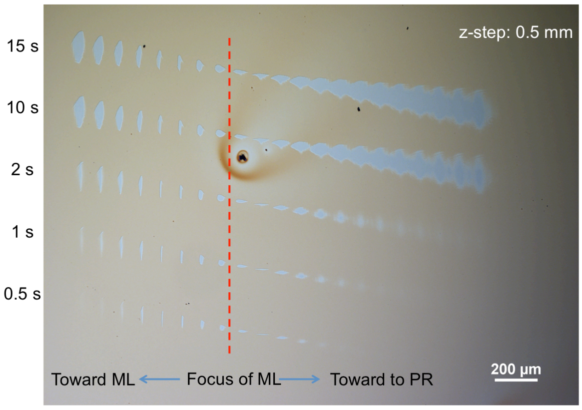

Fig. 2.2.5 Optical microscopy image of the ZEP photoresist exposed by the monochromatic EUV radiation

ZEP-520A is a positive-tone photoresist, which is a modern alternative to PMMA, based on the co-polymer compound (Zeon Corp.). The molecular mechanisms of ZEP-520A are not entirely understood yet [2011 Koshelev].

The photoresist processing is separated into exposure and development. Typical positive photoresists are composed of a photoactive compound, a base resin, and a suitable organic solvent system. The base resin, which is soluble with developers, is protected by the photoactive compound (inhibitor). The radiant energy delinks the inhibitor from the resin and results in an increased photoresist dissolution rate. Thus, exposure wavelength (photon energy) is an important parameter of resist sensitivity [1975 Dill].

There are two issues with the use of short-pulse radiation in Lloyd's mirror IL. The first one is the arrangement for interference, as discussed. The other issue is the interaction between the resist and the short-pulse radiation. The EUV pulse length from HHG sources is on the order of femtosecond duration. This is very different from the plasma-based EUV radiation, which typically yields nanosecond pulses, and is a quasi-CW (continuum wave) on the timescale of the exposure process.

The probability of delink decreases with increasing flux density at an identical exposure dose. The single photon breaks the cross-link within a particular radical distance, which is the effective range of the reaction between a photon and the photoresist [2012 Okamoto].

The spatiotemporal overlap of photons reduces the effectiveness, while the high radical concentration enhances local delinks. The use of short-pulse (high-density flux) enhances competing effects resulting in different exposure sensitivities. It might be interesting to compare our result with that from the plasma-based sources or synchrotron radiation in the future. The dependence of exposure results on pulse duration should be explored more.

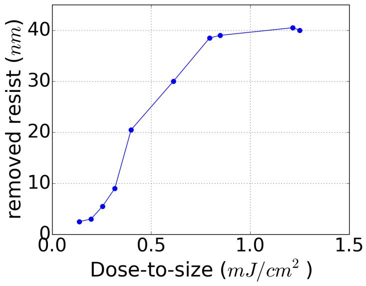

Fig. 2.2.6 Depth of removed photoresist depending on the exposure dose

2.2.4 Result and discussion

The Lloyd's mirror IL was performed with the photoresist prepared as described previously. The ZEP-520A coated wafer was mounted on a nano-precision piezo stage (SmarAct - SLC-1730) at the normal angle to the beam path. The photoresist plane was located at the z-position around z = +6 mm (toward photoresist) from the focal plane of the ML, which is an optimized location for sufficient exposure conditions of the field size of the beam (~200×50 μm) and the exposure time. The exposure time was ~9 s. After the exposure, the photoresist was developed with ZED N50 for 90 s and rinsed with 2-Propanol for 30 s. The resulting patterns were analyzed by atomic force microscope (AFM, Brucker).

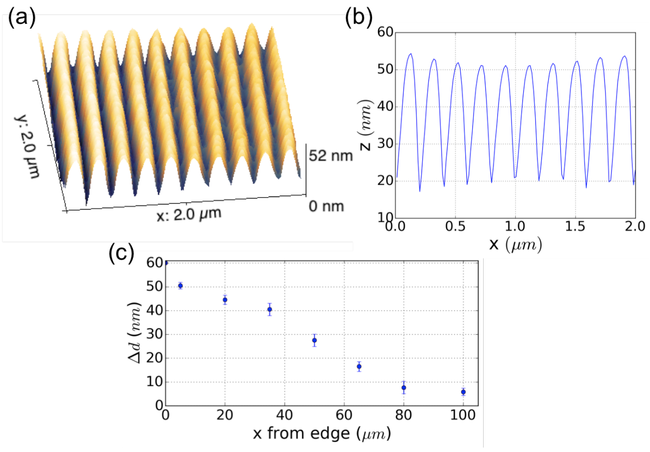

Fig. 2.2.7 (a) AFM image of the patterned photoresist, (b) thickness profile showing a half-period of 99 nm, and (c) groove depth along x-axis.

The resulting AFM image in Fig. 2.2.7 (a) shows a pattern with period of 198 nm with corresponding mirror's angle of 4.2°. Fig. 2.2.7 (b) is the cross-section of the (a). The groove depth (Δd) along the x-axis is measured and plotted in Fig. 2.2.7 (c), and clearly drops as a function of distance from the mirror edge. There are several reasons for the drop. Firstly, the transverse intensity profile of the Gaussian beam drops away from the edge, where the right half is flipped over the mirror with a reflection of ~95 % in Lloyd's mirror scheme. Secondly, the time delay between the reflected and direct beams increases away from the edge. As the interfering time decreases, the degree of mutual coherence decreases resulting in the drop of fringe visibility. The Fig. 2.2.8 shows the interference fringes with shifted positions of the beam against the Lloyd's mirror. The pitch is slightly changing with the shifted positions owing to the slightly different angle between the direct and reflected beams from both the different positions of the beam against the mirror and the divergence of the beam.

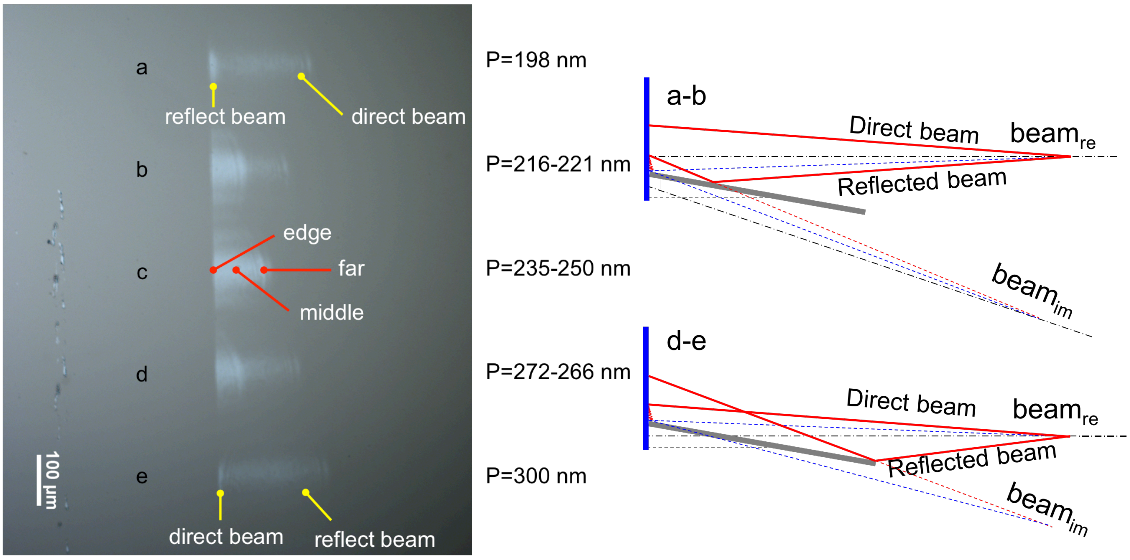

Fig. 2.2.8 Optical microscope image of the photoresist after development: The two beams (direct and reflected beams) are seen at each exposure. The areas of two beams are changing because the wafer stage was moving horizontally for individual exposures, a-e. Geometry of beam paths is illustrated in case of both (a-b) and (d-e).

In the photoresist, the depth (d) after the lithographic process can be derived as d=[1–exp(-αIt)]D, where α is the lithographic factor related to resist sensitivity, t is the exposure time, and D is the initial thickness of the photoresist. Then, the groove depth can be given by:

$$\Delta d = \{1\text{-}exp[-\alpha(I_{max} - I_{min})t]\}D, \tag{2.2.2}$$

Applying $(I_{max} - I_{min}) = 2(I_1 + I_2)V$ to Eq. (2.2.2), we obtain the following relationship between Δd and V:

$$\Delta d/D = 1\text{-}exp[-2\alpha(I_1 + I_2)Vt], \tag{2.2.3}$$

Thus, the fringe visibility V can be written as:

$$V = -\ ln(1 - \Delta d/D)/[2\alpha(I_1 + I_2)t]. \tag{2.2.4}$$

In principle, the intensity distribution of interference fringes is time averaged sum of two electric fields. We now have to consider the time integral over the pulse duration. For nano- or pico-second pulses, the change in time integral is negligible along the x-axis owing to the long pulse duration. However, for the pulses below 100 fs, the time integration term drops quickly away from the edge. In the interference term of the fringe in equation (2.1.3), the I_2 is delayed. It implies that the time integration over the overlap of two pulses can be assumed to be I_2, which interferes with the I_1. Thus, I_2 can be rewritten as: $\{I_2' = I_2 \times O_{(x)}\}$, where $O_{(x)}$ is an overlap factor with a normalized value, shown in Fig. 2.2.9 (b), which depends on the pulse duration.

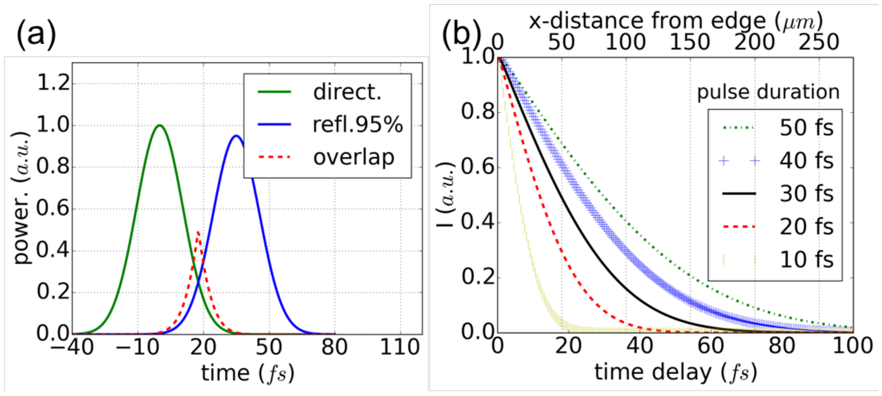

Fig. 2.2.9 (a) Pulses of the direct and reflected beams with the time delay. The pulses partially overlap depending on both the OPD and the pulse duration. (b) Integration of the overlap as a function of the time delay for several pulse durations.

A typical Gaussian shape pulse is plotted in Fig. 2.2.9 (a), where the pulse length is assumed to be the full-width at half maximum (FWHM) of the pulse. Fig. 2.2.9 (a) shows the direct and reflected pulses with some time delay. The partial overlap of the pulses in time depends on both the OPD and the pulse duration. The overlap decreases as the OPD increases or as the pulse duration decreases, as plotted in Fig. 2.2.9 (b). Pulse durations from 10 fs to 50 fs are investigated. The overlapping area drops more quickly as the pulse duration decreases.

The visibility for short-pulse radiation can be written as $V(I_1, I_2')$. In order to eliminate an unknown factor α, we plot the visibility as:

$$V_{(x)}/V_0 = -\ln(1-\Delta d_{(x)}/D) \times I_0/I_{(x)}, \qquad (2.2.5)$$

where $V_0 = V_{(x=0)}$, $I_0 = I_{1,(x=0)}+I'_{2,(x=0)}$, and $I_{(x)} = I_{1,(x)}+I'_{2,(x)}$. The Fig. 2.2.10 shows the results obtained using equation (2.2.5) with different distances from the edge. The visibility is > 0.55 over the investigated area. The visibility is not significantly reduced in the investigated x-range [2009 Zuppella, 2011 Wathuthanthri].

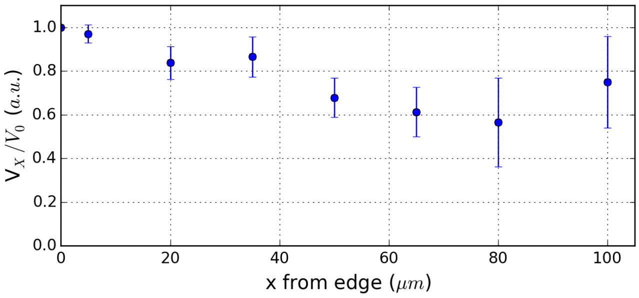

Fig. 2.2.10 Visibility over the edge region with the assumption that the pulse duration of the EUV light is 30 fs.

2.2.5 Conclusion

In conclusion, we have demonstrated a Lloyd's mirror IL in HHG system. Monochromatized EUV radiation generated by a HHG source enables us to perform laboratory lithographic fabrication for high-density periodic structures. The exposure of the ZEP-520A photoresist is obtained for the radiation used. The fringe visibility over the field is measured and corresponds well to a model that includes the effects of the Gaussian beam profile, the optical path difference and the pulse duration. The reflectivity of the mirror, the degree of mutual coherence, and the overlap of two pulses affect the visibility. In the future, the pattern of sub-60 nm pitch (30 nm half-pitch) is expected to be possible, using Lloyd's mirror angles up to 15° with the utilized radiation in this experimental setup.

Chapter 3

Fresnel Diffraction Image in EUV

3.1 SCALAR DIFFRACTION

3.1.1 REVIEW OF CLASSICAL DIFFRACTION THEORY

Scalar diffraction

In classical optics, diffraction of a light wave is a simple case of interference. The diffraction is determined by the behavior of propagating waves. The Huygens-Fresnel principle explains the essential features of classical diffraction. Every point of the wave-front acts as a secondary source emitting a monochromatic spherical wave radiation. The sum of these secondary waves determines the form of the propagating wave at any subsequent time. A secondary source is a disturbance described by a spherical wave:

$$U(r,t) = U_0 \frac{e^{i(kr-\omega t)}}{r} \tag{3.1.1}$$

The complex amplitude U is a scalar wave function of the electric-field amplitude that is adequate when polarization is not important, and only a small angle of diffraction is considered [1974 Hecht, 1975 Fowles].

From the idea of Green function integrating for the surface of a radial source, the Fresnel-Kirchhoff applies to integration including the diffractive aperture, which makes the basis of the scalar diffraction formulae. The formations take the aperture either to be opaque or to be fully transparent.

Fresnel-Kirchhoff diffraction

Fresnel-Kirchhoff diffraction theorem solves a general problem of diffraction in the paraxial regime. It can be used to model the propagation of light in either numerical or analytical modelling. It describes the wave disturbance when a monochromatic spherical wave passes through an opening in an opaque screen. The approximation is obtained with boundary conditions including the optical field U_0 in the aperture area A_1, and the optical field U=0 at all points on the screen A_2 and at large distances in image space A_3.

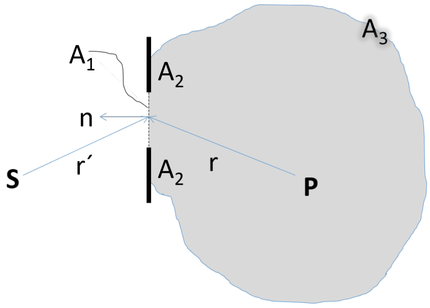

Fig. 3.1.1 The geometry for the Fresnel-Kirchhoff formula with boundary conditions A: A_1 is the opening, A_2 is closed with the edge of opaque screen, and A_3 is the boundary at large distance.

The Fresnel-Kirchhoff integral formula is given by following:

$$U_{FK} \approx -\frac{iU_o}{2\lambda}\iint \frac{e^{ik(r+r')}}{rr'}[cos(n,r) - cos(n,r')]\,dA \tag{3.1.2}$$

where the U_0 is the amplitude of the incident radiation field, k is the wavenumber, r is the distance of the element of aperture from the observation point, r' is the distance of the element of aperture from the primary source, cos(n,r) is a diffraction angle, and A is the area of the aperture. This scalar approach assumes the paraxial approximation, which is valid when $d^2/z > \lambda$.

The Rayleigh-Sommerfeld approximation is an attempt to solve the problem of boundary condition near the edge of the aperture that Fresnel-Kirchhoff's assumptions have in regard to a discontinuity around edge [2003 Born]. There are two formulae depending on the approach to solving the boundary conditions given by:

$$\begin{aligned} U_{RSI} &\approx \frac{iU_o}{\lambda}\iint_A \frac{e^{ikr'}}{rr'}[cos(n,r)]dA \\ U_{RSII} &\approx -\frac{iU_o}{\lambda}\iint_A \frac{e^{ikr'}}{rr'}[cos(\mathrm{n},r')]dA \end{aligned} \tag{3.1.3}$$

The three approximations above are done under following conditions:

$$\begin{gathered} r, r' \gg \lambda \\ Aperture \gg \lambda \end{gathered} \tag{3.1.4}$$

The first condition is yielded in order to make the equation simpler. The condition r' $\gg \lambda$ is satisfied when the illumination is plane wave. The second condition is associated with the boundary condition of aperture.

The Fresnel-Kirchhoff formula is the mean value of two Rayleigh-Sommerfeld formulae: $U_{FK} = ½(U_{RSI} + U_{RSII})$. For small incidence and diffraction angles, cos(n,r) ~ 1, cos(n,r') ~ -1, the three formulae yield very similar result $U_{FK} \sim U_{RSI} \sim U_{RSII}$, unless the image plane is not in the extremely near region [2003 Born].

Fresnel diffraction is the analytical form of the F-K formula for near-field images, while the Fraunhofer diffraction is also the analytical form of the F-K formula for far-field images. A single personal computer nowadays is powerful enough to calculate a near-, and far- field image of masks consisting of micron to sub-micron features with the EUV wavelength only within a few seconds, or a few minutes in case of incoherent sum of diffraction images [2003 Brooker, 2010 Schmidt, 2011 Voelz].

Diffraction field regime and Fresnel number

When light propagates very far from the source aperture, the optical field in the observation plane is approximated by the Fraunhofer diffraction integral. The "very far" is defined by $z > a^2/\lambda$ [1996 Goodman].

$$N_F = \frac{a^2}{z \cdot \lambda} \tag{3.1.5}$$

is called Fresnel number, where a is the characteristic size of an aperture, and z is the location of the detector from mask. The diffraction field regime can be separated as following:

$$\begin{aligned} &N_F \ggg 1\text{: Geometrical optics regime} \\ &N_F \gg 1\text{: angular spectrum method regime [2010 Schmidt]} \\ &N_F \sim 1\text{: Fresnel diffraction regime} \\ &N_F \ll 1\text{: Fraunhofer diffraction regime} \end{aligned} \tag{3.1.6}$$

These particular methods can enable approximate calculation of diffraction images with more accuracy and more efficiency.

The approximation methods are based on scalar diffraction theory. The analytical solutions for diffraction only exist for a limited number of aperture shapes or periodic patterns. In the extremely near-field, calculating diffraction images requires rigorous methods. In this regime, even the plane of z=0 is not defined due to the thickness of the aperture. The discussions on this issue will be taken account in Chapter 3.3 with more detail. The near-field diffraction image of F-K, or RS -I, and –II can be computed with either numerical integration or the Fourier transformation in the frequency domain where the fast Fourier transform (FFT) has a great advantage regarding computation time. Fig.

3.1.2 summaries the diffraction field in terms of distance z. Table 3.1.1 summarizes the conditions of particular scalar approximations.

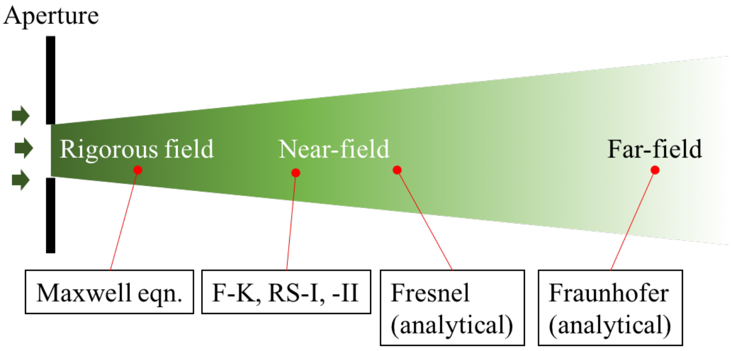

Fig. 3.1.2 The fields approximated by diffraction region [2007 Mack]

Parameter	F-K, RSI, II (Numerical)	Fresnel (Ana)	Fraunhofer (Ana)
Condition	$z \gg \lambda$, $a \gg \lambda$	$z \gg a$, $a \gg \lambda$	$z \gg a^2/\lambda$

Table. 3.1.1 The field regime according to the conditions of approximations [2003 Born]

3.1.2 RESOLUTION OF PROXIMITY LITHOGRAPHY

The resolution of proximity printing is given by:

$$Resolution \approx \alpha\sqrt{D \cdot \lambda} \tag{3.1.7}$$

The expression shows that the minimum printable size is increased with the proximity gap between the mask and the wafer D and wavelength of illumination λ. The α is the parameter dependent on particular process. In X-ray lithography, the resolution capability is a critical issue due to the image blur. With X-ray wavelength shorter than 0.5 nm, the number of photo-electrons and Auger electrons rapidly increases. The practical resolution limit of X-ray proximity lithography is around 100 nm. In proximity printing with EUV radiation, the resolution is enhanced owing to short wavelength, and the size of region blurred by photo-electrons is smaller than 1 nm [1995 Okazaki].

The resolution of EUV proximity lithography is plotted in Fig 3.1.3. This shows that, in the range of EUV, the photo-electron blur is almost negligible and achievable resolution is below 100 nm with proximity gap around 2 μm. The best wavelength in this estimation is around 3.5 nm resulting in resolution below 50 nm.

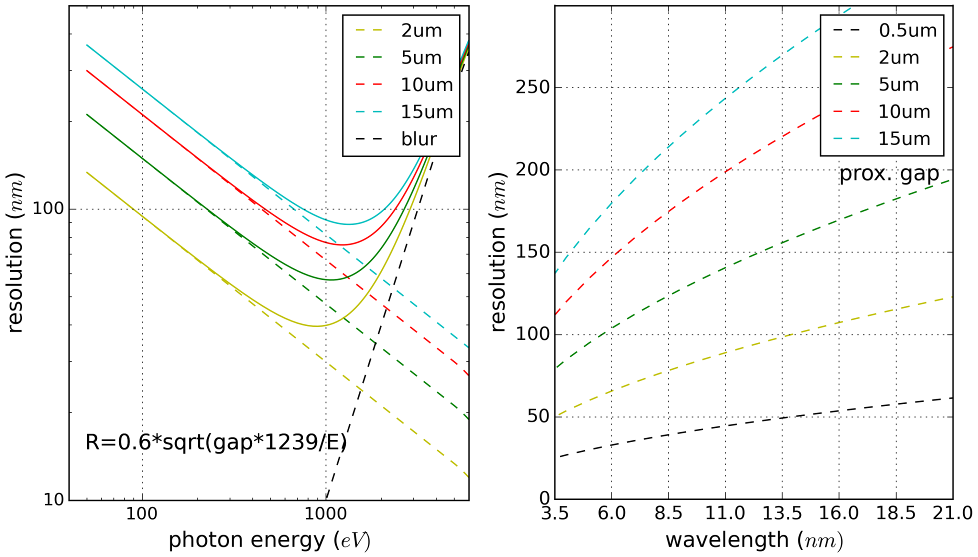

Fig. 3.1.3 Resolution of proximity lithography in EUV spectral range: The blur occurs by photo-electron scattering at high photon energies in X-ray. On the other hand, the blur by EUV photo-electron scattering is negligible.

3.1.3 FRESNEL DIFFRACTION IMAGES IN EUV

In EUV spectral range, Fresnel diffraction is useful to approximate the near-field (~10–500 μm) diffraction image for micro-scale objects of around 1–100 μm. Fig. 3.1.4 shows a propagation image of EUV light through a circular aperture in near-field. The aperture is micro scale of 1.6 μm diameter, the wavelength of illumination is around 11 nm. The diffraction patterns consist of the nanoscale features with high edge resolution owing to the interference of short-wavelength illumination.

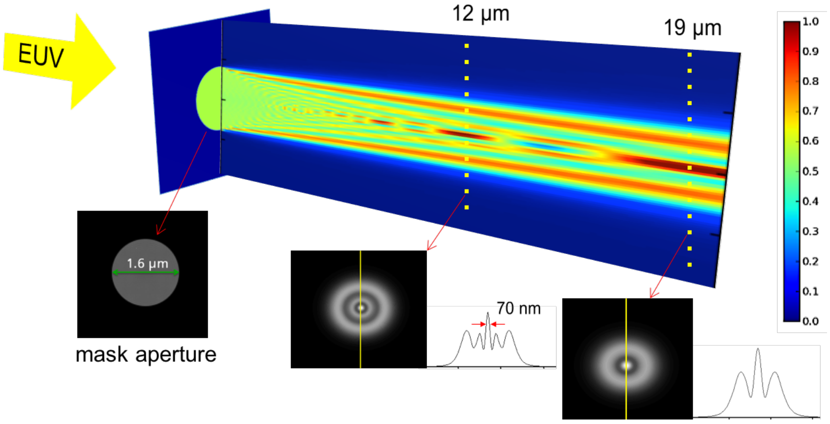

Fig. 3.1.4. The EUV light wave propagation along the z-axis for a circular aperture: The aerial images of intensity at 12 μm and 19 μm proximity gaps from the aperture.

In Fig. 3.1.5, diffraction images of square apertures of different widths are demonstrated. Fig. 3.1.5, (a) shows the square apertures with three different widths of 800 nm, 400 nm, and 200 nm. The (b) are the diffraction images formed at 3 μm away from the aperture. The cross-sectional profiles and the corresponding N_F are plotted at the right side of the figure. In three cases, the Fresnel number is changed from N_F=1, N_F=5, and to N_F=20 as a function of width. The precise control of optical system including sub-micron apertures and the distance between the mask and imaging plane is required with light illumination in EUV spectral range.

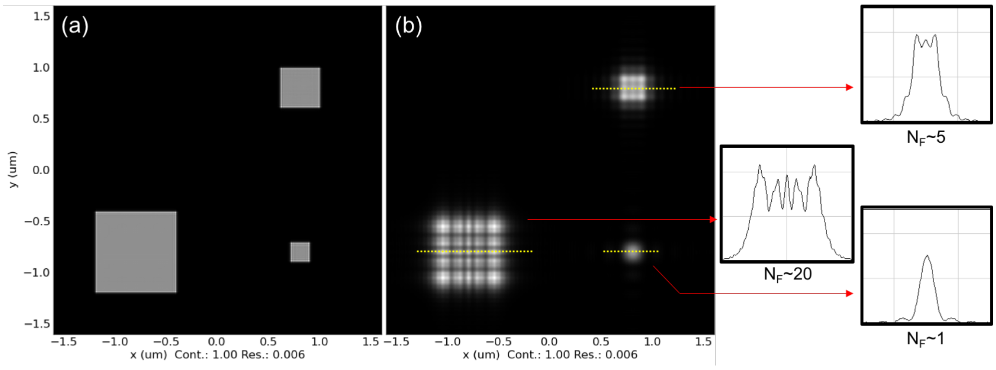

Fig. 3.1.5 (a) Square apertures with three different width of 800 nm, 400 nm, and 200 nm (b) The diffraction images formed at 3 μm away from the aperture: The cross-sectional profiles are plotted for the corresponding N_F.

In this section, Fresnel diffraction is reviewed and discussed for EUV radiation in paraxial regime. Scalar diffraction is useful to predict the diffraction image of sub-micron apertures with EUV radiation. The resolution of proximity lithography is discussed. EUV proximity lithography is more promising to obtain high-resolution print in comparison to the X-ray lithography due to the low blurring effect and sharp near-field interference image. Optical propagation simulation is performed, and the sub-100 nm edge resolution is obtained using micron-scale apertures with EUV radiation. Further details and demonstrations will be shown in the next section.

3.2 PROXIMITY LITHOGRAPHY WITH DPP EUV SOURCE

Diffraction-assisted extreme ultraviolet proximity lithography for fabrication of nanophotonic arrays

The possibilities and limitations of proximity lithography with extreme ultraviolet (EUV) radiation are explored theoretically and experimentally. Utilizing partially coherent EUV radiation with the wavelength of 10.88 nm from Xenon/Argon discharge plasma EUV source the proximity patterning of various nanoantenna arrays has been performed. The experimental results are compared with results of numerical scalar diffraction simulations. It is shown that proximity printing in the Fresnel diffraction mode can enable production of high resolution features even with lower resolution masks. Sub-30 nm edge resolution in resist is demonstrated. The potential of the method is explored by simulation of the patterning through circular and triangular apertures as well as through bowtie antenna patterns. The results suggest that precise control of the proximity gap and the exposure dose together with simulation-supported mask design optimizations may allow for wide variety of high-resolution structures to be printed through relatively simple transmission masks. The method is especially suited for high-performance manufacturing of sub-μm sized nanophotonic arrays.

3.2.1 INTRODUCTION

In this section we investigate the potential of the Fresnel diffraction-assisted proximity printing with EUV radiation of 10.9 nm wavelength emitted from a laboratory EUV radiation source. In traditional X-ray proximity lithography, the achievable resolution is limited by the photon-electron blur occurring owing to the reaction between photons of high energy and molecules of photoresists. However, an advantage using EUV radiation rather than using hard X-ray is that EUV photon energy has secondary electron blur of less than 1 nm. Therefore, the achievable minimum feature size depends only on the wavelength and the proximity gap. With around 11 nm EUV wavelength, the achievable line width with classical proximity lithography is limited to ~100 nm at 1 µm proximity gap ($Res \sim \sqrt{1 \times 0.011}$). However, this limitation describes a blur caused by a classical long-range Fraunhofer diffraction from the mask which is not necessarily a suitable approach when considering results of interaction of EUV radiation with sub-µm sized mask features. For a fixed mask to wafer gap g there is a set of structure sizes a, for which the Fresnel number will be equal or larger than unity, enabling Fresnel diffraction mode. This may allow for production of higher resolution features by the proximity printing at a suitable proximity gap. For EUV proximity printing a suitable set of test structures for this method are optical nano-antennas [2003 Crozier, 2005 Muehlschlegel, 2011 Novotny]. Such nano-antennas can locally enhance the incident electromagnetic fields and thus are of great interest for a variety of applications such as Surface-Enhanced Raman Spectroscopy (SERS) [2008 Stiles] or Surface Enhanced Infrared Spectroscopy (SEIRS) [2000 Jensen, 2008 Neubrech], biosensors [2009 Adato], optical storage [2006 Cubukcu], nanolithography [2006 Sundaramurthy, 2006 Wang] and high-harmonic generation [2008 Kim]. Since we are primarily interested in antennas for SEIRS, the single antenna size is between 250 nm and several micrometers. Nevertheless, the resolution requirements are in the nanometer range, due to critical importance of the edge quality and a requirement to create nanoscale distances between the antenna electrodes to achieve even higher field enhancement [2005 Schuck]. Currently, such antenna arrays are mostly made by state-of-the-art EBL, which limits their industrial exploitation. A relatively simple setup for EUV proximity lithography with a small scale laboratory source can enable a high volume manufacturing of high quality nano-photonic structures.

3.2.2 EXPERIMENTAL SETUP

In this study, EUV proximity lithography utilizes a high power gas discharge produced plasma (DPP) source developed at the Fraunhofer Institute for Laser Technology in Aachen [2005 Pankert, 2000 Bergmann] (Fig. 3.2.1(a)). Such sources normally have a broadband emission spectrum in the EUV range, since radiation is produced by the transitions between the excited states of highly ionized heavy atoms, such as xenon or tin. However, by optimizing the gas composition of the plasma and using suitable band-pass filters it is possible to obtain a radiation spectrum with a dominating maximum at 10.88 nm wavelength with bandwidth of around 3.2% [2009 Bergmann]. The diameter of the pinch varies from 150 μm to 350 μm depending on the gas mixture and discharge parameters.

The laboratory setup for EUV proximity lithography used for this study can illuminate 2" wafers with single exposure field size up to 4 mm^2 (Fig. 3.2.1 (a-b)) [2012 Brose]. The system utilizes high precision linear positioners and a set of three capacitive sensors to control and determine the distance and tilt between the mask and the photoresist-coated silicon wafer down to tens of nanometers. Depending on the mask design and the required structure type, different photoresists[****] were used as a photoactive medium.

The radiation from a partially coherent source passes through a pinhole aperture and irradiates a transmission mask with a divergence angle of 0.0012 radian. The divergence of the beam produces the pattern-shift as an error at the edge of field in the observation plane. With the mask to wafer gap around 10 μm the pattern-shift error of the system is around 18 nm in our setup, providing the practical resolution limit in the experimental demonstration. Reduction of the maximal divergence angle by spatial filtering or bringing the mask closer to the wafer will decrease the pattern shift error further, enabling structuring with sub 20 nm pitches.

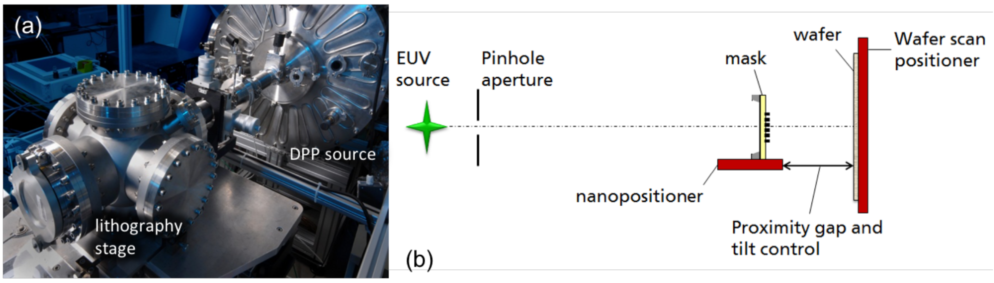

Fig. 3.2.1 (a) Photo and (b) scheme of the experimental setup for EUV proximity lithography used in this study

To support the investigation at this wavelength a novel type of transmission masks has been developed based on free-standing niobium membranes instead of conventional Si_3N_4 supported masks. Niobium is known for its mechanical stability [2006 Danylyuk] and has a high transparency (~65% at 100 nm thickness) at the used wavelength, in contrast to highly absorbing Si_3N_4 [1993 Henke]. The cross section of the transmission mask can be seen in

---

[****] Negative-tone photoresist: XR1541 (Hydrogen silsesquioxane) [Web Dowcorning]).

Positive-tone photoresist: PMMA [Poly(methyl methacrylate)], and ZEP520A-7 [Web Zeon].

Fig. 3.2.2. The layer system consists of the thin Niobium (Nb) support membrane and the structured Ni absorber layer. Niobium is also simultaneously used as a build-in filter for unwanted radiation above 16 nm. The technology can be used to produce not only masks for proximity printing but also for ultra-high resolution interference lithography. Further details on the mask technology can be found elsewhere [2012 Brose].

For this work a transmission mask with various popular nano-photonic antenna designs was produced. The nickel thickness of around 80 nm absorbs 98% of incoming radiation at this wavelength, allowing excellent contrast and large process windows for the processing.

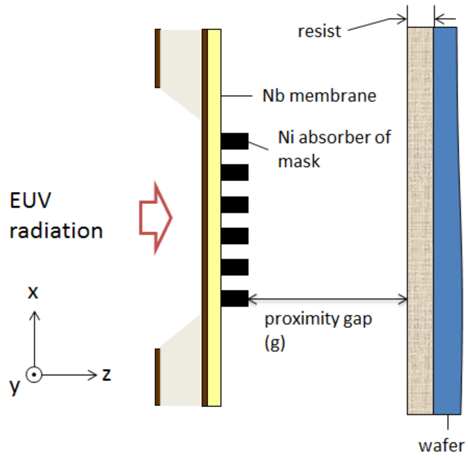

Fig. 3.2.2 Scheme of the lithography front-end, including a transmission mask and a resist coated wafer: The coordinate system and the relevant values are defined.

3.2.3 MODELING

Accurate simulation of the near-field diffraction is extremely important for understanding limitations of EUV proximity lithography. The scalar simulation can be performed with the help of Fresnel-Kirchhoff (FK) diffraction or Rayleigh-Sommerfeld (RS) diffraction integrals. In our setup, where the angles of incidence and diffraction are small, those diffraction formulae give essentially the same results [2003 Born]. For the simulation, we employed lithography simulation software developed by the Fraunhofer IISB [2007 Meliorisz]. Here, we have used the RS integral of the first kind (RS I) since it was shown to produce a little more stable results [2007 Meliorisz]. The EUV wavelength is short enough for this approximation to work with nano-antenna structures with sizes above several hundreds of nanometers and a proximity gap of several micrometers.

The broadband spectrum of the radiation and its angular divergence are implemented in the simulation. The broadband illumination is taken into account by selecting a set of wavelengths around the main peak of the spectrum and summing the different intensities generated by each wavelength. Since the radiation bandwidth of the Xe/Ar plasma source is only 3.2% [2009 Bergmann], the results are qualitatively very similar to the simulation performed with the single 10.88 nm wave, with only minor intensity changes visible. The seven wavelengths around 10.88 nm chosen for the simulation are shown in the Fig. 3.2.3.

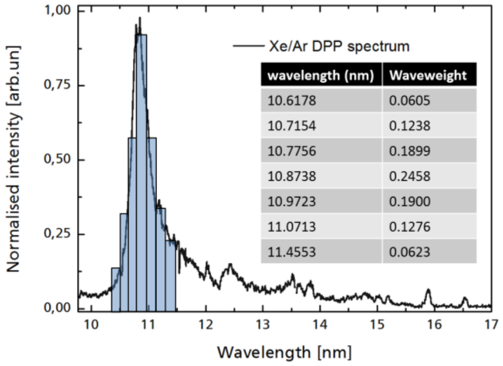

wavelength (nm)	Waveweight
10.6178	0.0605
10.7154	0.1238
10.7756	0.1899
10.8738	0.2458
10.9723	0.1900
11.0713	0.1276
11.4553	0.0623

Fig. 3.2.3 Measured emission spectrum of the DPP source with Xe/Ar gas mixture. The set of wavelengths chosen for the simulation is shown with bars. The wavelength and relative intensity of each wavelength (wave-weights) are shown in the inset table.

It is known that Fresnel diffraction patterns produced by simple round and triangular apertures can become rather complex. For example, in the well-studied Fresnel diffraction on a round aperture a set of concentric rings can be observed with number of rings depending on an observation position. In the Fig. 3.2.4 the results of numerical simulation of such diffraction are presented. Here the intensity profiles produced by the round aperture with the diameter of 1.6 µm (Fig. 3.2.4 (a)) are studied in dependence of the proximity gap. As expected from analytical modeling of the diffraction the change in the Fresnel number manifests itself in the number of visible rings (zones).

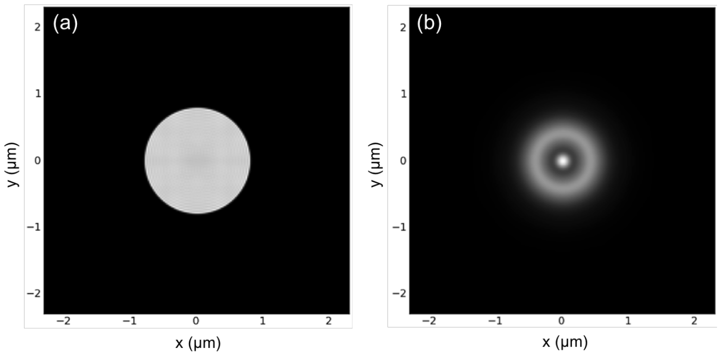

Fig. 3.2.4 The circular aperture (a) and corresponding diffraction image at 19 µm proximity gap

The diffraction on the triangular aperture is more complex. At 20 µm distance the aperture of the length of 1.56 µm (Fig. 3.2.5 (a)) is transformed into a set of three small stabs pointing to the middle of the triangle with sub-100 nm distance between them (Fig. 3.2.5 (b)).

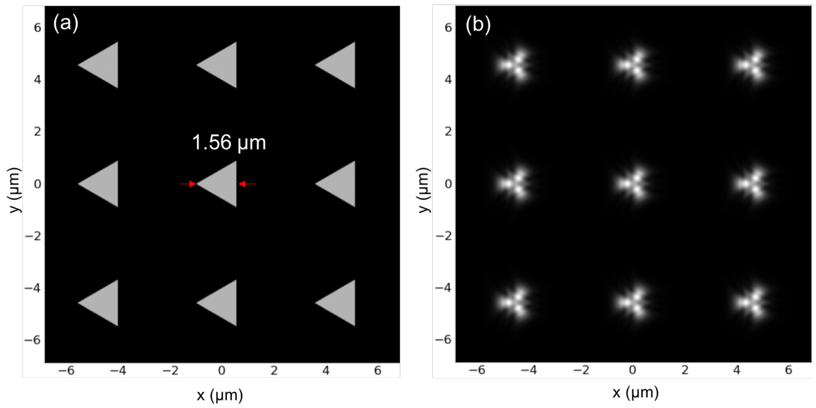

Fig. 3.2.5 (a) The triangular aperture array and (b) the related intensity distribution behind the aperture at 20 µm proximity gap.

The simulations clearly demonstrate the potential of the method for creation of complex nano-photonic structures of novel designs. By tuning the exposure time and modifying the proximity gap the structures of different shapes with down to sub-100 nm resolution can be produced.

3.2.4 RESULTS AND DISCUSSION

Exposure results

The experimental results of the EUV exposures through the circle and triangle apertures are shown in Fig. 3.2.6 in form of atomic force microscope (AFM) images after exposure and development, overlaid with corresponding simulated aerial image.

Fig. 3.2.6 shows AFM images of negative high-resolution HSQ resist of 40 nm thickness exposed though arrays of circular (Fig. 3.2.6 (a)) and triangular (Fig. 3.2.6 (b)) apertures at 20 µm distance. Excellent agreement with the calculated aerial image is observed.

It is also worth mentioning that the HSQ resist has demonstrated rather high contrast at this wavelength, providing the structures with the edge resolution of 28 nm (measured as a change from 10 to 90 % of the height of the structures). Together with the possibility to tune the distance between the obtained nano-photonic antennae by changing the exposure time, this can allow to obtain novel types of nano-photonic resonators. For example, the exposure through an array of simple triangle apertures at a suitable proximity gap created a set of three-antennae structures with distance between single antennae as small as 100 nm (Fig. 3.2.6 (b)).

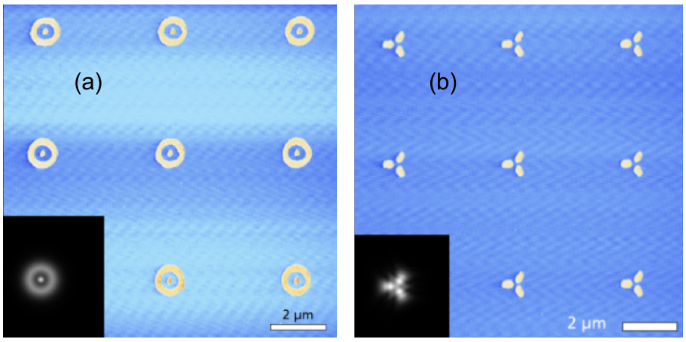

Fig. 3.2.6 AFM images of the resists with 40 nm thickness exposed by EUV proximity lithography for circular (a) and triangular (b) apertures at 20 µm proximity gap. Overlay images show the respective aerial images obtained from simulations.

Good correlation between scalar diffraction simulations and experiments confirms that Fresnel diffraction is the main governing process in EUV proximity lithography of micrometer sized structures.

Overall, the possibility to change the aerial image dramatically and controllably just by changing the proximity gap together with the ability to fine tune the exposed resist area by variation of the exposure time provides a very high degree of flexibility for the exposures. In combination with the developed simulation capabilities this should enable fast and efficient design of suitable transmission masks for wide range of interesting nano-photonic structures including ring-disc cavities [2010 Sonnefraud] or other more complex nano-resonant antennas [2010 Lukyanchuk]. Exercising the gap control with at least a micrometer precision one can therefore achieve reliable non-contact patterning of different structures with nanoscale resolution.

Optical proximity correction

The diffraction-assisted EUV lithography can also be applied to enable the high-throughput and high-quality production of traditional nano-photonic structures, such as bowties. A bowtie is one of the most popular structures in nanophotonics because of its optical properties – efficient radiation coupling and high field enhancement between the electrodes [2006 Sundaramurthy, 2006 Wang, 2008 Kim, 2005 Schuck]. In this study, the mask with apertures of a triangular shape with 1.2 µm height, 44° opening angle and 30 nm distance between two triangles was simulated (Fig. 3.2.7 (a)). The resulting distance between the triangles in the aerial image is strongly depending on the proximity gap between a mask and a wafer. Fig. 3.2.7 (b) shows the resulting aerial image (in x-y plane) at the 5 µm proximity gap (z-axis).

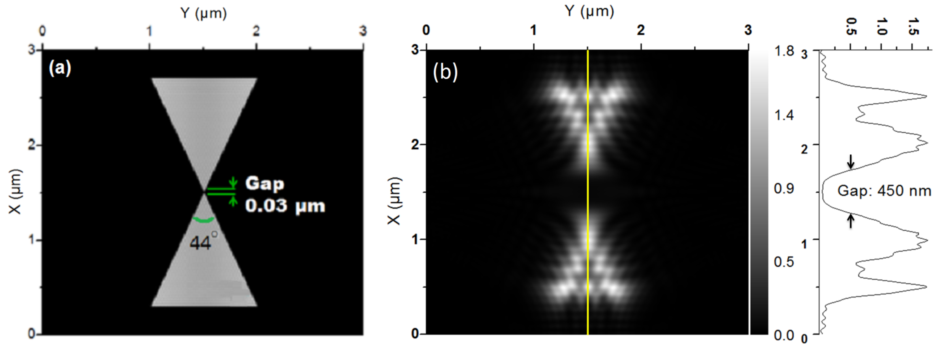

Fig. 3.2.7 (a) Scheme of the simulated bowtie mask, (b) x-y plane intensity image at 5 µm gap.

To achieve a sub-100 nm distance between bowtie electrodes with this traditional mask design, the gap between a mask and a wafer should be maintained at a sub-µm level. At 5 µm mask-to-wafer gap, the minimal achievable distance between electrodes is 450 nm at a fixed level of incoming intensity, see Fig. 3.2.7 (b).

However, with EUV proximity printing traditional techniques of optical proximity correction (OPC) can be used to correct and improve the image. The developed Fresnel diffraction simulation routines can be used to implement an iterative modification of the mask design, realizing significant reduction of the achievable distance between the electrodes of the bowtie. As an example, the modified bowtie mask was simulated with the aim to reduce the distance between electrodes in bowtie structures at the same proximity gap of 5 µm. The modified bowtie element in the mask is designed with overlapping electrodes and the opening angle of the triangle is increased to 90º (Fig. 3.2.8 (a)). As can be seen from the simulation result in Fig. 3.2.8 (b), obtained distance between bowtie electrodes is significantly reduced.

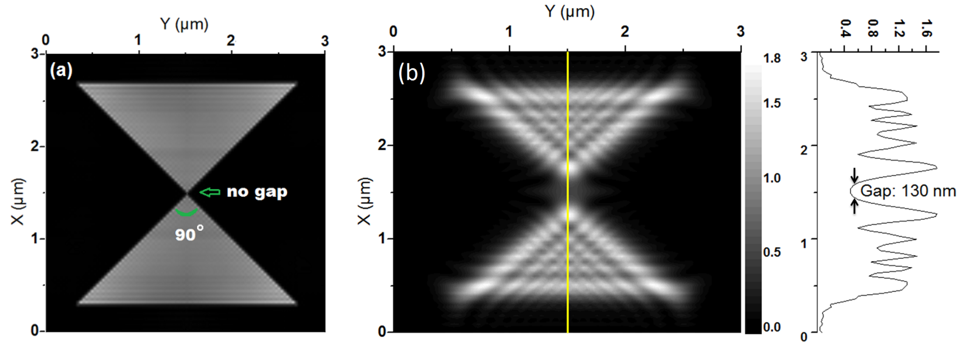

Fig. 3.2.8 (a) Scheme of the modified bowtie mask, (b) aerial image at the 5 µm proximity gap.

The cross section intensity distribution in the Fig. 3.2.8 (b) at the 5 µm proximity gap shows that the achievable distance between the electrodes can be reduced by more than a factor of 3 to 130 nm while maintaining same proximity gap and exposure dose.

It is also worth to note that such a transmission mask is also simple in manufacturing, since reliable production of bowtie arrays with sub-50 nm distance between electrodes is a challenging task even for EBL.

Further iterative optimization of the mask design such as using OPC or other method [2007 Poonawala] may allow one to push the distance between bowtie electrodes to the sub-100 nm range while still maintaining rather relaxed conditions on the distance between mask and wafer, enabling a high-yield production process.

In future, the work will be extended by including a simulation of the transfer of the aerial image into resists. Moreover, the full three-dimensional masks will be rigorously simulated to obtain even more accurate results in close proximity to the mask.

3.2.5 SUMMARY AND CONCLUSION

In summary, the laboratory-scale setup for EUV proximity lithography has demonstrated the ability to create complex nano-antenna arrays and can be used for cost-effective small and medium-scale manufacturing of nano-photonic structures. Utilizing a compact partially coherent DPP EUV source and state of the art positioning systems a knife-edge resolution of 28 nm was achieved. Precise control over the mask-to-wafer gap increases flexibility of the diffraction-assisted EUV lithography, providing the possibility of producing different nanostructures without changing the design of the mask. The established scalar diffraction simulations allowed not only the prediction of the experimental results, but it also opened a way for implementation of optical proximity correction, increasing the quality of structuring and applicability of the method.

3.3 SCALAR DIFFRACTION VS. FDTD

Image formation behind an EUV transmission mask

The optical wave propagation through complex mask features of a dielectric medium is described by electromagnetic theory of Maxwell's equations. The electromagnetic wave fields (E and H) can be determined in a medium and free space. Scalar diffraction can be considered as an ideal case of Maxwell equations. The thin mask approximation (TMA) is assumed that the infinitely thin absorber (thickness = 0), infinitely high absorption k (k=0, or β=1), and no refraction (δ=0) at the boundary. The scalar diffraction method is useful when calculating the large field of a mask and far-field imaging. However, the validity of the scalar approximations is limited due to a specific phase error [2007 Meliorisz].

A transmission mask with feature size of sub 100 nm illuminated by EUV radiation typically requires the rigorous simulation. This is because the absorber thickness of sub 100 nm and substrate thickness of a few tens nm are comparable to wavelength of EUV, and the contrast of transmission between the absorber and substrate is not as high as for the visible and ultraviolet masks.

The finite-difference time-domain (FDTD) is a computational technique to model scientific and engineering problems dealing with electromagnetic wave interaction with material structures [1966 Yee, 1980 Taflove]. Yee described the FDTD numerical technique for solving Maxwell's curl equations on grids staggered in space and time. FDTD is useful to simulate the wave fields with forward time-stepping. The E and H fields are determined at every grid point in space within the time domain. The material of each cell must be specified. Any material can be used as long as the permeability μ (μ_0: the permeability in vacuum = $4\pi\times10^{-7}$ Hm^{-1}), permittivity ε (ε_0: permittivity in vacuum ~ 8.85×10^{-12} F/m), and conductivity are specified. A wide range of linear and nonlinear dielectric and magnetic materials can be modeled. However, FDTD suffers from disadvantages in modeling of a large computational grid, such as for a large field mask with a short-wavelength of light, or far field propagation. In order to reduce the computational time, parallel computation can be considered. FDTD calculates a single polarization state, either TE or TM. The un-polarized light value can be obtained by averaging both TE and TM values [2010 Erdmann].

Here we briefly compare the simulation images calculated by F-K diffraction and FDTD methods. Optical propagation in paraxial and non-paraxial regimes, through single slits and multi-slits, are simulated with coherent EUV radiation.

Mask modelling

The Fresnel-Kirchhoff (F-K) diffraction model assumes that the transmissive diffraction masks are infinitely thin and infinitely opaque in the absorber region, which is known as a thin mask approximation (TMA) as shown in Fig. 3.3.1 (a). On the other hand, the rigorous diffraction model uses the 2- or 3-dimensional layout with the complex refractive index of the material. For an EUV transmission mask, we model the mask features based on what is possible to fabricate in the laboratory. A typical mask model is to use an absorber layer on a high-transmissive substrate (amplitude mask) as shown in Fig. 3.3.1 (b). It is also possible to achieve free-standing masks either by patterning on the low-transmissive substrate (Fig 3.3.1 (c) or by etching or by milling with a focused ion beam after patterning with photoresist (Fig. 3.3.1 (d)).

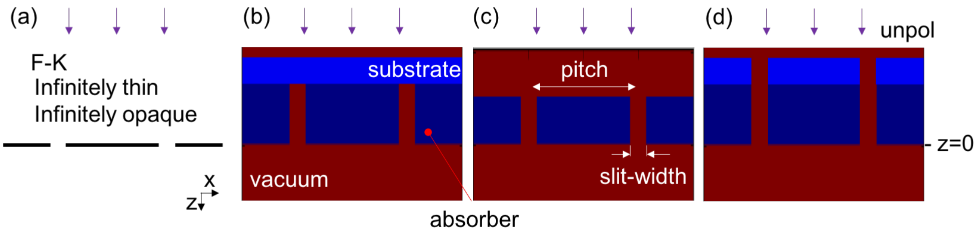

Fig. 3.3.1 The geometries of transmission mask: (a) F-K mask (b) substrate supported mask (c) free-standing mask (d) free-standing mask with substrate support

Isolated object

Optical wave propagation through a wide slit is simulated. The width of the slit was 100 nm and the wavelength of light was 6.7 nm for both scalar and FDTD models. The propagation is simulated in the range of z = 0 to z = 1 μm with corresponding Fresnel number of $N_F = 20$ to $N_F = 1.5$ respectively as shown in Fig. 3.3.2. The compared masks are (a) the TMA of F-K approximation, (b) the FDTD mask consisting of a tungsten (W) absorber with thickness of 200 nm on a Si_3N_4 membrane with thickness of 30 nm, and (c) the FDTD mask consisting of the same material and thickness as in (b) but having free-standing features in the slit area (as in Fig. 3.3.1 (d)). The F-K mask shows finer interference features in the near and far field regime than for FDTD masks. The propagation images of the FDTD masks are smeared due to the finite optical properties.

The free-standing mask yields higher intensity than others, and fine interference fringes have disappeared. The cross-sectional profile at the Fresnel distance of $N_F = 20$ are compared for three masks as shown in the bottom of Fig. 3.3.2. The intensity and the fringe details are slightly changed depending on the simulation method.

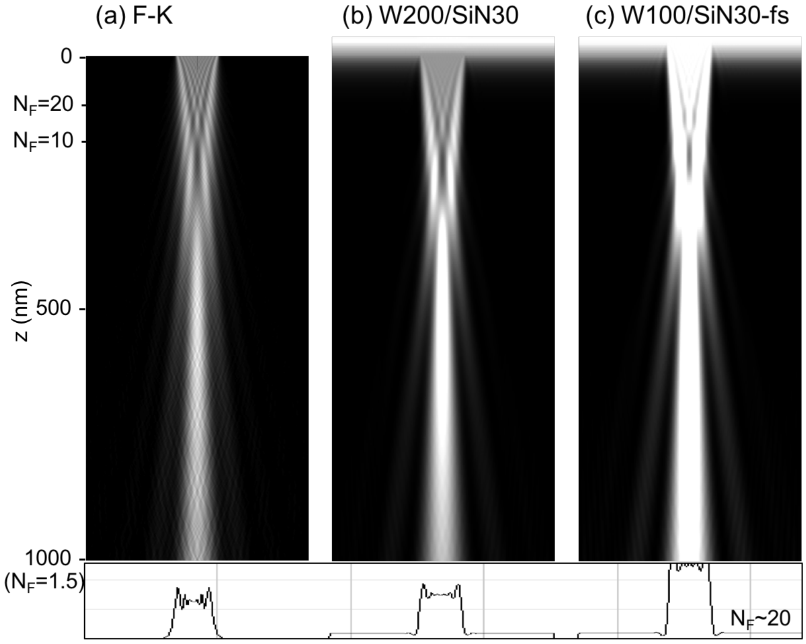

Fig. 3.3.2 The light propagation of the wavelength at 6.7 nm through a wide slit of 100 nm calculated by (a) F-K (b) FDTD with the W absorber with thickness of 200 nm on Si3N4 substrate with thickness of 30 nm, and (c) FDTD with the free-standing W absorber with thickness of 100 nm on Si_3N_4 substrate with thickness of 30 nm: The bottom curves are cross-sectional profiles at the plane where N_F=20

When the slit is narrow, for example a width of 40 nm, the light intensity is significantly reduced and the Fraunhofer diffraction pattern is shown in Fig. 3.3.3. The corresponding N_F is reduced for the same z-distance. The cross-sectional profiles around N_F=20 are compared for three different masks as shown in Fig. 3.3.3. The intensity and the Gaussian intensity profile are different with the different calculation methods.

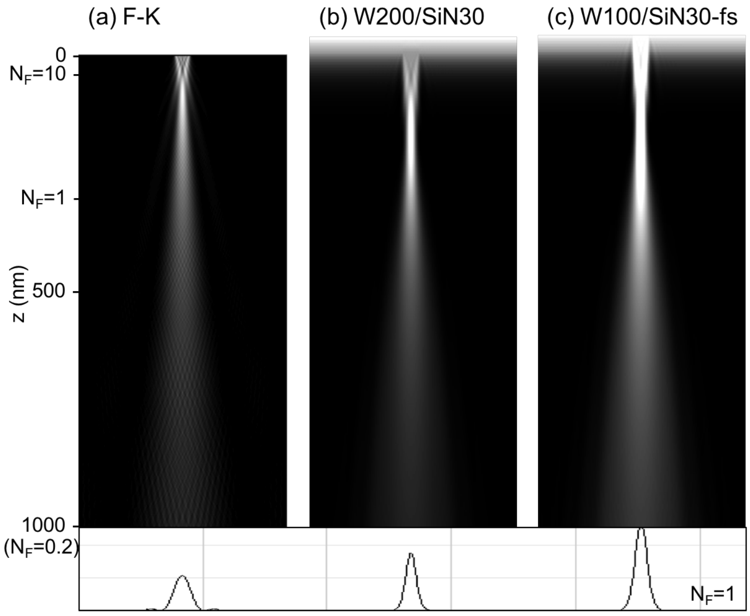

Fig. 3.3.3 The light propagations for wavelength at 6.7 nm through a narrow slit of 40 nm calculated by (a) F-K (b) FDTD of the W absorber with thickness of 200 nm on Si_3N_4 substrate with thickness of 30 nm, and (c) FDTD with the free-standing W absorber with thickness of 100 nm on Si_3N_4 substrate with thickness of 30 nm: The bottom curves are cross-sectional profiles at the plane where N_F=1

Periodic object

For periodic structures, the intensity pattern is in the Fresnel regime as long as the mask field is wide enough. The size of the aperture is equal to the field of the mask. With a finite dimension of mask field, the Fresnel image field is gradually getting narrower as a function of distance from the mask (walk-off). The contribution of the higher diffraction orders is reduced at a further observation plane [1989 Patorski]. Here, the near field diffraction of a periodic object is simulated by scalar diffraction and the FDTD approach. In both approaches, the mask consists of a pitch of 300 nm with a slit-width of 20 nm for coherent illumination with a wavelength of 13.5 nm. The FDTD mask consists of a gold (Au) absorber with thickness of 60 nm supported by a Si_3N_4 substrate with thickness of 20 nm. The FDTD uses TE polarized illumination.

The intensity profiles of the diffraction patterns are compared in the near field regime around 1st Talbot distance (see Chapter 4), and in the regime much closer to the mask. In Fig. 3.3.4, (a) and (b) are the intensity profiles of the interference pattern computed by scalar diffraction and FDTD models respectively. The differences in intensity and contrast exist, however, the position of constructive and destructive interference is nearly identical in the Talbot regime. On the other hand, the field much closer to the mask surface differs between the scalar diffraction and FDTD approaches as plotted in (c) and (d) respectively in Fig. 3.3.4. In the close proximity to the mask, the near-field intensity pattern calculated by different methods differs significantly.

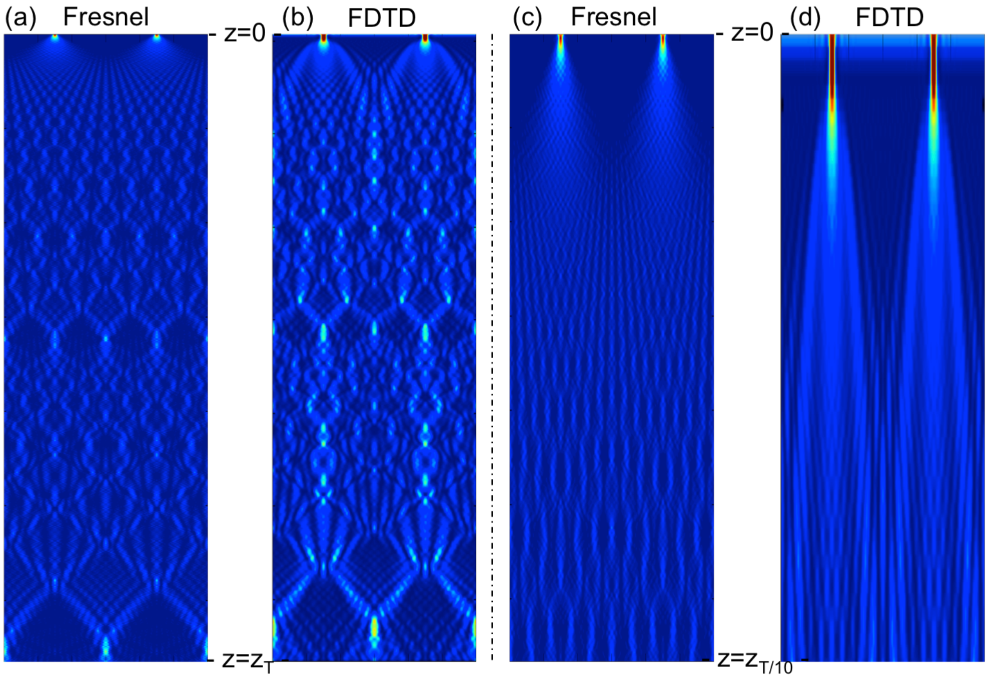

Fig. 3.3.4 Talbot image from the mask composed of 300 nm-pitch, 20 nm-slit-width illuminated by EUV at 13.5 nm wavelength (a, c) F-K diffraction image (b, d) FDTD image, Au 60 nm / Si_3N_4 20 nm

In the previous section, it was shown that the mask layout strongly influences the near-field intensity distribution particularly where no interference between the neighboring slits is present. Here several mask schemes are simulated and compared with the scalar diffraction approach. All the masks consist of a pitch of 100 nm and a slit-width of 15 nm. The radiation field is defined as coherent illumination of wavelength at 6.7 nm. In Fig. 3.3.5 (a), the interference image calculated by scalar diffraction is shown in the z range between z = 0 and z = 747 nm corresponding to fractional Talbot distance of $z_T/4$. The three different mask models are implemented in FDTD calculation: (b) an iridium (Ir) absorber with thickness of 70 nm on Si_3N_4 with thickness of 30 nm, (c) a free-standing mask of W with thickness of 50 nm, and (d) a free-standing mask of W with thickness of 110 nm in Fig. 3.3.5. The intensity and contrast are different of course, but also the profile shapes are different in details. In the bottom of the Fig. 3.3.5, the profiles of the cross section at $z = z_T/6$ are plotted for the particular models. The scalar diffraction shows the intensity profile with good regularity, however, the rigorous calculations show irregular profiles with different intensity and contrast.

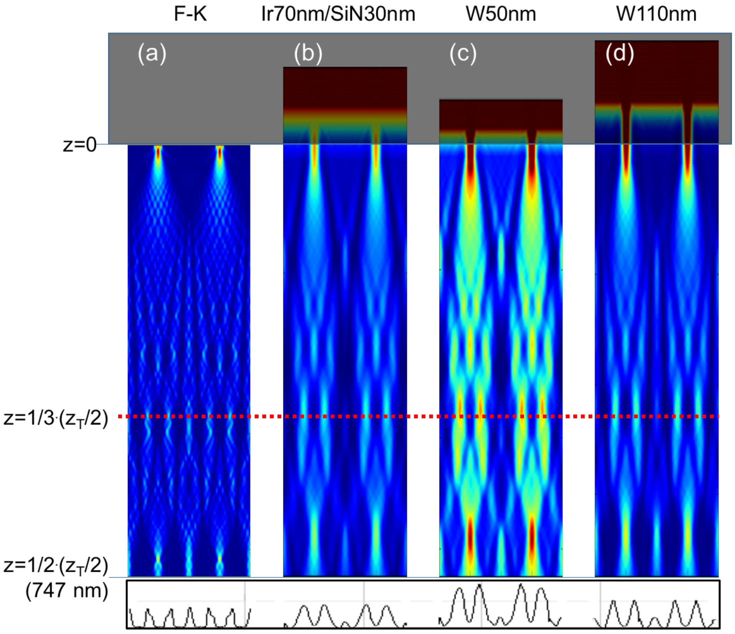

Fig. 3.3.5 The propagated interference patterns calculated by (a) F-K formula and (b-d) FDTD with different mask layouts

In conclusion, different methods of both scalar diffraction and rigorous FDTD simulation are used to calculate optical wave propagations, and the interference patterns are compared for different mask layouts. The propagation of EUV radiation through the isolated objects of wide and narrow slits is simulated. The contrast and intensity are significantly different for both simulation methods[††††]. Also the periodic objects are compared for both methods. In the Fresnel regime of a Talbot image, the phase errors are not significantly different between different simulation methods. The displacement of locations of constructive and destructive interference fringes is small for different simulation methods and mask layouts. However, the field much closer to the mask surface, which is beyond the Fresnel regime, requires one to employ the rigorous simulation with a particular mask layout.

[††††] The difference between both simulation methods arises from the fact that the scalar diffraction method is not valid in the case when the feature size of mask layout is not large enough in comparison to the wavelength of light.

Chapter 4

Diffractive Interference Lithography

4.1 REVIEW OF TALBOT EFFECT

In this section, the Talbot effect and its application are reviewed. Also different methods of Talbot lithography are summarized.

Diffraction grating

In the far field, the diffraction pattern of the plane wave is characterized by Fraunhofer diffraction. In the near-field, however, the interference fringes of diffracted light are characterized by Fresnel diffraction. The diffraction grating is a key element to form the interference fringes that depend on the structure of the elements and the number of the elements of the grating. With an incident angle θ_i, and period of grooves of grating d, the intensity fringes have maxima at angles θ_m as given by the grating equation:

$$m \cdot \lambda = d \cdot (sin\theta_m + sin\theta_i) \qquad (4.1.1)$$

where integer m is called the diffraction order that can be measured in the Fraunhofer regime. In the near-field, the observed intensity fringes are the interference pattern formed by the diffracted beam of all diffraction orders.

Self-image

In the Fresnel diffraction of periodic objects, so called self-imaging phenomenon is encountered [1969 Edgar, 1981 Patorski]. With the coherent illumination of plane wave light, the self-images of periodic objects such as a grating are produced at a regular distance given by:

$$z = n \cdot z_T \ (n=1,2,3\ldots) \qquad (4.1.2)$$

where n is the positive integer. The distance z_T is the so called Talbot distance. Self-imaging means that a particular image is formed without the help of a lens or any other device between object and image [2005 Lohmann].

In 1836, William Henry Fox Talbot first observed that objects with periodic transmission profiles, such as transmission grating or pinhole arrays, illuminated with a white light source produce periodic intensity patterns of different colors resembling the transmission object itself [1836 Talbot]. In 1881, Lord Rayleigh explained this effect for a plane wave interacting with a one-dimensional grating known as the Talbot length [1881 Rayleigh]:

$$z_T = \frac{\lambda}{1-\sqrt{1-(\lambda/d)^2}} \tag{4.1.3}$$

In the paraxial regime, when λ/d is small, it approximates as:

$$z_T = \frac{2d^2}{\lambda} \tag{4.1.4}$$

where d is the period of object. The Talbot effect reproduces images of a periodic object at integer multiples of the half Talbot distance ($n \cdot z_T/2$). The Talbot image was described as the Fresnel diffraction image of a periodic structure. [1956 Cowley, 1965 Winthrop]. There are other positions in the image space where the Talbot effect reproduces images at higher feature density as compared with that of the mask [1979 Flanders, 1996 Berry]. These higher density images are generated at the plane of the fractional Talbot distance given by:

$$\boldsymbol{z = (p/q) \cdot (z_T/2)} \tag{4.1.5}$$

where p and q are co-prime numbers.

During a century after Talbot, the analytical theory of the effect was developed further and extended to Gaussian or spherical illumination wave-front, two-dimensional periodic and quasi-periodic objects and partially coherent sources of finite size. The effect has been successfully utilized for interferometry [1984 Patorski, 1984^a Patorski, 1985 Bolognini], image processing [1986 Anders, 1996 Besold] and structuring [1979 Flanders, 1985 Aristov] applications. An overview of the development of the analytical theory of the effect and its main applications can be found in many scientific articles [1989 Patorski].

The phenomenon is explained as Fresnel diffraction of a periodic object, and is expressed using the angular spectrum with Fourier optics [1969 Edgar, 1996 Goodman, 2011 Voelz]. A one-dimensional transmission grating can be characterized with a pitch (period) and a line width or opening width. A typical grating produces an intensity copy of itself at integer multiples of the Talbot distance, within the limitation that no evanescent fields are present, and so spatial resolution is limited by mask feature size and optical properties for a certain wavelength of light.

In scalar diffraction theory, the amplitude grating has the initial intensity distribution of binary transmittance, u(x, z=0) = 1 in the slit and u = 0 in the line, and the opening width of the grating is much smaller than the half-pitch. The image of the Talbot pattern can be expressed using the angular spectrum representation, within the approximation of the scalar wave equation. The complex field of the monochromatic wave is expressed as E(r, t) = E(r)·exp(iωt), where ω is the angular frequency. The field in a plane at distance z behind a grating, E(r) = E(x, z) (where x is the coordinate perpendicular to the grating rulings, this definition of the x axis is used throughout the chapter), can be expressed as the convolution of the field at the object plane (z=0) and propagator H:

$$E(x,z) = E(x,0) * H(x,z) \tag{4.1.6}$$

The propagator H in space is the inverse Fourier transform of the propagator $\widehat{H}$ in reciprocal space:

$$\widehat{H}(x,z) = e^{i\cdot k_z \cdot z} \tag{4.1.7}$$

where the longitudinal wavenumber is expressed as $k_z = (k^2 - k_x^2)^{1/2}$, where $k = 2\pi/\lambda$. This solution can be expressed in the paraxial approximation, where $\lambda < d$. Thus the expression of E(x,z) is given for Talbot length z_T as following:

$$E(x,z) = \int E(x,0) \cdot \mathrm{e}^{in(2\pi/d)x} \cdot e^{-in(2\pi/z_T)z} dx \tag{4.1.8}$$

where the first term is the initial intensity distribution, the second and third terms are the periodicities in x, z directions respectively [2003 Guerineau].

Talbot image behind finite periodic gratings

In the previous section, we have focused on infinite periodic gratings. However, in reality, a grating consists of the finite number of periods, and the diffraction shadow limits the range where the Talbot pattern can be observed [1984 Patorski]. In the observation plane, diffracted waves with a small number of diffraction orders contribute to the image formation. In the paraxial regime, the most efficient diffractions are 0^{th} and $\pm 1^{st}$ diffraction orders [2010 Kim]. Fig. 4.1.1 illustrates the diffraction shadow by diffraction of up to $\pm 1^{st}$ diffraction orders. The overlapping area (triangular zone of red dot in Fig. 4.1.1) is the useful region for forming a Talbot pattern efficiently.

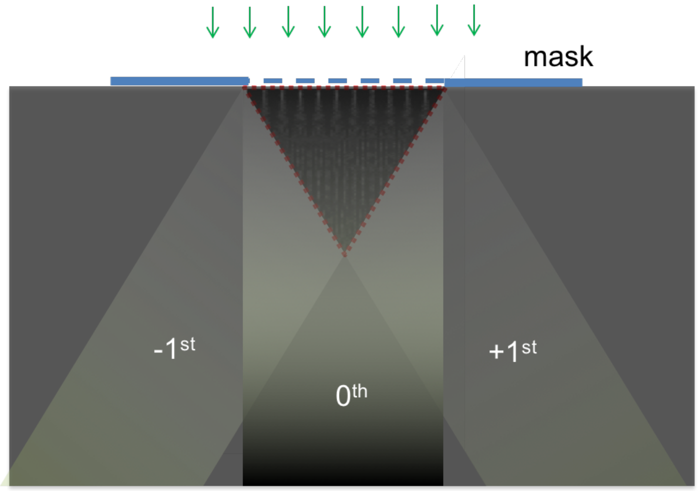

Fig. 4.1.1 The diffraction shadow by diffraction orders behind the grating of finite dimension

Talbot lithography

Talbot lithography is an interference lithography technique, which records the self-image, the fractional Talbot pattern, or the Fresnel images between the Talbot planes. Typically, a coherent plane wave illuminates through the transmissive grating, and the image is printed on the photoresist.

The use of EUV radiation for Talbot lithography is an emerging technique due to the short wavelength nature, and capability of producing nano-patterns. Various applications in nano-fabrication are presented. Talbot lithography with EUV illumination has been used for replicating complex structures [2009 Isoyan], for the demonstration of defect tolerant lithography [2012 Urbanski, 2013 Li], for high-resolution patterning of large-area samples [2012 Wang], and for patterning with spatial frequency multiplication (M_{sf}) up to a factor of 2 using the achromatic Talbot effect [2014 Mojarad, 2013 Danylyuk]. The fractional Talbot effect was demonstrated for 1D structuring with soft X-rays [2014 Kim] and observed for 2D patterns using microlens arrays with laser illumination in the visible spectral range [1997 Besold], several analyses on Talbot effect are well summarized in [2013 Wen].

4.2 FABRICATION OF TALBOT MASKS

Proximity lithography, Talbot lithography, or diffractive interference lithography require a precisely produced transmission mask. The most efficient method of fabricating the mask depends on the purpose e.g. producing a large field, a thin mask, or a free-standing structure. This section introduces a few useful techniques of fabrication for transmission masks including traditional and new techniques.

E-beam lithography for Talbot masks

Traditional X-ray transmission mask is often fabricated by E-beam lithography. The E-beam tool directly writes any geometrical feature on a photoresist coated membrane. Typical material of the membrane is Si_3N_4 or Si depending on the wavelength of the radiation. The writing field area is around 300 μm × 300 μm. The resolution depends on the beam size and is typically on the order of a few tens of nanometers. Thus, it is suitable to fabricate the Talbot masks or the proximity lithography masks with a pitch down to 50 nm. The exposure latitude of E-beam lithography is large when using the transmissive membrane, because the thickness of the membrane is only a few tens of nanometers and no significant back scattering is expected, which is different from exposing a thick Si substrate. The process following E-beam writing is the typical lithography process including the development, drying, and etching.

Fig. 4.2.1 is an example of the grating masks with different sizes produced by e-beam lithography. The Si substrates having thickness of 100 nm were deposited with PMMA photoresist with thickness of 60 nm by spin-coating. The e-beam wrote the grating features with the exposure dose of 1000 μC and the sample was developed. For feature sizes below 40 nm, significant distortion of the pattern occurs such as increased line-edge roughness.

The mask shown in Fig. 4.2.1. might be useful for fractional Talbot lithography with EUV radiation of wavelength at 46.9 nm produced by an argon capillary discharge laser. The remaining photoresist can be used as an absorber at this wavelength resulting in high-contrast between the substrate and the absorber.

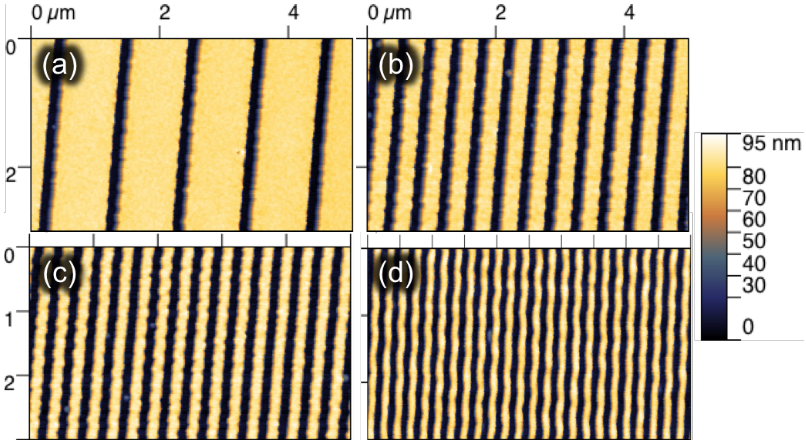

Fig. 4.2.1 AFM images of the grating masks produced by e-beam lithography (a) 1 µm pitch with 100 nm slit-width (b) 400 nm pitch with 80 nm slit-width (c) 300 nm pitch with 60 nm slit-width (d) 200 nm pitch with 40 nm slit-width

Focused Ion Beam milling for Talbot masks

The focused ion beam (FIB) can be used to locally remove or mill away some part of the material with the sputtering action of the ion beam [2007 Volkert]. The FIB milling technique is often used to modify lithography masks when there are a few defects on the surface are present. In laboratory demonstrations, FIB is also a useful tool to fabricate transmission masks for Talbot lithography or proximity lithography. FIB can write with high resolution. The spot size is in the order of only a few nanometers (< 5 nm). It can write any features directly on any material from polymer to metal. Heavy ions, such as gallium ions, remove the atoms by either elastic or inelastic collisions.

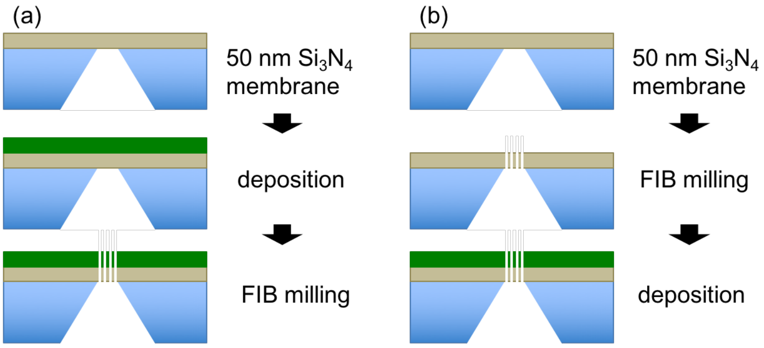

Fig. 4.2.2 Fabrication processes with FIB milling (a) FIB milling after absorber deposition (b) the FIB milling before deposition

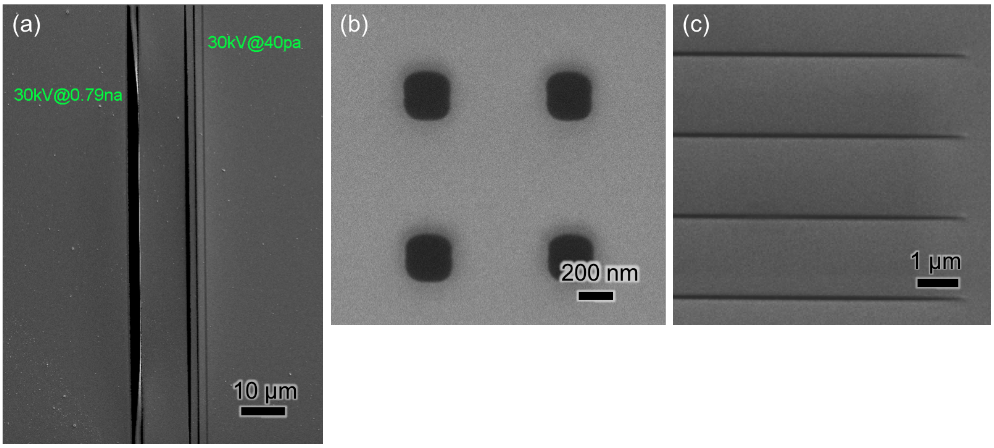

Fig. 4.2.3 The SEM images of the fabricated masks by FIB milling (a) the line milling with different parameters of beam current (b) the FIB milling on the Si 100 nm substrate (c) gold deposited grating of 100 nm slit-width after FIB milling on Si

A disadvantage of FIB milling, however, is the slow milling time. The speed of removing the target material highly depends on the atomic or physical properties of the material such as atomic number (weight), ultimate tensile strength. The milling time is proportional to the area or the volume of the milling field. One idea to reduce the unnecessary milling time is to cut along the edge of apertures. Typically, the whole area of the aperture is milled through completely. Instead, if only the edge of the aperture is milled, the whole aperture will drop down resulting in removing the whole aperture. Fig. 4.2.4 (a) shows the scheme of the FIB milling along the edges of the square apertures. The milling time will be reduced proportionally to the milling area. Fig. 4.2.4 (b) is the SEM image of the Si membrane after the FIB writing. The corners of the square apertures are very sharp in comparison to the manner to mill the whole aperture in Fig. 4.2.3 (b). One problem of this method is that the cut square that has to drop down is sometimes hanging up and folds. In this case additional FIB milling is required to completely remove them.

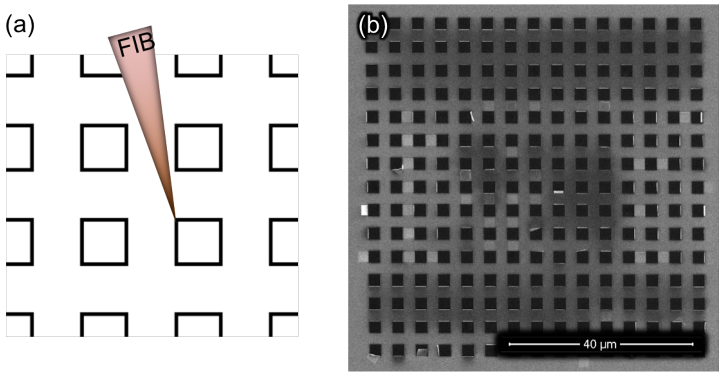

Fig. 4.2.4 (a) The scheme of the FIB milling along the edges of the squares (b) SEM image of the 2D square grating fabricated by the method

In conclusion, this section introduces the fabrication techniques for the EUV transmission masks. E-beam lithography is useful to fabricate large field masks. The FIB method can fabricate EUV transmission masks with high-resolution down to sub 10 nm scales. The FIB milling method is suitable for laboratory purposes due to the low speed. The alternative method to reduce the milling time in the FIB is introduced and demonstrated.

Chapter 5

Coherent EUV Talbot Lithography

5.1 FRACTIONAL TALBOT LITHOGRAPHY WITH AN EUV LASER

The fractional Talbot effect leads to a possibility to implement patterning of structures with smaller periods than that of the master mask. This is particularly attractive when using short wavelength illumination in the extreme ultraviolet due to attainable resolution in the sub-100 nm range. In this chapter we demonstrate Talbot lithography with the fractional Talbot effect under coherent illumination generated with a capillary discharge Ne-like Ar extreme ultraviolet laser. Various spatial frequency multiplications up to 5x are achieved using a parent grating. This technique allows fabrication of nano-structures with high-resolution patterns, which is of high interest in many applications such as manufacturing of plasmonic surfaces and photonic devices.

5.1.1 INTRODUCTION

In order to achieve smaller structures in Talbot lithography, high-resolution masks fabricated with smaller periods are required. This fact imposes a limitation towards the printing of smaller feature sizes due to the challenge of producing large area, high quality and small period masks compatible with EUV illumination [2012 Brose].

To overcome this obstacle, we investigated the use of the fractional Talbot effect in Talbot lithography focusing on finding the alternative scaling of structures. The Fractional Talbot effect describes the interference pattern not only at the integer multiples of the Talbot distance, $n \cdot z_{T,}$ but also at other intermediate planes located at fractional Talbot distances. Particularly clear line and space patterns can be found at rational numbers of the half Talbot distance, $z = (p/q)(z_T/2)$, where p and q are co-prime numbers [1996 Berry]. The effect leads to fractional interference patterns from the parent mask for various spatial frequency multiplication (M_{sf}). While various imaging applications and analysis are reported on the fractional Talbot effect [2013 Wen, 1965 Winthrop], however, in structuring, fractional Talbot lithography was reported only with visible light and hard x-rays [1994

Arrizon]. Herein we demonstrate fractional Talbot lithography in the EUV utilizing a compact EUV laser source, resulting in various M_{sf} up to $M_{sf} = 5$ from one parent mask.

5.1.2 THEORY AND METHODOLOGY

The fractional Talbot pattern can be analytically expressed using the angular frequency representation [1979 Flanders]. The binary transmittance, $E_0(x) = 1$ in the slits and $E_0(x) = 0$ at the absorber, is considered as an initial intensity distribution at the mask plane (z=0), where x is the axis of initial intensity distribution of grating and z is the axis of propagation of the plane wave illuminating the mask. In the paraxial limit, the angular frequency representation is identical with the framework of Fourier optics. The optical field, E(x, z) is described with the inverse Fourier transform of a propagator, $\hat{H}(k_x, k_z; z) = \exp(i \cdot k_z \cdot z)$ in reciprocal space, where the longitudinal wavenumber is $k_z = (k^2 - k_x^2)^{1/2}$, with the wavenumber $k = 2\pi/\lambda$, thus $E(x, z) = E_0(x, z{=}0) * H(x, z)$. The intensity profile as a function of distance is illustrated in Fig. 5.1.1 (a).

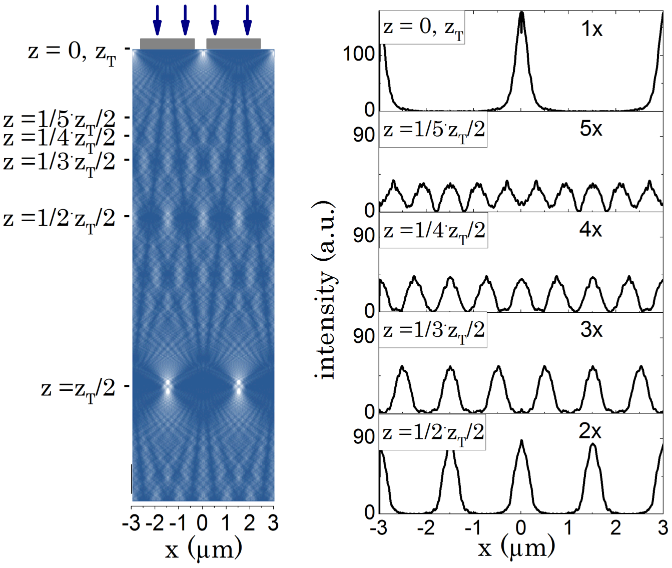

(a) (b)

Fig. 5.1.1 (a) The Talbot pattern behind a grating with narrow slits (500 nm per 3 µm pitch) as a function of distance from a grating (b) the intensity profiles at several distances indicating M_{sf} – note that the cross-section data are averaged with 10 computational pixels.

Fractional Talbot images having positive integer M_{sf} values (1x, 2x...) are formed at z positions equal to fractional Talbot distances according to the following relations (also, see Fig. 5.1.1 (a, b)):

$$
\begin{aligned}
&1x:\ \text{at } z = (1/1)\cdot n\cdot(z_T/2),\ 0\\
&2x:\ \text{at } z = (1/2)\cdot n\cdot(z_T/2)\\
&3x:\ \text{at } z = (1/3)\cdot n\cdot(z_T/2),\ (2/3).n.(z_T/2)\\
&4x:\ \text{at } z = (1/4)\cdot n\cdot(z_T/2),\ (3/4)\cdot n\cdot(z_T/2) \qquad (5.1.1)\\
&5x:\ \text{at } z = (1/5)\cdot n\cdot(z_T/2),\ (2/5)\cdot n\cdot(z_T/2),\\
&\qquad\qquad (3/5)\cdot n\cdot(z_T/2),\ (4/5)\cdot n\cdot(z_T/2)\\
&\qquad\qquad\qquad \ldots\ (n=1, 2, 3\ \ldots)
\end{aligned}
$$

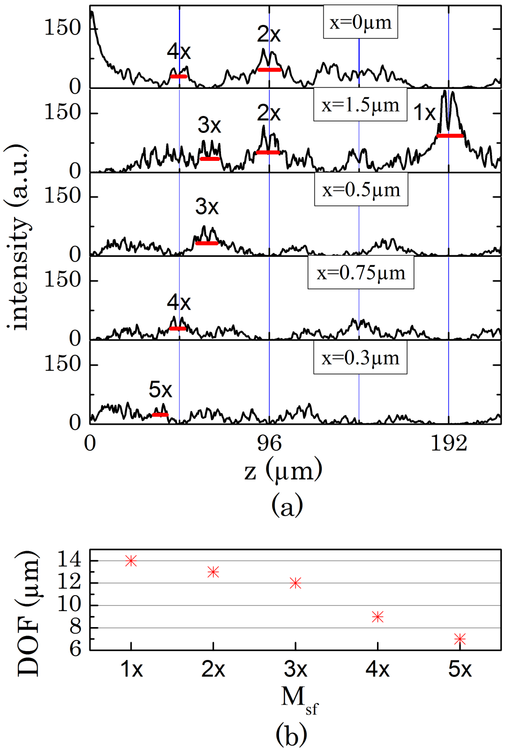

Fig. 5.1.2 (a) Profiles of the Talbot pattern in the 'Fig. 5.1.1 (a)' along the radiation propagation axis at various x-positions with indication of M_{sf}, and (b) the DOF for different M_{sf}. [Note that measured number of DOF values for a desired M_{sf} equals M_{sf}, and each values are slightly different. The DOF values presented in (b) are minimum ones among those values.]

The distance between the mask and the sample has to be precisely controlled, within the depth of field (DOF) of the pattern to achieve the desired M_{sf}. The DOF for the desired M_{sf} is given approximately by:

$$\frac{1}{2}\frac{z_{Msf-1}-z_{Msf+1}}{2} \approx \frac{p^2}{2\lambda(M_{sf}^2-1)} \qquad (5.1.2)$$

where $z_{Msf} = 1/M_{sf.}(z_T/2)$ [1979 Flanders]. The DOF can be estimated from the simulation by measuring the peak intensity distribution of the Talbot pattern or Talbot carpet along the radiation propagation direction [2009 Case]. The Fig. 5.1.2 (a) shows profiles of the

Talbot image along the radiation propagation axis for several x-positions of Fig. 5.1.1 (a). The profiles indicate the intensity range of the pattern for the desired M_{sf}. The DOF corresponds to the full-width at half-maximum (FWHM) of each peak for the respective M_{sf} (see the red lines in Fig. 5.1.2 (a)). The Fig. 5.1.2 (b) shows values of DOF at different M_{sf} from 1x to 5x. As expected, for the higher M_{sf}, the pattern yields shorter DOF, which makes distance control more critical.

5.1.3 RESULT AND DISCUSSION

Table-top coherent EUV source

A capillary discharge Ne-like Ar laser at λ = 46.9 nm was used for exposures in experiments. This laser provides high spatial and temporal coherence, which are required for this work. The spectral bandwidth was approximately $\Delta\lambda/\lambda = 3.5\text{x}10^{-5}$ [2012 Urbanski], and the spatial coherence radius was 500 μm at the mask plane [2001 Liu, 1997 Marconi]. The exposure dose at the wafer plane in the experiments was 0.1 - 0.3 mJ/cm^2/pulse [2013 Li].

Talbot masks

The transmission grating (or Talbot mask) was fabricated using focused ion beam (FIB) milling. A Tungsten probe tip was used to generate the Ga^+ ion beam. The beam current was 80 pA and the dwell time was 1 μs during the process. The grating structure was defined on a Si_3N_4 (50 nm thickness) membrane deposited with Au (130 nm thickness) that was fully milled through to make 20 slits and to achieve free standing array structures as shown in Fig. 5.1.3. (b). In total, 20 pairs of the absorbing and opening lines were created with 3 μm pitch over a total area of 60 μm x 50 μm. The number of pairs was enough to demonstrate the fractional Talbot effect even though the line width roughness and the out-of-plane bending of the lines impacted the quality of results. The length of the lines was 50 μm and the width of the slits was ~ 500 nm in average (see Fig. 5.1.3 (a-c)).

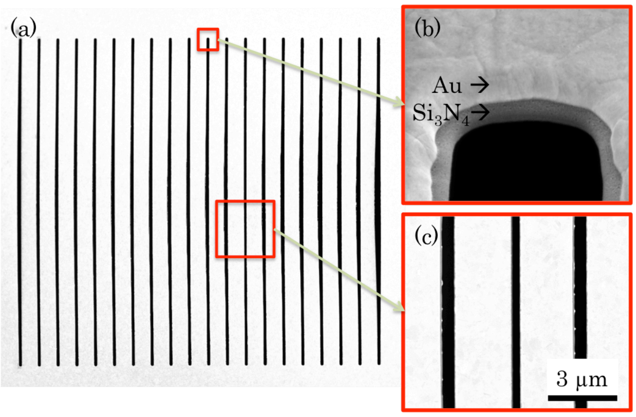

Fig. 5.1.3 The free standing transmission grating of narrow slit array formed on the Au deposited Si$_3$N$_4$ window (a-c). Zoom-in views at the end of a slit (b) and in the middle (c).

The grating was illuminated by the EUV laser to form the fractional Talbot pattern. A positive-tone photoresist (polymethyl methacrylate - PMMA) with an approximate thickness 80 nm was deposited by spin coating on a Si wafer that was placed behind the mask at the corresponding fractional Talbot distances in order to achieve the desired demagnification, M_{sf}. The distance of the proximity gap was measured using the contact signal between the mask and the wafer. The exposure dose was set at 100 shots (around 20 mJ/cm^2) through the experiment. After the exposure, the photoresist was developed with MIBK (Methyl isobutyl ketone) : IPA = 1 : 3 for 45 sec and cleaned with IPA for 45 sec.

The experimental results corresponding to the prints at the different fractional Talbot distances are summarized in Fig 5.1.4, which are image data obtained using the atomic force microscope (AFM), showing the fractional Talbot lithography results of $M_{sf} = 1$ (a), $M_{sf} = 2$ (b), $M_{sf} = 3$ (c), and $M_{sf} = 5$ (d) with corresponding pitches of 3 µm, 1.5 µm, 1 µm and 600 nm respectively. In Fig. 5.1.4 (a) the narrow slit on mask is transferred into the wafer due to replication of the Talbot effect, Fig. 5.1.4 (b) shows doubling of M_{sf}. In Fig. 5.1.4 (c) small destructive interference at peaks can be noticed, because the wafer position was not exactly at $z = z_{Msf=3}$, and in Fig. 5.1.4 (d) line-edge roughness and out-of-plane bending of the parent mask start to degrade a quality of the pattern. However, the obtained results clearly show the expected multiplication factor at the frequency corresponding to the fractional Talbot effect.

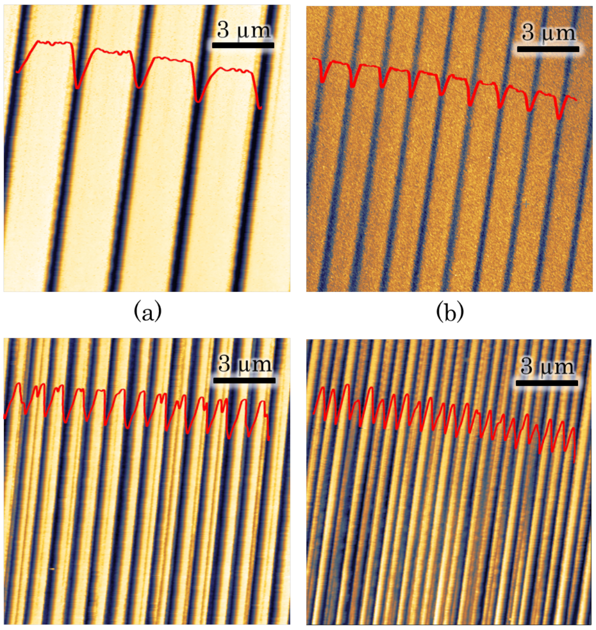

(a) (b) (c) (d)

Fig. 5.1.4 The AFM measurements of the lithography results showing (a) $M_{sf} = 1$, (b) $M_{sf} = 2$, (c) $M_{sf} = 3$, and (d) $M_{sf} = 5$ from the parent mask of 3 µm pitch. Overlayed red curves are corresponding AFM cross-sections. The height of the PMMA structures (a-d) was ~ 80 nm.

The widths of developed or removed parts were approximately ~ 570 nm (a), ~ 320 nm (b), ~ 310 nm (c) and ~ 210 nm (d) at FWHM of the height, while the corresponding simulated values were respectively 670 nm, 840 nm, 780 nm and 840 nm at FWHM of intensity. According to the simulation data, the width is supposed to be comparable to the slit width of parent mask. The difference between the calculated values and the experiment data can be explained by variations in the illumination dose proper of the pulsed nature of the EUV laser and non-linear response of the photoresist. The EUV transmission at 46.9 nm wavelength is reduced approximately by half every 10 nm thickness of PMMA [1993 Henke]. It also should be taken into account that peak intensity is changing as a function of M_{sf}. The advantage of obtaining high M_{sf} with fractional Talbot lithography is opposed by the fact that intensity reduces with increasing M_{sf} as shown in Fig. 5.1.5. The intensity values from simulations (blue squares) and developed depth of the photoresist from experiments (red circles) are both decreasing for higher M_{sf} as expected.

Fractional patterning with spatial frequency multiplication will be useful for applications that require large area and high-resolution patterning, relaxing the fabrication constrains for the master mask. It is also convenient and efficient when various sizes have to be printed using one mask in EUV patterning.

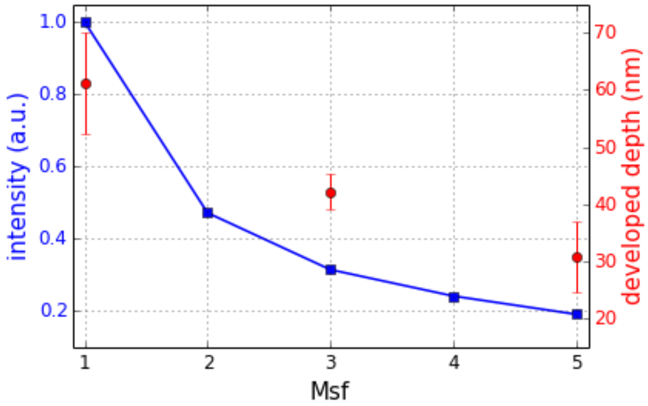

Fig. 5.1.5 Intensity change in simulation (square blue) and developed depth of PMMA as a lithographic result (circle red) as a function of M_{sf}

5.1.4 CONCLUSION

We have demonstrated fractional Talbot lithography experimentally using highly coherent EUV illumination at 46.9 nm wavelength generated with the capillary discharge Ne-like Ar laser. Spatial frequency multiplications up to 5x were achieved with pitches of 3 μm, 1.5 μm, 1 μm and 600 nm respectively from the parent grating of 3 μm pitch. The grating mask is highly transmissive with a free-standing structure fabricated by FIB milling. However, the line width roughness and the out-of-plane bending of the lines must be improved for better quality of the printing over large areas. We envision that a grating with smaller pitch size could be used for further reduction of period and feature-size as well as the grating with narrower slits could be used to get higher M_{sf} values, more than M_{sf} = 5x. Also the utilization of recently developed EUV lasers in the vicinity of 13 nm can decrease further the feature size achievable with this patterning approach [2010 Alessi].

5.2 OPTICAL PROPERTIES OF 2D FRACTIONAL TALBOT LITHOGRAPHY

We investigate optical properties of two-dimensional (2D) fractional Talbot patterns under illumination with EUV laser light. The fractional Talbot effect, due to spatial frequency multiplication, can enable patterning of micro and nano-structures with various feature sizes using a micro-scale pitch mask. The experiment is performed with a free-standing mask fabricated by focused ion beam milling and a highly coherent illumination at 46.9 nm wavelength generated by a compact capillary discharge Ne-like Argon laser. As a result of spatial frequency multiplication, the structure density of a square array of apertures in the mask was increased by a factor of up to 9 at the recording plane. The depth of field of the fractional Talbot images has been investigated using Fresnel diffraction analysis. Added field distribution complexity caused by asymmetry of the 2D arrays was observed both in simulation and in the experiment. This approach could be useful for sub-micron structuring of 2D patterns for various applications including among others the fabrication of photonic crystals, quantum dots, and also of submicron-electronic devices.

5.2.1 INTRODUCTION

Fractional Talbot lithography with EUV has several advantages. For example, the short EUV wavelength reduces the resolution constraints imposed by the diffraction limit as compared with deep-ultraviolet lithography [2013 ITRS, 2007 Wurm]. Additionally, it reduces photoelectron scattering in the photoresist, which is a limitation for X-ray lithography [1995 Okazaki]. The multiplication factor that can be achieved in fractional Talbot lithography relaxes the mask fabrication requirements regarding the pitch size as compared with traditional (1x) Talbot lithography [2012 Brose]. Fractional Talbot lithography has the capability to produce complex 2D patterns, which can potentially be useful for fabrication of many applications such as photonic crystals, quantum dots and nano-antennae [2006 Ozbay, 1996 Krauss, 1988 Reed].

In the previous section, we demonstrated spatial frequency multiplication in one-dimension by a factor of 5 using fractional Talbot lithography with coherent EUV illumination [2014 Kim]. In this section, we extend the method to the two-dimensional arrays of rectangular structures and analyse achievable frequency multiplication levels and corresponding depth of field both theoretically and experimentally. For the latter a square array mask is illuminated by coherent EUV radiation with a wavelength of 46.9 nm generated by a capillary discharge Ne-like Ar laser.

5.2.2 THEORY AND METHOD

Fractional Talbot effect in 2-dimension

Fig. 5.2.1 illustrates the fractional Talbot lithography approach. While a wafer placed at half the Talbot distance prints a replica of the Talbot mask, if the wafer is located behind the mask in the fractional Talbot planes prints of multiplied density of mask pattern can be obtained.

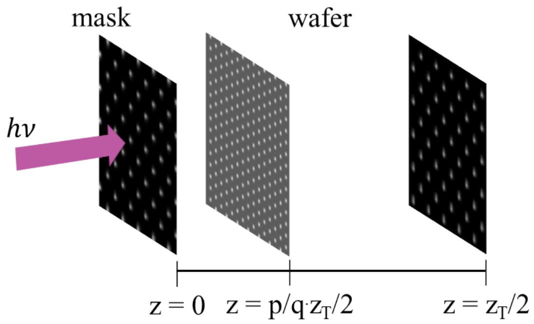

Fig. 5.2.1 An illustration of the fractional Talbot lithography arrangement.

Talbot images with Fresnel analysis

The diffraction pattern of a periodic array is defined under the Fresnel-Kirchhoff approximation. The diffracted light field is calculated as a function of the distance, utilizing for its evaluation the fast Fourier transform method [2010 Schmidt].

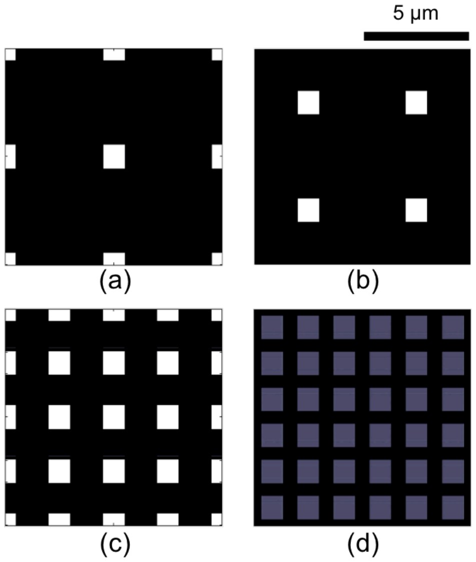

Fig. 5.2.2 Simulated images of the fractional Talbot pattern at (a) $z = 0$ or mask, (b) $z = z_T/2$, (c) $z = 1/2 \cdot (z_T/2)$ and (d) $z = 1/3 \cdot (z_T/2)$ with corresponding multiplications, (a, b) $M_{sf}^2 = 1$, (c) $M_{sf}^2 = 4$ and (d) $M_{sf}^2 = 9$ respectively.

Fig. 5.2.2 illustrates the calculated images of fractional Talbot patterns generated with a mask of 5 μm pitch. The different images correspond to the intensity at $z = 0$ (a), $z = z_T/2$ (b), $z = (1/2)\cdot(z_T/2)$ (c) and $z = (1/3)\cdot(z_T/2)$ (d) with corresponding 2D spatial frequency multiplications, $M_{sf}^2 = 1$ (a), $M_{sf}^2 = 1$ (position of intensity pattern is shifted) (b), $M_{sf}^2 = 4$ (c) and $M_{sf}^2 = 9$ (d) respectively.

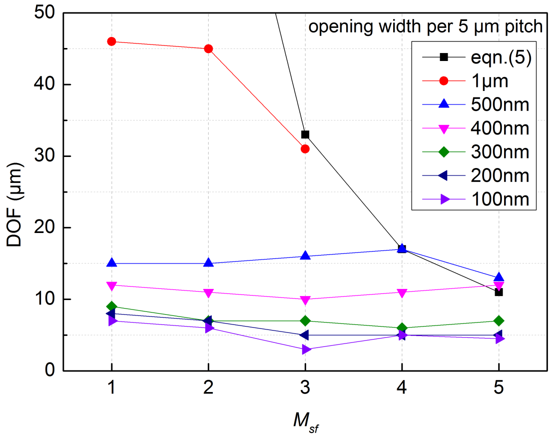

Fig. 5.2.3 The calculated DOF for different opening widths and various M_{sf} obtained with the Fresnel approach described in [2014 Kim] [Note: eqn. (5) refers to eqn. (5.2.1)]

The calculated intensity distributions shown in Fig. 5.2.2 assume a precise distance between the mask and the image plane (wafer). However, in a practical implementation of the fractional Talbot lithography, the distance between the mask and the wafer has to be adjusted within the depth of field (DOF) of the mask. The DOF depends on mask pitch, illumination wavelength and the desired magnification factor M_{sf}, and is defined as following:

$$\boldsymbol{DOF} = \frac{\boldsymbol{d^2}}{\boldsymbol{2\lambda\left(M_{sf}^2 - 1\right)}} \tag{5.2.1}$$

where d is pitch of the array [1979 Flanders]. The analytical solution in equation (5.2.1), which is independent on opening width, demonstrates DOF decrease with the increase of M_{sf}. This correlates with the result obtained in the Fresnel approach for 5 μm pitch and 1 μm opening width, but not for smaller openings, where DOF is not changing significantly for different magnification levels (Fig. 5.2.3). It is important to note that the value of DOF can be changed with the different opening width. This is especially important for 2D patterns, where opening can have different dimension in two directions, producing complex field distribution both in-plane and in z-direction.

In the experiment, the positioning error, dz has to be controlled within DOF in order to achieve the fractional Talbot pattern for desired M_{sf}. The z-distance for desired M_{sf} is given by:

$$z = z_{(Msf)} \pm dz \tag{5.2.2}$$

where $z_{(Msf)} = p/M_{sf} \cdot (z_T/2)$, p and M_{sf} are same co-prime numbers as in equation (5.2.1).

5.2.3 EXPERIMENT

Talbot mask

A Talbot mask was designed to test the fractional Talbot lithography with a magnification factor M_{sf}^2 larger than 4. The maximum M_{sf} value of the fractional Talbot pattern is limited by (pitch/width–1), where the width stands for a width of the mask transmissive zone (in case 'pitch/width' is not an integer, counting any fractional remainder as one). Thus, for a 2D array, the limit is $M_{sf}^2 = (\text{pitch/width}-1)^2$. We designed a mask with a pitch of 5 μm and the width of the transmissive zone of 1 μm. Thus, the maximum M_{sf}^2 is 16.

The mask was designed with a square array formed over an area of 100 μm × 100 μm. Each square was 1 μm × 1 μm (width) in 5 μm × 5 μm unit (pitch). Low stress Si_3N_4 membrane (50 nm thickness) samples were manufactured by Norcada Inc., Canada. The membrane was covered with 130 nm thick gold layer by electron beam physical vapor deposition (EBPVD). The square aperture array was manufactured by focused ion beam (FIB) milling of the sample in order to form a free-standing structure.

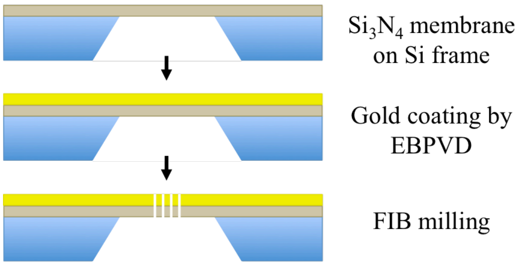

Fig. 5.2.4 Fabrication process for the Talbot mask

Fig. 5.2.4 shows a schematic diagram of the fabrication process. The fabrication of the 2D arrays leads to more stable results than in the case of previously manufactured one-dimensional structures [2014 Kim]. In the FIB tool a Gallium probe tip was used to generate the Ga+ ion beam. The beam current was 80 pA with dwell time of 1 μs during the process. Due to imperfections of the FIB milling process, the mask pattern that has been formed consisted of rectangular structures of to 1.1 μm × 1.35 μm size instead of squares, which limited the achievable multiplication factor to $M_{sf}^2 = 9$ in the experiment. Fig. 5.2.5 shows the scanning electron microscope (SEM) image of the mask with zoomed-in images at the edge of one square aperture at the top-right inset and 3×3 holes section area at the bottom-right.

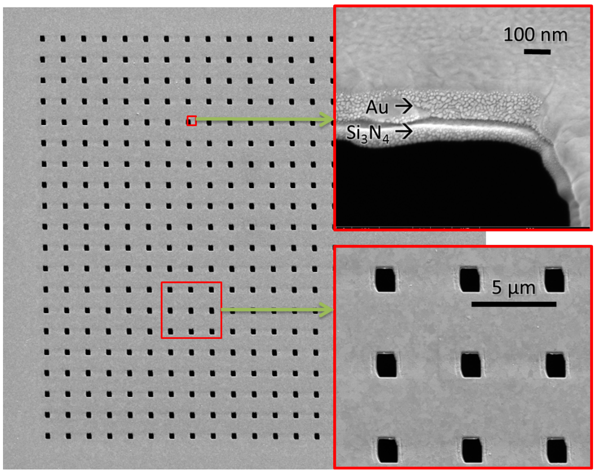

Fig. 5.2.5 The Talbot mask for fractional Talbot lithography that contains free-standing structure in the square array. The pitch was 5 μm and the width was 1 μm approximately

Lithography process

The exposure was performed under vacuum, with a background pressure of ~ 10^{-5} mbar. Beforehand, a Si wafer was spin-coated with a positive-tone photoresist (poly-methyl methacrylate, PMMA) with a thickness of about 100 nm and baked at 180° for 2 minutes on a hotplate. This photoresist sample was located at distances $z = (1/3)^{\cdot}(z_T/2)$ from the mask to achieve $M_{sf}^2 = 9$ ($M_{sf} = 3$). In our experimental system, the absolute positioning of the wafer with respect to the mask has a limited accuracy leading to deviations of resulting patterns between experiments. Nevertheless, in a single experiment the relative positioning is controlled to within 10 nm range. Also the tilt is accurate to within 1 μrad, which is precise enough for the purpose of the experiment. The exposure dose was ~ 20 mJ/cm^2 (approximately 100 laser shots) at an operating frequency (repetition rate) of 1-3 Hz. After the exposure, the photoresist was developed with MIBK (4-Methylpentan-2-one) : IPA (2-Propanol) = 1 : 3 for 45 seconds and cleaned with IPA for 45 seconds.

5.2.4 RESULTS

2D fractional Talbot patterns

The lithography samples were analysed using an atomic force microscope (AFM). Fig. 5.2.6 shows the result of the fractional Talbot lithography that achieved $M_{sf}^2 = 9$ ($M_{sf} = 3$) with a corresponding pitch of 1.7 µm × 1.7 µm using the parent mask of 5 µm × 5 µm pitch. In the figure, the simulated image (a) is compared with the experimental result: top-view (b) and 3D-view (c). The elongated squares at the mask, as shown in Fig. 5.2.5, produced elongated squares at the wafer for both simulation and experimental results.

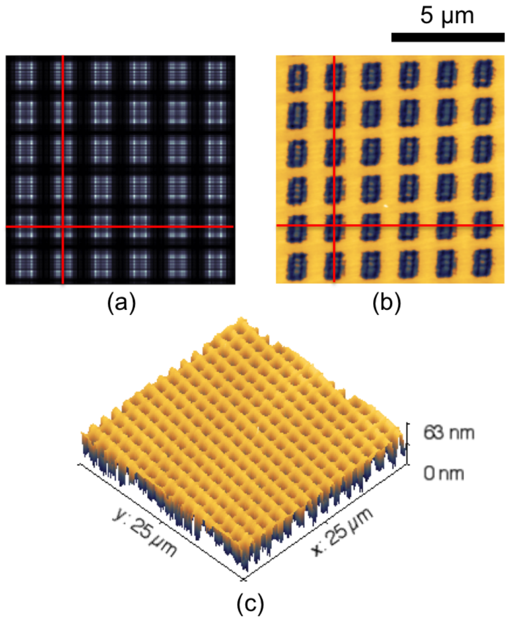

Fig. 5.2.6 (a) Simulated pattern image, (b-c) lithographic print of fractional Talbot pattern on the photoresist coated wafer for $M_{sf}^2 = 9$, (b) top-view, and (c) 3D-view.

The cross section profiles along red lines in Fig. 5.2.6 (a) and (b) are plotted in Fig. 5.2.7. The calculated intensity and measured profiles in PMMA are compared in vertical and horizontal cross sections. A direct comparison between the calculated intensity profile and the depth modulation of the developed resist shows a good agreement. The absence of fine structures in the lithographic print appearing in the calculated profile is caused by non-linearity of the photoresist's response [1993 Henke].

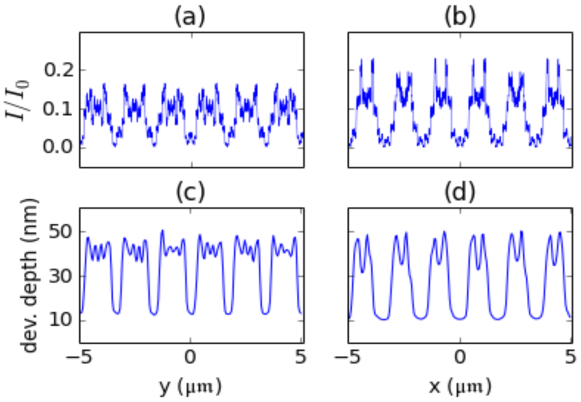

Fig. 5.2.7 (a) vertical and (b) horizontal cross-sections of the calculated intensity pattern shown in Fig. 5.2.6 (a). (c) Vertical and (d) horizontal cross-sections of the printed pattern shown in Fig. 5.2. 6 (b). In these plots, the zero depth corresponds to the top surface of the resist.

The error in the wafer positioning produces extra structures in the print. This effect is evident in Fig. 5.2.6 and Fig. 5.2.7. This inner diffraction fringe structure was observed because the z-position of the wafer deviated from the set position, $z = (1/3)\cdot(z_T/2)$ by "dz" due to the absolute wafer positioning error, see equation (6). Thus, in fact, the result in Fig. 5.2.5 is a fractional Talbot pattern recorded at $z = (1/3)\cdot(z_T/2) + 3$ μm. Even though the small details arise in the pattern, however, if dz < DOF, this fringing can be practically ignored because the further processing to the sample (e.g. etching) can effectively eliminate these fine structures below the threshold intensity.

Out-of-DOF fractional Talbot patterns

In the previous section, the fractional Talbot pattern achieving $M_{sf}^2 = 9$ is described when dz is located within the DOF. In this section, we discuss the situation when the pattern is recorded outside of the DOF. Fig. 5.2.8 shows the calculated patterns located at z-range between $z_{(Msf=3)}$ and $z_{(Msf=4)}$. Fig. 5.2.8 (a) and (d) are the patterns when $z = z_{(Msf=3)} - 1$ μm and $z = z_{(Msf=4)} - 1$ μm respectively. Fresnel diffraction patterns are formed also in each square of the fractional Talbot pattern. Fig. 5.2.8 (b) and (c) are images at $z = z_{(Msf=3)} - 15$ μm and $z = z_{(Msf=3)} - 25$ μm that are locations between 5.2.8 (a) and (d). As shown in the figure, there is an intensity modulation between the squares. A clear multiplied pattern can be seen when dz < DOF as shown in the Fig. 5.2.8 (a) and (d), while the fractional pattern has been distorted when dz > DOF.

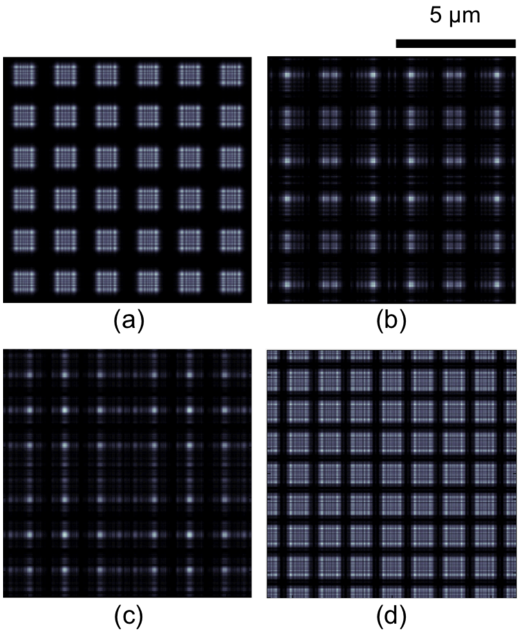

Fig. 5.2.8 Simulated intensity profiles at several z-positions near $z_{(Msf=3)}$ showing the pattern change as z moves from $z_{(Msf=3)}$ to $z_{(Msf=4)}$. (a) $z = z_{(Msf=3)} - 1$ μm, (b) $z = z_{(Msf=3)} - 15$ μm, (c) $z = z_{(Msf=3)} - 25$ μm and (d) $z = z_{(Msf=4)} - 1$ μm

Now we present the experimental results confirming these calculations in the case that dz is out of range of DOF of $M_{sf}^2 = 9$ such as Fig. 5.2.8 (c) using the mask in Fig. 5.2.5. Fig. 5.2.9 marks the z distance from the mask. It shows the fractional Talbot positions with ticks at $1/4\cdot(z_T/2)$, $1/3\cdot(z_T/2)$ and $1/2\cdot(z_T/2)$ and the corresponding DOF (17.6 μm, 33.2 μm, 88.8 μm as respectively) with blue shadings. The two red arrows are the z positions used in the experimental demonstrations.

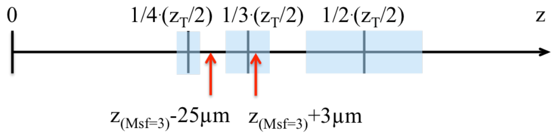

Fig. 5.2.9 z-axis showing z-positions (black ticks) and the DOF (blue shading) of several M_{sf}, and (red arrows) the z-positions of experimental samples at $z = z_{(Msf=3)} + 3$ μm (see Fig. 5.2.6 a), $z = z_{(Msf=3)} - 25$ μm (Fig. 5.2.8 c)

When dz = - 25 μm ($z = 1/3\cdot(z_T/2) - 25$ μm), which is out of DOF for $z_{(Msf=3)}$, (left red arrow in Fig. 5.2.9), the result shows the intermediate intensities between the squares, which is different from pattern recorded at dz < DOF as shown in Fig. 5.2.10. The calculated image of (a), experimental data with top-view (b) and 3D-view (c) are shown in Fig. 5.2.10. The simulated image in Fig. 5.2.10 (a) shows a good agreement with experimental result in Fig. 5.2.10 (b). Comparing both experimental results in Fig. 5.2.6 and Fig. 5.2.10, interference fringes appeared inside the array in case of dz < DOF, and the fringes appeared outside of the array in case of dz > DOF, while a clear spatial frequency multiplied (period demagnified) array pattern is achieved at the exact position of dz = 0 from $z_{(Msf)}$.

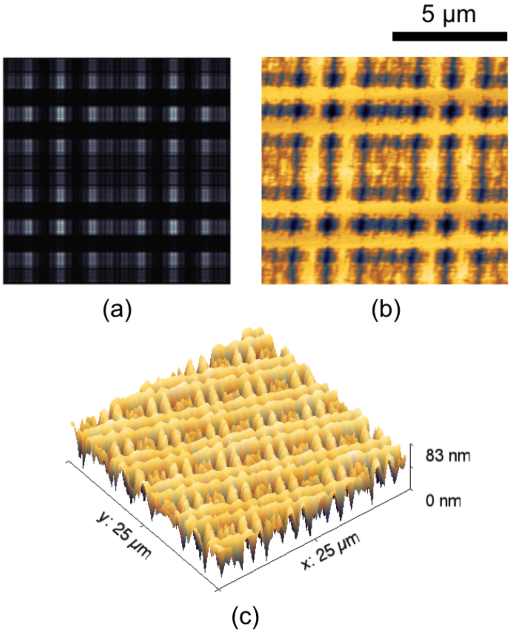

Fig. 5.2.10 The sample recorded at $z = z_{(Msf=3)} - 25\ \mu m$, which is out of DOF of $M_{sf} = 3$ in (a) simulation and lithographic result in (b) top-view and (c) 3D-view

5.2.5 DISCUSSION

The experiment demonstrates that making fine-structure patterns using the fractional Talbot technique is feasible. The quality of the patterns relies on precise positioning control of the wafer (within a DOF for a particular M_{sf}) as well as on the high contrast of the Talbot mask and requires the use of highly coherent EUV radiation. The positioning constraints include tilting and distance control between the mask and the wafer. Choosing the appropriate z-position of the wafer is important to achieve the desired multiplication factor. This position has to be controlled within the DOF. The tilting error may lead to a change of z-position across the wafer, and therefore induces pattern irregularities.

Fractional Talbot lithography allows variation of the structures density at the wafer using a single mask by changing the mask-wafer distance. This method shows also a path to reduce the structure size by using of spatial frequency multiplication utilizing shorter EUV wavelengths. The resolution limit of this technique will be studied by simulations and in experiments in chapter 7.

5.2.6 CONCLUSION

We have investigated fractional Talbot images for a 2D square array under coherent EUV illumination generated with a capillary discharge Ne-like Argon laser. The fractional patterns with spatial frequency multiplication up to $M_{sf}^2 = 9$ with corresponding half pitch of 0.85 μm × 0.85 μm were obtained in the experiment. The depth of field for the corresponding Talbot planes has been investigated in detail. The images within and outside of the DOF have been simulated and recorded in experiments. For the investigated arrays Fresnel fringes were observed within the rectangles in the first case ($dz < DOF$), while in the latter ($dz > DOF$) interference fringes occur between the rectangles. A precise control of the position and the tilt of both mask and wafer are therefore essential for the implementation of the method in the Talbot lithography. In addition to that, a high-contrast Talbot mask and coherent EUV radiation are required as well. Fractional Talbot lithography has potential application in manufacturing of periodic structures such as photonic crystal arrays, nano antennae, quantum-dot arrays, etc. This technique is convenient for the patterning of large areas at high resolution and for variation of the structures density using a single parent mask. We envision achieving higher multiplication factors for 2D arrays and also array pattern manipulation by shape variation in the near future. Additionally, the method would benefit from the utilization of shorter wavelength coherent sources in the vicinity to 10 nm, like the EUV laser systems described in [2010 Alessi].

5.3 RESTORATIVE SELF-IMAGING OF ROUGH LINE GRID

Restorative self-image of rough line grids: application to coherent EUV Talbot lithography

Self-imaging is a well-known optical phenomenon produced by diffraction of a coherent beam in a periodic structure. The self-imaging effect (or Talbot effect) replicates the field intensity at a periodic mask in certain planes effectively producing in those planes an image of the mask. However, the effect has not been analyzed for a rough-line grid from the point of view of the fidelity of the image. In this section, we investigate the restorative effect of the self-image applied to the lithography of gratings with rough lines. The study is applied to characterize a Talbot lithography experiment implemented in the extreme ultraviolet. With the self-imaging technique, a mask with grid patterns having bumps randomly placed along the line edges reproduces a grid pattern with smoothed line edges. Simulation explores the approach further for the cases of sub 100 nm pitch grids.

5.3.1 INTRODUCTION

The quality of patterned structures is important, because it influences the functionality of the device. The fidelity of the printed pattern is particularly critical in the fabrication of micro-electronics components. The microelectronic industry had invested significant amount of efforts and resources to mitigate this problem, localizing and repairing defects in the lithography masks. But also in other applications besides the main stream of the micro-components industry, the quality of the lithography print is instrumental to successful device fabrication and performance.

Talbot lithography is particularly well adapted to produce high quality lithography prints with high resolution over large areas. It has been shown that the Talbot effect can reproduce defect free images from a defective periodic mask. This filtering characteristic was identified as a convenient way to improve the quality of the print in a lithography process [1971 Dammann, 1990 Lohmann]. The defect tolerance characteristic of the Talbot images is well studied in the bibliography. It was shown that a mask with a periodic pattern, which is locally damaged, produces a defect-free copy at the Talbot distance. The effect of a defect on the pattern size around the defect in ArF Talbot lithography was investigated for submicron patterns [2015 Sato]. In this case, the periodic mask included regularly distributed defects. On the other hand, it was shown how the presence of spherical particles behind gratings affects the formation of Talbot self-images [2012 Hofmann]. The tolerance in angles of continuously self-imaging gratings was studied for non-paraxial illumination both numerically and experimentally [2007 Druart]. Defect tolerant Talbot imaging was studied for lithography applications with an EUV laser in the case of masks with complex designs [2009 Isoyan, 2013 Li]. For the particular case of a line grating, it is increasingly difficult to fabricate a straight-line edge when the pitch is reduced. Thus it would be worthwhile to analyze the restoration effect of the Talbot image in this case, quantifying the quality of the replicated pattern for the rough-line grid.

In this chapter, we analyze with numerical simulations and experimental results the effectiveness of EUV Talbot lithography to improve the lithography print from rough line grid masks. For the test we used a binary transmission mask fabricated in an opaque membrane with slits opened through it and a coherent EUV high-photon flux laser. We observed improvement in the pattern recorded in the photoresist compared with the original pattern on the mask. We also performed a model calculation of the obtained image for sub-100 nm pitches and analyzed the limits of the improvement.

5.3.2 SIMULATED DEMONSTRATION

Fig. 5.3.1 illustrates the scheme of the self-imaging effect. When the mask (Fig. 5.3.1 a) is illuminated by a plane wave, a replica of the mask's pattern is observed at the Talbot plane z_T (Fig. 5.3.1 b). For the simulation, a line grid pattern with rough edges was created. Bumps of ~ 100 nm radius were randomly distributed along the line edges. The size of the bumps along the edges of the slits that produce the roughness was selected to be bigger than a cut-off size defined as $\Delta x \approx \lambda/2\pi \approx 7.5$ nm for the wavelength at 46.9 nm. This selection validates the results of the scalar theory used in the simulations. The distribution was performed using the random function in Matlab's built-in functions.

The diffraction pattern was calculated using the Fresnel diffraction formalism, by the fast Fourier transform method [1996 Goodman]. The scalar diffraction method assumes the mask is within the thin mask approximation (TMA). The simulation is performed as a finite grid of $\Delta x = 0.5$ nm, $\Delta y = 0.5$ nm, over field of 50 μm×50 μm of the mask.

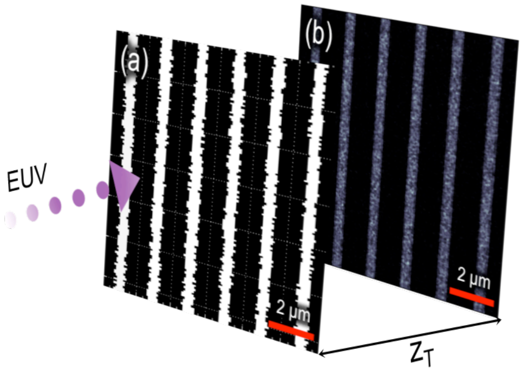

Fig. 5.3.1 Scheme of the self-imaging setup: (a) Talbot mask and (b) the self-image produced at a distance z_T

Fig. 5.3.2 shows the simulated images of (a) a mask with randomly rough lines, and (b) the self-image at z_T. The minimum dimension of the structures that can be imaged with sufficient accuracy is:

$$\Delta x \approx \frac{1}{k} = \frac{\lambda}{2\pi} \tag{5.3.1}$$

where the k is the wavenumber.

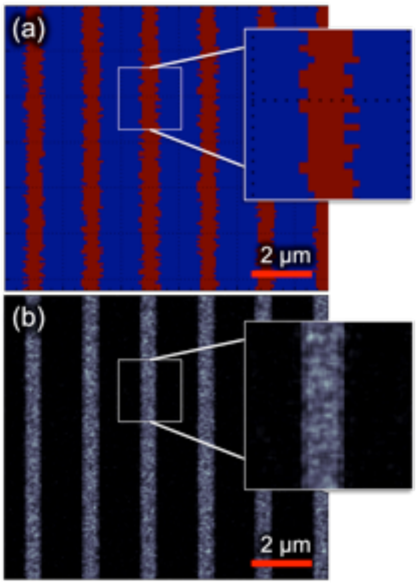

Fig. 5.3.2 Simulated images of (a) a mask with randomly rough lines, and (b) the self-image at z_T

The simulation shows that the self-image at z_T has significantly better quality, in which the bumps along edges are smoothed out over the grid. As a consequence, the rough lines were straightened in the self-image. The roughness along an edge was quantified using standard deviation (σ) defined as:

$$\sigma = \sqrt{\frac{1}{N} \cdot \sum_{i=1}^{N} (x_i - \overline{x})^2} \qquad (5.3.2)$$

where N is the number of samplings along a line, and the quantity in the bracket is the deviation of the edge of the slit from the straight line at the sampling point i. In the case of the self-image, the deviation of the edge is determined after a binary thresholding of the calculated image. Consequently, the deviation of the edge depends on the value selected for the threshold.

Fig. 5.3.3 shows the calculated σ for different threshold values ranging from 0.05 to 0.7. The calculated σ = 95 nm on the mask (Fig. 5.3.2 (a)) was reduced to σ ≅ 32 nm in the Talbot pattern (Fig. 5.3.2 (b)). In the analysis, the parabolic curve of σ in the Talbot pattern occurred due to the irregular intensity distribution of the areal image of Talbot pattern. When the threshold value is either too high or low, the difference of intensity value between neighboring x_i can be very large. This causes the higher σ values in the areal image as compared with the value obtained for the mask.

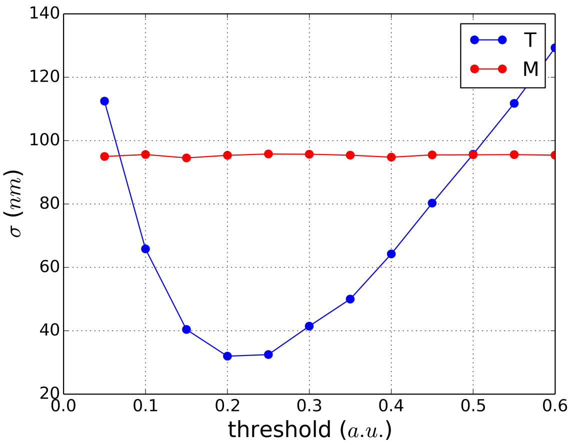

Fig. 5.3.3 The σ values on the self-image (T) in dependence of the threshold level, and on the mask (M) in simulation

5.3.3 EXPERIMENTAL DEMONSTRATION

The experimental demonstration was performed with an EUV laser and a transmission Talbot mask with a setup as following. The transmission mask and the wafer are aligned in the optical axis as illustrated in Fig. 5.3.1. Monochromatic EUV illumination of wavelength 46.9 nm was generated by a capillary discharge plasma laser [1999 Macchietto]. The capillary discharge plasma produces a highly spatial and temporal coherent beam well suited for the application described in this work. The spatial coherence length at the position where the self image was obtained was around 350 μm, which covered the whole area of the mask, assuring a fully spatially coherent illumination. The temporal coherence of the laser is $\Delta\lambda/\lambda \approx 3.5\times10^{-5}$. [2001 Liu, 1997 Marconi, 2012 Urbanski]. The exposure dose at the sample plane was about 0.1 - 0.3 mJ/cm^2 per pulse [2013 Li, 2014 Kim].

The transmission Talbot mask was defined using a focused ion beam (FIB) tool to drill through a low stressed Si_3N_4 membrane. The same binary file that was used for the simulation was fed into the FIB to make a more precise comparison between the calculation and the experimental results. After the milling, the mask was deposited with a layer of 50 nm of gold to improve the absorption in the EUV. The pitch in the mask was 2 μm, and the slit width was ~ 500 nm in average. The illumination field area of the mask was 50 μm × 50 μm. Fig. 4 shows the SEM image of the fabricated mask.

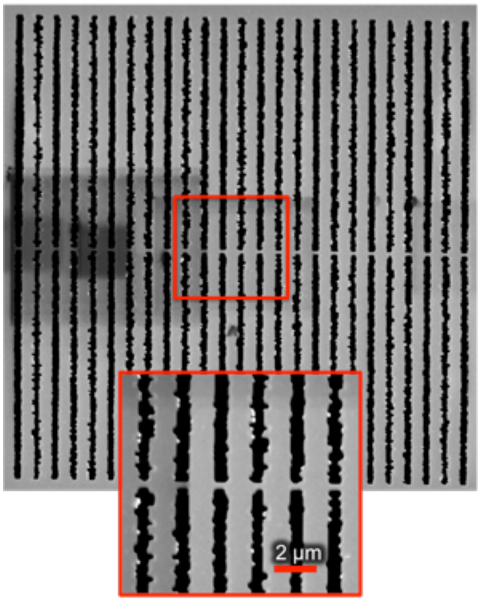

Fig. 5.3.4 The free standing transmission mask having the rough line grid

The depth of focus (DOF) in the Talbot plane is expressed as:

$$DOF = \frac{\lambda}{(NA)^2} = \lambda\left(1 + 4n^2\left(\frac{d^2}{\lambda \cdot A}\right)^2\right) \tag{5.3.3}$$

where A is mask field size [1999 Isoyan]. With the experimental parameters used the DOF is ~ 600 nm for the first Talbot plane, n=1.

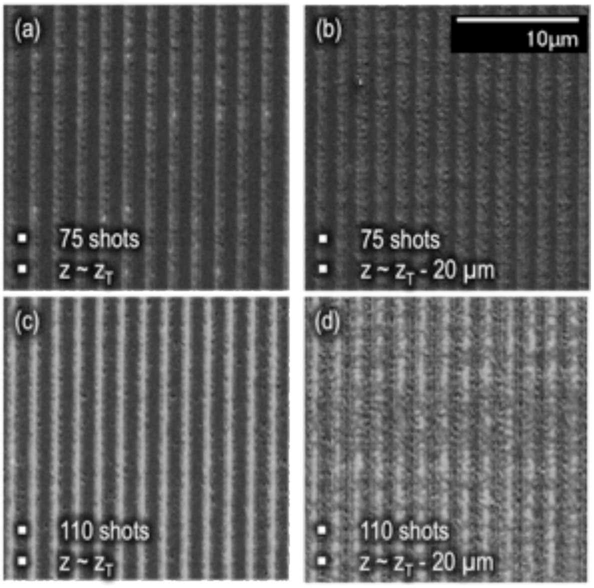

Fig. 5.3.5 Patterned photoresist images by self-imaging technique: The exposure dose and the distance cause the different qualities in the result.

The print was recorded on a silicon wafer spin-coated with 50 nm thick layer of photoresist (JSR Inc.). During the exposure, the distance from the wafer to mask was maintained close to the 1st Talbot distance. After the exposure, the exposed photoresist was developed for 30 seconds and rinsed with 2-Propanol. Fig. 5.3.6 shows SEM images of the patterned photoresist. The quality of the grid pattern is improved when the wafer is close to $z = z_T$ (a, c) rather than in the case when the wafer is out of focus (b, d). The quality improvement is significant when the distance is precisely controlled to be the Talbot distance. The quality also depends on the exposure time, because the threshold of intensity impacts the development results, as shown in Fig. 5.3.5 (a, c) and (b, d) that the photoresists were exposed with 75 shots and 110 shots respectively. Fig. 5.3.6 (a) is the zoomed-in image of Fig. 5.3.5 (c). Fig. 5.3.6 (b) is an AFM image taken at the central part of sample. The roughness is significantly decreased in the print as compared to the roughness in the mask.

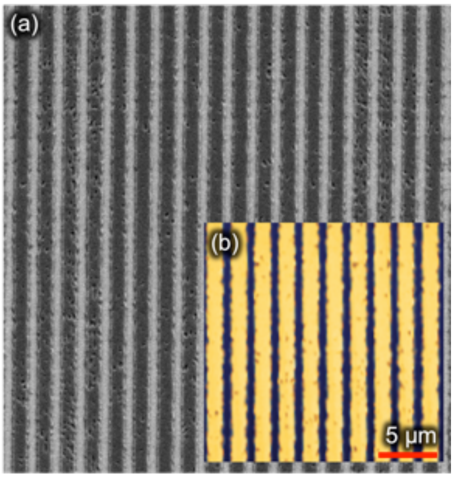

Fig. 5.3.6 the patterned photoresist measured with SEM and AFM (right bottom image)

5.3.4 RESULT AND DISCUSSION

In order to compare the roughness in the mask and the one in the self-image, the images shown in Fig. 5.3.4 and Fig. 5.3.6 (b) were converted into binary images as shown in Fig. 5.3.7. In this case, the gray-scale image turns into the binary image by the balanced histogram thresholding method (BHT). The pixels fall within a desired range of intensity values, thus the image is divided to black or white from two main classes: background and foreground [2008 Anjos].

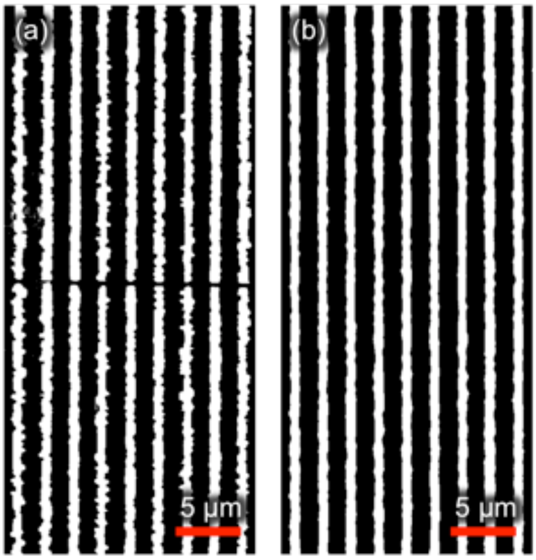

Fig. 5.3.7 (a) the mask image and (b) the self-image after the binary image conversion

The improvement of quality can be seen in Fig. 5.3.7 (a, b). This apparent improvement correlates well with the reduction of the σ. Fig. 5.3.8 plots the calculated σ for the mask and the Talbot image for 18 locations along the edges of the slits. The σ measured in the print are significantly lower than those in mask. The average values are σ = 88 nm in mask and σ = 46 nm in the print.

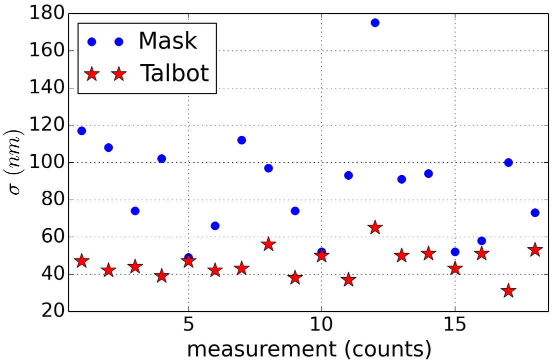

Fig. 5.3.8 σ values in the mask and Talbot patterns

The σ measured in the experimental result correlates well with the σ obtained in the simulation assuming a threshold for the binarization in the range 0.15 – 0.3 in Fig. 5.3.3. In both simulation and experiment, the σ values are reduced by about a factor of 2 or more.

Simulation for sub 100 nm pitches

We also analyzed the influence of the pitch, the slit width and the σ of the mask on the quality of the print. The study was completed by measuring the roughness of the Talbot image obtained with different masks.

First, to evaluate the influence of the pitch, we tested three different masks. The mask pitches were p = 100 nm, p = 60 nm, p = 30 nm. In those pitches, the roughness was σ = 6.2 nm, σ = 3.9 nm, and σ = 2 nm respectively. Due to the averaging characteristic of the Talbot effect, the σ in the self-image became σ > 3 nm, σ > 2 nm, and σ > 1 nm respectively. The σ in the mask (M) and at the Talbot plane (T) for selected pitches are plotted in Fig. 5.3.9.

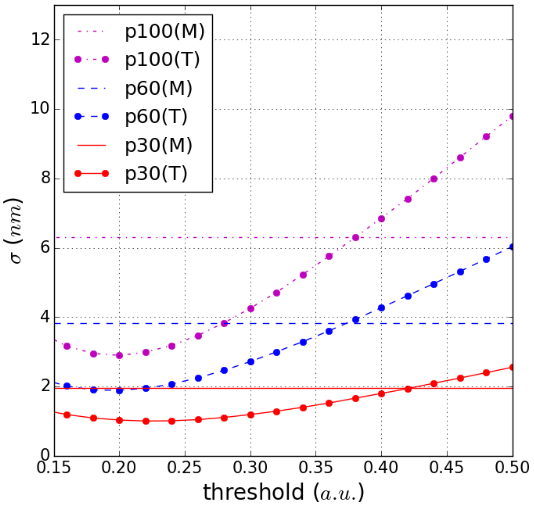

Fig. 5.3.9 The simulation result: σ curves in masks (M) and in self-images (T) for the pitches of 100 nm, 60 nm and 30 nm

The complete lithography method includes processes that determine the quality of the print. The printed result is influenced by the photoresist response and the development process among other factors. However, the analysis presented here with the thresholding method in the areal image is intended to study only the self-healing effect in the optical image. As discussed in Fig. 5.3.3, when we assume a threshold around 0.3 the simulation and the experimental results are in good agreement. Using this value for the threshold, the parameter σ in the self-image becomes 4 nm, 2.1 nm and 1.1 nm respectively. This represents a significant improvement of the self-imaging for sub-100 nm pitch gratings. The roughness is reduced by ~ 50 % for all three masks with different pitches and initial values of the sigma. Such amount of improvement is expected for all pitches considered in this analysis.

Second, we tested various mask pitches with identical σ. For this simulation, we used EUV illumination at 13.5 nm wavelength, which is a candidate for the source of the next generation of optical lithography. The pitches selected for this test were 100 nm, 60 nm and 40 nm, with σ in the three cases fixed at 3.2 nm in the mask. As shown in Fig. 5.3.10 (a), σ in the self-image is decreased from ~ 2 nm to ~ 1 nm as the pitch is increased from 40 nm to 100 nm. Our analysis indicates that the resulting sigma in the Talbot image is proportional to the ratio of the initial sigma and the slit-width (pitch/2) in the mask. So that in Fig. 10 (a), the sigma for the mask with a high-density grid is increased in comparison to the one for the mask with a low-density grid.

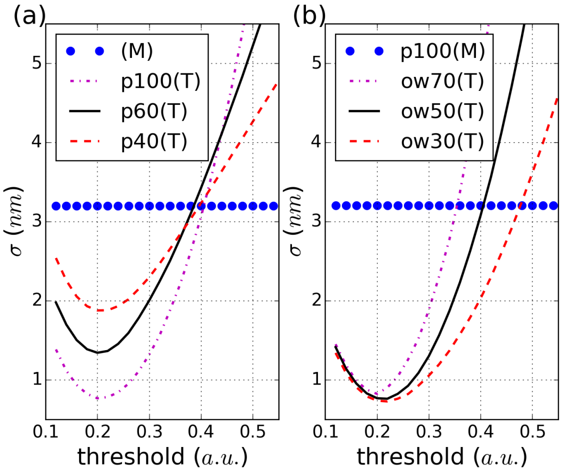

Fig. 5.3.10 The simulation results for various parameters: (a) σ at z_T (T) for pitches of 100 nm, 60 nm, and 40 nm when an identical σ (M) in mask is used, (b) σ at z_T (T) for opening widths of 100 nm, 70 nm, and 50 nm when a fixed 100 nm pitch and σ = 3.2 nm in mask is used.

Lastly, the slit-width was varied with fixed pitch and σ in the mask. The values of the slit-width were 70 nm, 50 nm, and 30 nm, with a fixed pitch of 100 nm and a fixed σ = 3.2 nm in the mask. As can be seen in Fig. 5.3.10 (b), the minimum σ values in the self-image were ~ 0.9 nm. However, the dependence on thresholding is different in the three cases enabling wider threshold values for smaller slit widths. For example, for σ = 2 nm, the threshold increases as the slit width or opening width (ow) is decreased as shown in Fig. 5.3.10 (b). This implies that the fabrication requirements can be relaxed with adjustment of the slit-width. Those results can be of a great interest in nano-patterning, where the line-edge roughness (LER) is one of the significant issues in electronic device fabrication.

5.3.5 CONCLUSION

In conclusion, we have demonstrated a submicron printing technique based on self-imaging and performed a detailed characterization of the quality improvement in the print relative to the mask. The rough grid pattern on the mask produces a self-image with line-edge roughness reduced by about a factor of 2 for 2 μm to 30 nm pitch gratings. This is due to the fact that line edges are randomly rough in the mask, which forms a smeared self-image that averages the roughness effectively reducing the σ. However, it also shows the limitation for improvement, because diffraction orders that are mainly influencing the self-image are limited to ±1st orders [2012 Kim]. In the simulation, the σ is improved in self-images for sub 30 nm pitch when EUV radiation is assumed in the illumination.

Chapter 6

Partial Coherent EUV Talbot Lithography

6.1 QUASI-MONOCHROMATIC TALBOT EFFECT

A useful source for the application of Talbot lithography includes EUV radiation generated by DPP offering the partial coherence optical property and sufficient intensity for photoresist exposure. The DPP of xenon (Xe) consists of strong emission in the spectral range between 10 nm – 16 nm corresponding to the ionization states between Xe^{11+} and Xe^{9+}. With the gas mixture with Argon (Ar), the spectrum becomes narrow at around 11 nm wavelength, moreover, the spectrum above around 12 nm can be reduced using Nb filter (~100 nm). Such a spectrum is shown in Fig. 6.1.1. The bandwidth at full-width half-maximum of the main peak around the wavelength at 10.88 nm is $\Delta\lambda/\lambda \approx 3\times10^{-2}$. This radiation could be useful for Talbot lithography with the quasi-monochromatic Talbot effect near the mask. No complex EUV mirrors are required to get a narrow spectrum.

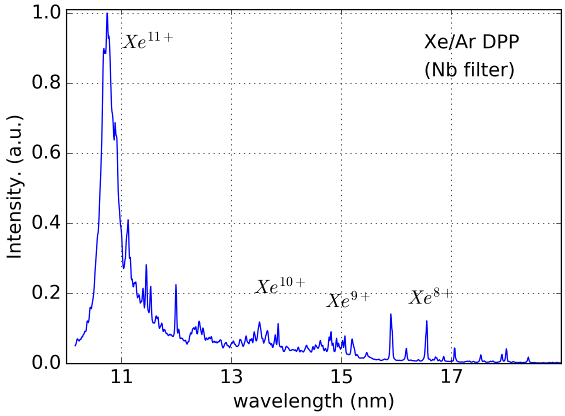

Fig. 6.1.1 EUV Spectrum emitted by DPP with Xe/Ar gas mixture

The gas DPP source is spatially incoherent due to the nature of the plasma emission and the finite source size from the pinching between the electrodes. The spatial coherence can be improved by increasing the distance between the pinch and the object, because the coherence length is related to the diameter of the source and the cone angle of the beam. The use of additional pinholes or slits will improve the coherence if the loss of intensity is allowed.

Talbot lithography with a DPP source can be efficiently performed when the source, the mask, and the arrangement with the photoresist are properly matched for the purpose. The finite size of the pinch causes a lateral shift δ of the interference pattern given by $\delta = g(d/D)$, see Fig. 6.1.2. Clearly, the distance between the source and mask (D), the gap between the mask and wafer (g) must be chosen so that the blur δ is small compared with the line-width of either the fractional Talbot fringe or achromatic Talbot fringe (see chapter 6.2) to appear clearly [1972 Spears].

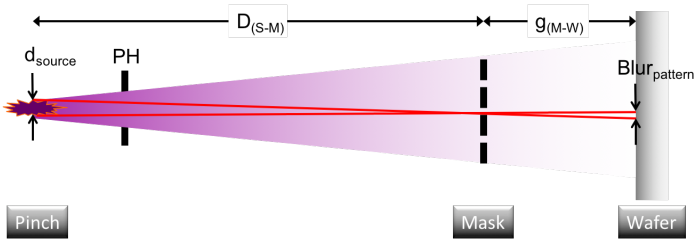

Fig. 6.1.2 The schematic of the Talbot lithography using quasi-monochromatic source. The lateral shift δ = g(d/D) occurred due to the finite size of the source d

The quasi-Talbot effect has been demonstrated for many applications. The optical Talbot effect with a broadband spectrum is utilized for spectral measurements [2003 Guerineau] and the temporal and spectral characterization of ultra-short laser pulses [2003 Teng]. The quasi-Talbot effect was investigated in the deep Fresnel diffraction region [2007 Teng]. The self-image has been successfully replicated and recorded at the effective Talbot distance using a broadband hard x-ray beam ($\Delta\lambda/\lambda \sim 1$) [2010 Kim].

The simulation of quasi-Talbot patterns can be performed with an incoherent sum over the broad spectral range. The fractional Talbot patterns in the field near the mask are analyzed in the range between the z=0 (mask) and the 1st Talbot distance. The test mask consists of a pitch of 2 μm and we observed the fractional Talbot pattern influenced as a function of the slit-width. Fig. 6.1.3 shows the Talbot images calculated by the scalar diffraction approach. The broad-band spectrum in Fig. 6.1.1 is used in the calculation. The interference fringes will be increasingly blurred as a function of the distance (g) until the number of the Talbot plane N approaches to $\lambda/\Delta\lambda$. Above the distance $N \cdot z_T$, an achromatic and propagation-in-variant intensity pattern is observed [2000 Guerineau]. In this demonstration, N is 33. In the deep Fresnel regime with low N, quasi-fractional Talbot patterning is possible.

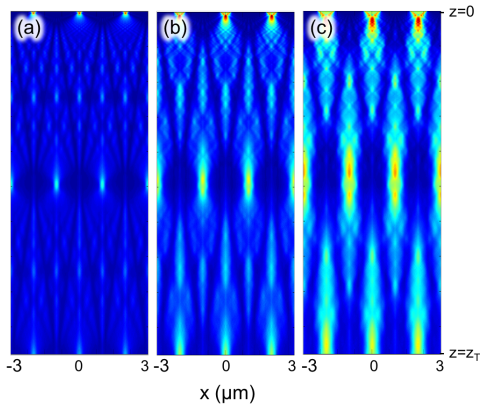

Fig. 6.1.3 Simulated Talbot images in the range between z=0 and z=z_T for different slit widths of (a) 250 nm, (b) 500 nm, and (c) 750 nm for same period of 2 μm

In experimental demonstration, the fractional Talbot patterns were printed on ZEP photoresist. The exposure time was only a few minutes with the DPP source operated with the discharge voltage of 5 kV, yielding the dose of around 20 mJ/cm^2 at the mask plane. The experimental masks are fabricated with the focused ion beam milling method. Gold with thickness of around 60 nm was deposited on a Si_3N_4 substrate with thickness of 50 nm. The sample was milled completely through both the absorber and substrate.

The photoresist sample was exposed at the distances in the range between z = 0 and the first Talbot distance, including the fractional Talbot planes for M_{sf} = 2, 3, and 4. Fig. 6.1.4 (a-c) shows SEM images of the masks having various slit-widths of 250 nm, 500 nm, and 750 nm respectively. Fig. 6.1.4 (d-f) shows the AFM images of the printed patterns on the photoresist, where the proximity gap was around between $z=(1/4)\cdot(z_T/2)$ and $z=(1/5)\cdot(z_T/2)$. The distance shift dz from the $z=(1/4)\cdot(z_T/2)$ was higher than the DOF of $M_{sf}=4$.

In order to obtain the fractional Talbot pattern, the following facts must be considered. The maximum M_{sf} is limited by the finite slit-width, and the depth of focus is increased as the slit-width is increased. With these conditions, the demonstration shows the printed patterns in Fig. 6.1.4 (d, e, f).

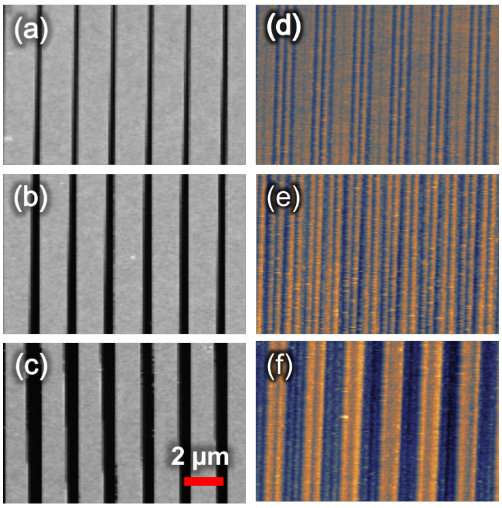

Fig. 6.1.4 Grating masks (2 μm pitch) with different slit widths (a: 250 nm, b: 500 nm and c: 750 nm) (SEM images), (b) AFM images of the lithographic samples showing fractional Talbot patterns

From our experimental results, the printed patterns at other distances from the contact to the several fractional Talbot distances are plotted in the Fig. 6.1.5 for the masks of difference slit-widths. The resist profiles for the masks of slit-widths of 250 nm, 500 nm, and 750 nm are plotted in (a), (b), and (c) respectively in Fig. 6.1.5. The mask with the slit-width of 250 nm results in the narrow slits on the prints. However, the DOF is relatively small compared to wide-slit-masks. With the mask with the slit-width of 750 nm, the demonstration results in the spatial frequency multiplication only up to M_{sf} =2 as expected.

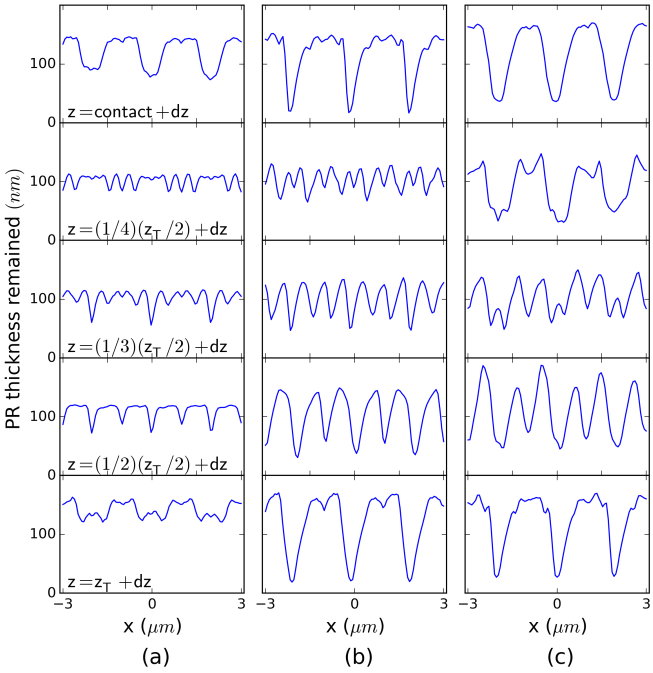

Fig. 6.1.5 The resist profiles exposed at different distances z for the masks of difference slit-widths: (a) 250 nm, (b) 500 nm, and (c) 750 nm

In conclusion, we demonstrated the fractional Talbot patterning with partially coherent EUV radiation generated by a DPP source with a Xe/Ar gas mixture. The fractional Talbot patterns are obtained between the contact and the first Talbot plane which is the quasi-monochromatic Talbot regime. The demonstration will be useful for applications of DPP sources where the quasi-monochromatic regime is required for purposes such as lithographic patterning, spectrometry, or optical characterization of incoherent sources.

6.2 ACHROMATIC TALBOT EFFECT

6.2.1 REVIEW OF THE ACHROMATIC TALBOT EFFECT

The self-image is basically a phenomenon of interference of the diffracted beams through the periodic mask coherently illuminated. Certainly this effect relies on the wave nature of light that is revealed by the diffraction and interference phenomena. The classical Talbot effect describes the longitudinal repetition of the grating self-images. The distance is approximated by $z_T = 2d^2/\lambda$, where λ is the wavelength of the monochromatic plane wave illumination. The Talbot pattern is repeated in the planes located at distances $z = n \cdot z_T$, where n is a positive integer.

When the illumination spectrally broadens, which means the radiation spectrum consists of the spectral lines of slightly shorter and longer than the central wavelength of spectrum, the Talbot distance is broadened as a sum of z_T of particular wavelengths. Then, the propagation of the intensity pattern becomes nearly propagation-invariant along the z-direction from a certain regime that is given by:

$$z_M = 2d^2/\Delta\lambda \tag{6.2.1}$$

where the Δλ is the temporal width of the spectrum. Such an effect is called the achromatic Talbot effect [2000 Guerineau, 2003 Guerineau]. In a monochromatic Talbot pattern, the images are formed not only at every plane at a distance $n \cdot z_T$ with positive integer n, but also at planes of $(n-1/2) \cdot z_T$, laterally shifted for the half of the period of the grating. In achromatic Talbot pattern both the pattern of grating and the shifted pattern of grating are formed at a single observation plane. Fig. 6.2.1 illustrates the Talbot pattern along the propagation direction behind a typical grating produced by monochromatic and by spectrally broadband radiation.

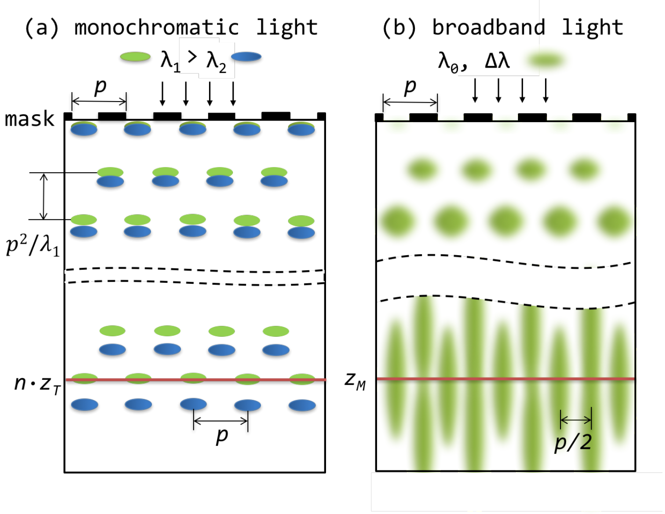

Fig. 6.2.1 Talbot self-imaging effect with monochromatic (left) and broadband (right) radiation

The achromatic Talbot image is an incoherent sum of field intensities of elementary monochromatic patterns resulting in two times smaller fringe period (p/2). Fig. 6.2.2 plots the simulated image of an achromatic Talbot pattern with partially coherent EUV radiation based on Xe DPP source. This Talbot image was calculated for a mask with a pitch of 30 nm for illumination with a central wavelength at λ=10.9 nm and bandwidth of Δλ/λ=0.03. The intensity profile along the propagation axis results in an interference pattern whose envelope encodes the Fourier transform of the spectral distribution of the light [2000 Guerineau]. The cross-sectional profiles along the propagation axis behind the absorber, slit, and the location between the absorber and slit are plotted in Fig. 6.2.3 as a max 1, max 2, and min respectively (also see Fig. 6.2.2). The min value is constant along the z-axis. The curves of max 1 and 2 are enveloped along the z-axis due to the Gaussian spectrum of the illumination light. The intensity is increased and decreased around a certain value as a function of the propagation distance [2003 Guerineau].

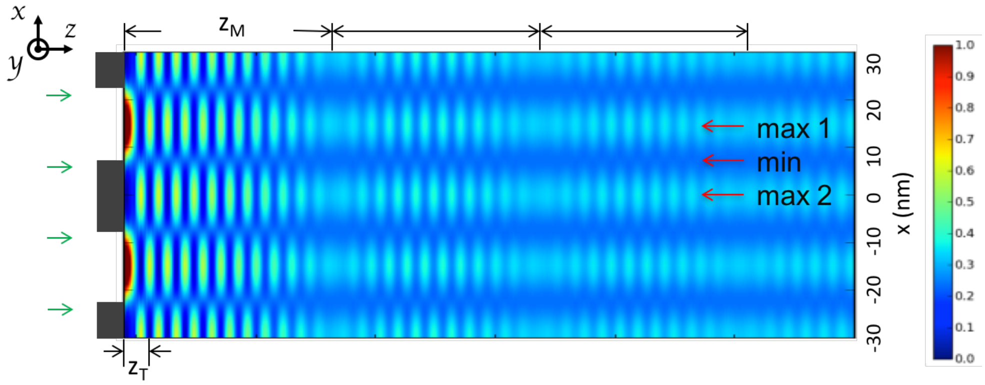

Fig. 6.2.2 The simulated achromatic Talbot pattern along propagation direction z

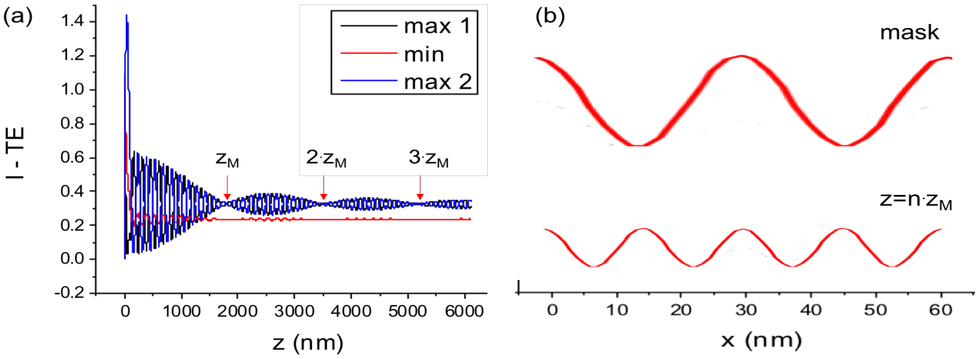

Fig. 6.2.3 (a) The cross-sectional profiles along the propagation direction z behind the particular position of absorber, slit, and the location between the absorber and the slit, in the plot, respectively max 1, max 2, and min (b) the cross-sectional profiles along the x-axis at z=0 (mask), and at $z=3z_M$ (achromatic Talbot distance)

The Talbot pattern at the first z_T is nearly equal to the monochromatic Talbot image. However, the image is smeared along the propagation direction due to the incoherent sum over the broadband spectral range. The mask period in transverse cross-section becomes a half at the plane of $n \cdot z_M$. The values of the two maximum intensities converge to a constant value as a function of the propagation distance as shown in Fig. 6.2.3 (a), the depth of field of the achromatic Talbot pattern is very large with high-number of n.

The achromatic Talbot effect leads to the lithographic applications of high-density patterning [2005 Solak, 2006 Solak]. In chapter 7.2, achromatic Talbot lithography will be discussed for obtaining sub 10 nm resolution.

Chapter 7

Resolution Limit of Talbot Patterning

7.1 OPTICAL LIMITS OF FRACTIONAL TALBOT PATTERNING WITH EUV RADIATION

Optimizing optical properties of gratings at a certain illumination wavelength is crucial to achieve a large number of fractions and high density patterns in fractional Talbot patterning. In this work, we study the optical limits of fractional Talbot patterning with coherent extreme ultraviolet (EUV) illumination using the rigorous optical wave propagation simulation. Analysis of the Talbot pattern by varying grating parameters is performed in order to evaluate their influence on intensity and contrast of the interference fringes. We observe images with high-density fringes of high quality, resulting in 11 nm half-pitch patterns.

7.1.1 INTRODUCTION

EUV interference lithography has attracted attention to fabricate periodic structures with high resolution and to study the fundamental optical properties of EUV-matter interaction. Dual grating EUV interference lithography [2015 Mojarad, 2015 Karim] and single grating EUV achromatic Talbot lithography [2005 Solak, 2013 Danylyuk, 2016 Brose] have been demonstrated to achieve high resolution structures in photoresists. Both techniques utilize transmission gratings that serve as a mask, consist of high-resolution structures and contribute mainly to the intensity profile that is created in wafer plane. An increase of the spatial frequency up to two times can be achieved by the utilization of these different interference schemes.

To achieve a greater demagnification of the mask pitch (period), the fractional Talbot effect can be utilized. It is capable of obtaining regular intensity profiles of high-density [1979 Flanders]. This technique requires a very careful control of mask-wafer distance due to its low depth of field, but it is possible to use the technique to achieve an alternative periodic structuring with high resolution and more relaxed mask requirements [2014 Kim]. The reduction of the grating pitch by self-imaging of high-order Talbot fringes has been spatially resolved [1997 Nowak, 2016 Kim]. Also in this approach the master grating's pitch and its slit-width/pitch ratio is mainly contributing to the intensity profile and determines its capability to achieve highly dense fringes with a large number of spatial frequency modulations.

The optical properties of the transmission grating at a certain illumination wavelength need to be optimized to achieve a large number of fractions, especially in a non-paraxial regime under EUV illumination. The conventional Talbot effect is not valid in this regime. The electromagnetic theory of Talbot imaging of wave fields diffracted by metallic and dielectric gratings has been investigated [1993 Noponen]. It was shown that the interplay of high-diffraction orders impacts the formation of the Talbot image of wavelength-scale amplitude gratings [2012 Kim, 2012 Hua, 2012 Sato]. In the paraxial regime, the important parameter of the Talbot mask includes the mask pitch and its slit-width/pitch ratio. Large numbers of pitch reduction can be obtained with small slit-width/pitch ratios. As the slit-width becomes narrower, illumination at short wavelengths is required to avoid both the extinction behind each single slit and the transmission of the absorber. The absorber thickness is limited by the fabrication process of the mask. Creating masks with high aspect ratios is challenging, therefore smaller feature sizes necessitate a thickness reduction of the absorber leading to a reduced mask contrast.

In the non-paraxial regime, the Talbot image has to be obtained with non-paraxial rigorous calculation. The refractive index and the thickness of the absorber have to be chosen carefully to obtain a high-resolution Talbot image with high intensity and contrast. In an experiment, the photoresist as a recording medium needs to be capable of visualizing the provided intensity profiles. The minimum feature size in the exposure result will be limited by the photoresists resolution and the resist contrast sets the lower limit for the acceptable contrast of the intensity profile that leads to a successful resist pattern [1985 Wake].

We study the optical limits of fractional Talbot patterning under EUV illumination with a rigorous optical wave propagation simulation. Only masks that can be practically fabricated are considered. Analysis of Talbot patterns with various mask parameters is performed for EUV illumination that is transverse electric (TE) polarized, monochromatic and spatially coherent.

7.1.2 THEORETICAL REVIEW ON FRACTIONAL TALBOT EFFECT

In the near-field behind a transmission grating illuminated by a plane wave, self-images can be observed at defined distances behind the mask as discussed in Ch. 5. The minimum feature size of the print depends on the spatial and temporal coherence of the incident radiation and its polarization. However, this work focuses on linear polarized coherent radiation that illuminates several mask features to observe the diffractive nature of the fractional Talbot images.

In the paraxial regime, the fractional Talbot image, which is the Fresnel image of the opaque mask, is not significantly influenced by the complex refractive index and thickness of the absorber. However, sharp fractional Talbot images are not expected to be resolved unless $d/\lambda \gg 1$ [1993 Noponen]. Moreover, in the EUV spectral range, the refractive index n is close to unity for most materials, e.g., n of gold = 0.9. The attenuation of the supporting membrane and the absorbers is not significantly different, not as for a classical Talbot mask, e.g., $\kappa_{Si3N4}/\kappa_{Gold}$ = -0.0093/-0.051 with EUV radiation of wavelength at 13.5 nm, where $n = n+i\kappa$ and κ is the extinction coefficient. When increasing the absorber thickness to increase absorption, the intensity becomes too low to expose photoresists in lithographic techniques.

Therefore, creating high contrast between membrane and absorber and identifying the optimal feature size, period, slit-width/pitch ratio and absorber thickness are very important in order to obtain high-density fractional Talbot fringes of high intensity and contrast [1997 Nowak, 2004 Mambro].

7.1.3 METHOD OF SIMULATION

In order to obtain a large number of interference fringes and therewith intensity modulation of high spatial frequency, we force the mask feature size to approach the wavelength scale. For this purpose, we employ a diffraction analysis using the finite-difference time-domain (FDTD) method for a rigorous electromagnetic field (EMF) simulation with the simulation tool DrLiTHO [Web DrLiTHO, 2011 Erdmann]. This method computes the transmitted electric field distribution in the near field. Lateral dimensions (x, z) are specified on the grid with scale of $\lambda/10$. This simulation method is used to explore the impact of mask geometry and its material properties in the EUV range on the fractional Talbot patterning.

Modelling of Talbot masks

In this chapter, we utilize two different types of amplitude grating masks. We consider Si_3N_4 membrane supported masks with absorber structures on top and complete free-standing masks consisting just of absorber lines that are not supported by a Si_3N_4 layer. Our typical transmission masks consist of high-transmissive membrane materials and a highly attenuating absorber [2012 Brose].

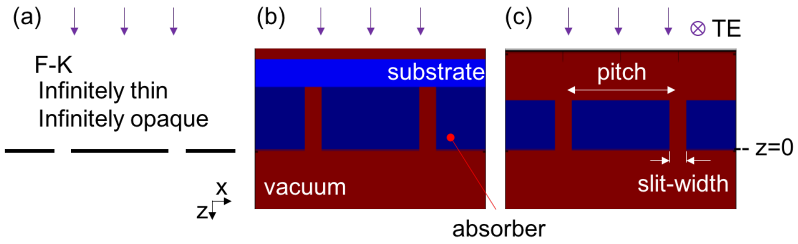

Fig. 7.1.1 The different schemes of fractional Talbot masks: (a) F-K mask, (b) membrane supported mask, (c) free-standing mask without membrane support

Fig. 7.1.1 illustrates possible mask geometries for fractional Talbot lithography under coherent EUV illumination. Whereas in the Fresnel-Kirchhoff approach, the mask is infinitely thin and completely opaque, as shown in Fig. 7.1.1 (a), the non-paraxial Talbot mask utilizes a complete two-dimensional (x, z) layout of the mask, consisting of membrane and absorber layer in case of a membrane supported mask, as in Fig. 7.1.1 (b), or a free-standing mask without membrane support, as in Fig. 7.1.1 (c). This simulation uses TE polarized coherent plane illumination.

7.1.4 RESULTS AND DISCUSSIONS

Talbot images depending on the mask layout and composition

The rigorously simulated Talbot images with different schemes of masks differ from each other in evanescent field intensity, contrast and regularity of fringes, especially for a high number M_{sf} fractional Talbot pattern.

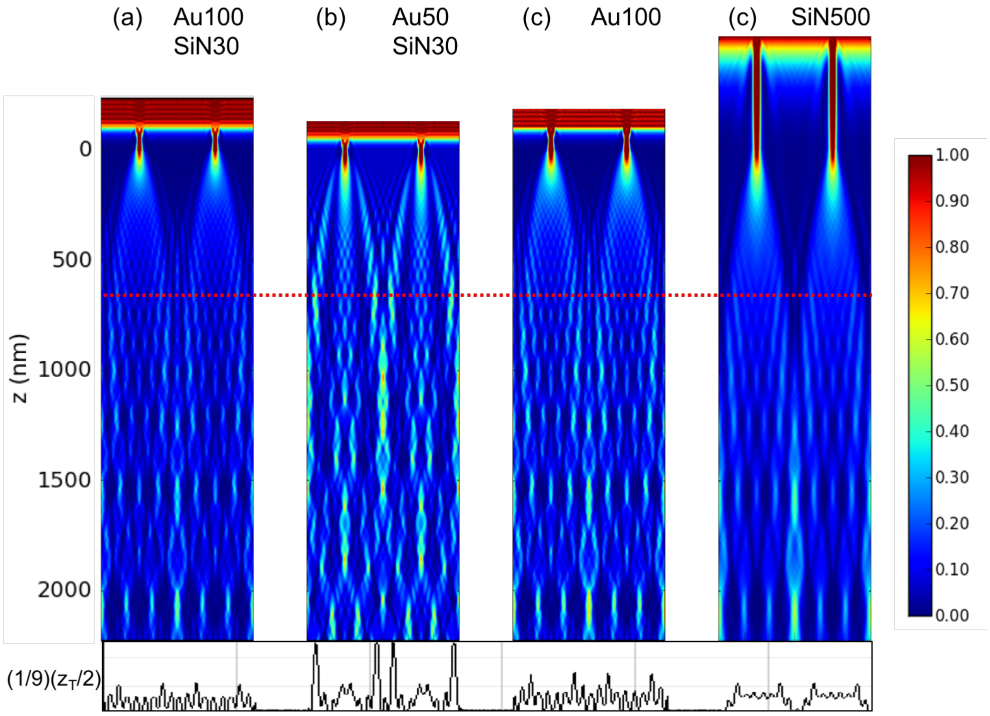

Fig. 7.1.2 Talbot images as a function of a distance for different mask layouts: The common parameters include the illumination of wavelength of 13.5 nm, mask pitch of 300 nm and the slit-width of 30 nm. (The intensity profiles at the bottom are cross-sections at $z_{(Msf=9)}$ resulting in print pitch of 33 nm)

Fig. 7.1.2 shows the Talbot image along propagation direction z in the range from mask z=0 to $z=(1/3)\cdot(z_T/2)$. The common features in the masks are the pitch of 300 nm and the slit-width of 30 nm. In Fig. 7.1.2 (a-b), two different gold absorber thicknesses of 100 nm and 50 nm are used both on top of a Si_3N_4 membrane with 30 nm thickness. In Fig. 7.1.2 (c-d), the free-standing mask features are deployed in a gold layer (100 nm thickness) and as a second type of free-standing mask in a Si_3N_4 layer (500 nm thickness). Overall the intensity patterns look quite similar but there are some quite important differences when looking at the details. The intensity profiles at $z = (1/9)\cdot(z_T/2)$ (horizontal red line) are compared at the bottom of Fig. 7.1.2. In case of (a) and (c), the regularity of the intensity modulation is relatively fine in comparison to the case of (b) and (d) where the $M_{sf} = 9$ is hard to distinguish and might be not possible to realize in the experiment.

Spatial frequency multiplication of fractional Talbot pattern

This section shows that the high number of M_{sf} can be obtained when using a low ratio of slit-width to pitch. However, it is limited by the evanescent field when the slit-width is too small in the non-paraxial regime. The test mask to observe the limit of M_{sf} consists of a pitch of 500 nm and a slit-width of 20 nm. The gold absorber has a thickness of 200 nm on top of Si_3N_4 membrane of 30 nm thickness. The illumination wavelength is 13.5 nm (monochromatic, spatially coherent, TE-polarized). The propagation image of the Talbot pattern shows fine features of fractional Talbot fringes with M_{sf} as a function of distance, as plotted in Fig. 7.1.3. Fractional Talbot fringes of more than M_{sf} = 25 are observed in the simulation result. However, the overall regularity of the fringes in the cross-section profile is decreased as the M_{sf} increases. The cross-sectional profiles at several M_{sf} are plotted in Fig. 7.1.4 (a-e). The maximum fractional Talbot image is limited at M_{sf} = 22, with the corresponding pitch of 22.7 nm (half-pitch ~ 11 nm), as shown in Fig. 7.1.4 (c). For the experimental realization the intensity profiles on Fig. 7.1.4 (a) and Fig. 7.1.4 (b) might lead to a successful high-resolution resist pattern. In the case of Fig. 7.1.4 (c-e) there is an additional overall modulation of the Talbot fringes that will distort the resist pattern, leading to missing or overexposed regions in the exposure result. This distortion is increased as the spatial frequency multiplication is increased.

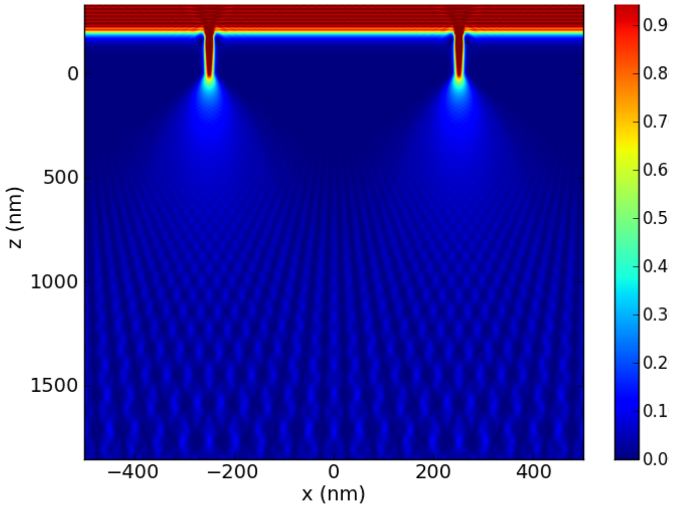

Fig. 7.1.3 The Talbot pattern along the propagation-axis z behind the mask consisting of the pitch of 500 nm and the slit-width of 20 nm

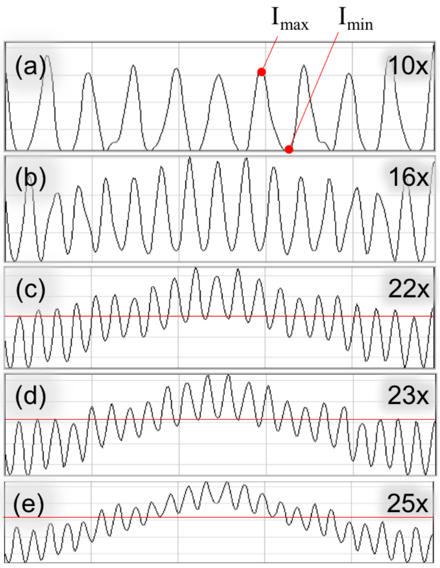

Fig. 7.1.4 The fractional Talbot patterns produced by the mask consisting of following parameters: pitch of 500 nm, slit-width of 20 nm, Si_3N_4 thickness of 30 nm, gold thickness of 200 nm, the Talbot pattern of M_{sf} (a) $M_{sf} = 10$ (b) $M_{sf} = 16$ (c) $M_{sf} = 22$ (d) $M_{sf} = 23$ (e) $M_{sf} = 25$

Fig. 7.1.5 plots the intensity and contrast for the particular profiles of Fig. 7.1.4. The intensity is average intensity of I_{max}. The contrast was calculated from the average values of I_{max} and I_{min}, where contrast is given by $C=(I_{max}-I_{min})/(I_{max}+I_{min})$. We analyzed the regularity of the fringes with variation of I_{max}, as plotted in the figure as an error bar. A long error bar implies a large irregularity and therewith indicates a large overall modulation in the Talbot pattern. The intensity is decreased as M_{sf} is increased, as expected. The contrast also decreases as M_{sf} increases, but at $M_{sf} = 22$, it is still more than 0.55, which is sufficient for the lithographic method.

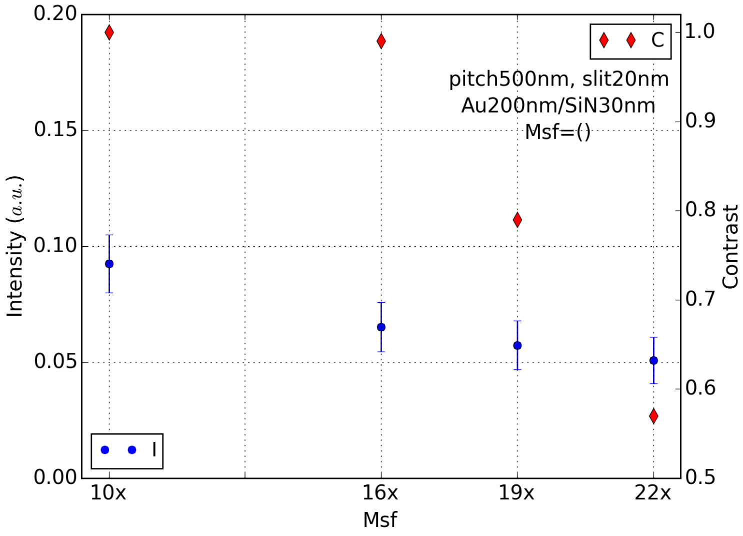

Fig. 7.1.5 Intensity (I) and contrast (C) in the fractional Talbot pattern as a function of M_{sf}

Pitch, slit-width, and thickness dependency

We also investigate the fractional Talbot pattern for various pitches, slit-widths and absorber thicknesses and their influence on intensity and contrast.

First, we tested masks with various pitches of 100 nm, 300 nm and 500 nm with fixed features of gold absorber of 200 nm thickness on a Si_3N_4 membrane of 30 nm thickness and a slit-width of 20 nm. The analyzed plane is at a distance $z_{(Msf=4)}$. Thus, the corresponding print pitches are 25 nm, 75 nm and 125 nm, respectively. The intensity for the pitch of 100 nm is greater than for the other pitches, but the regularity is lower than for the masks of other pitches. The contrast is greater than 0.6 in all cases.

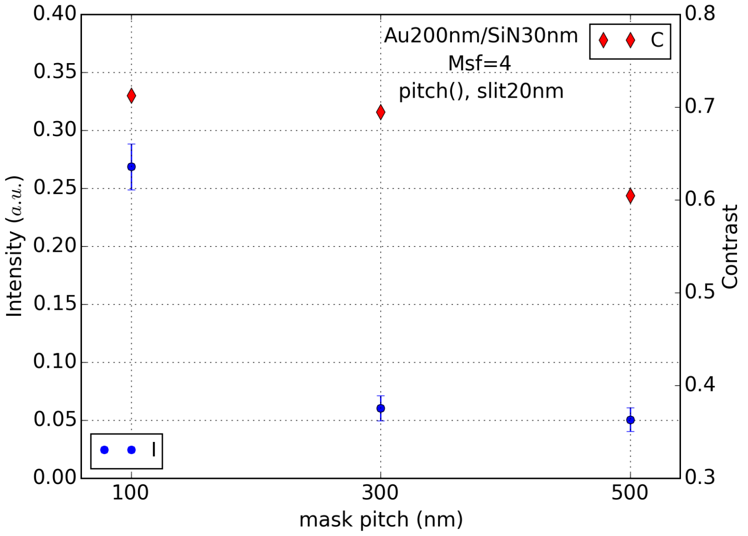

Fig. 7.1.6 Intensity (I) and contrast (C) of fractional Talbot pattern at a distance of $z_{(Msf=4)}$ as a function of pitch[###]

Secondly, various slit-widths from 10 nm to 25 nm are analyzed with the mask consisting of the common features of gold (thickness = 200 nm), Si_3N_4 thickness of 30 nm and a pitch of 100 nm. The analyzed image plane was at $z_{(Msf=4)}$, which results in a pitch of 25 nm in all cases. In this case, the influence of the evanescent field is significant in the results, especially when the slit-width becomes narrower. For the mask of 10 nm slit-width, the intensity is significantly reduced, but the contrast is very high. There is a tendency of increasing intensity as the slit-width widens. Interestingly, the irregularity is higher with a

---

[###] The increase of intensity with the decrease of mask pitch is occurred due to the fact that the overall slit area is increased as the pattern density is increased. The decrease of contrast with the increase of mask pitch is connected to the fact that I_{max} is decreased.

slit-width of 20 nm than with any other layouts of the mask. Therefore, the slit-widths of 15 nm and 25 nm are good candidates with respect to the three aspects of intensity, contrast and regularity. Since the intensity can be compensated by just longer exposure times the slit-width of 15 nm with a contrast of almost 90% seems to be a good option when fabricating a transmission mask.

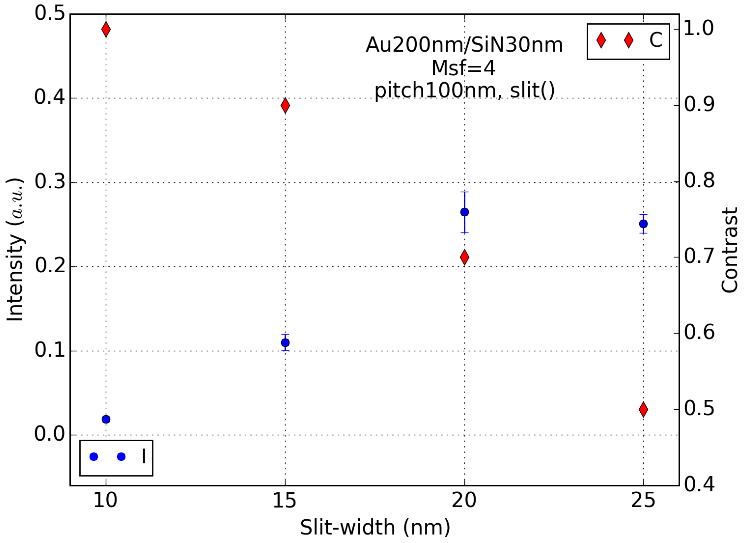

Fig. 7.1.7 Intensity (I) and contrast (C) in the fractional Talbot pattern dependent on slit-width

Third, we investigate the masks with various thicknesses of absorber with fixed parameters of pitch of 100 nm, slit-width of 20 nm, M_{sf} = 4, and Si_3N_4 membrane thickness of 30 nm. As expected, the intensity decreases as the thickness increases as shown in Fig. 7.1.8. It can be explained with the fact that the thicker opening tunnel (slit) reduces more the intensity of transmitted light, resulting in the evanescent field in the Talbot pattern as a function of distance. The regularity is decreased when using thin mask below 70 nm due to the high transmission through the absorber. The weak field passing through the absorber interferes with the main diffractive field. Interestingly, the contrast is not significantly different as the thickness changes. Comparing thicknesses of 110 nm and 130 nm, the regularity and intensity are better for the thickness of 110 nm while the contrast is better for the thickness of 130 nm. The complicated behavior of contrast as a function of the thickness might be caused by additional factors such as optical wave-guiding effect in the structure of high aspect ratio between opening width and the thickness.

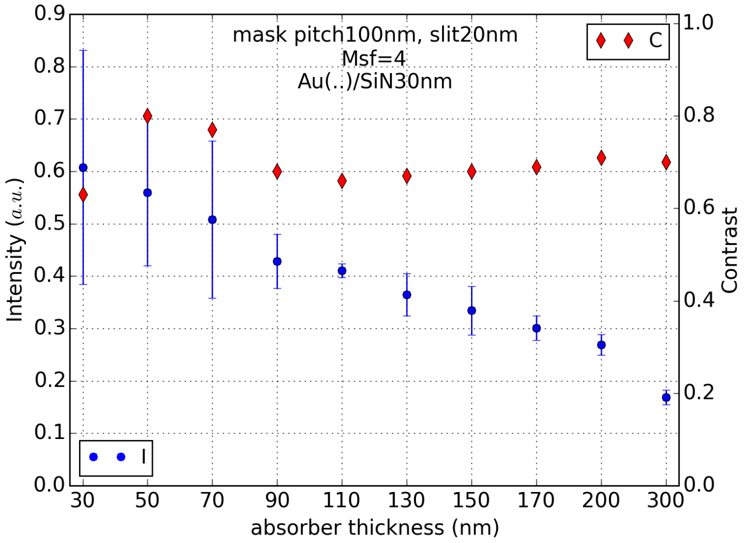

Fig. 7.1.8 The influence of absorber thickness on the intensity (I) and contrast (C) in the fractional Talbot pattern

A critical issue in fractional Talbot lithography is the short DOF. The photoresist layer on the wafer has to be located within the DOF. The DOF is determined from the cross-sectional profiles along the z-axis behind the slit (Fig. 7.1.9), the DOF for $M_{sf} = 4$ or $M_{sf} = 2$ is only 30 nm or 67 nm, respectively. Wafer positioning with less than 1 nm precision is required in this case. Also the resist thickness has to be taken into account to achieve a homogeneous height profile.

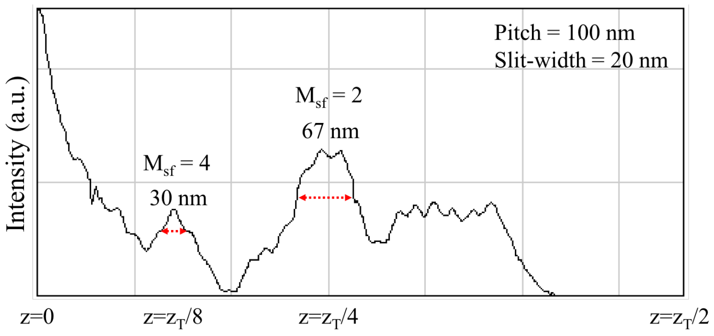

Fig. 7.1.9 The depth of field for the print pitch of 25 nm and pitch of 50 nm obtained for $M_{sf} = 4$ and $M_{sf} = 2$, respectively

Summarizing, there are tendencies of optical properties of the fractional Talbot pattern to depend on the mask layout geometry. The intensity decreases as slit-width decreases and the contrast decreases as the M_{sf} increases. However, some cases demonstrate extraordinary optical properties outside of this tendency. Therefore, a mask layout has to be optimized for specific purposes. Nevertheless, the tested layouts in this work suggest good examples of the mask designs in order to achieve high-density fringes in fractional Talbot lithography. The contrast of fractional Talbot patterns is approximately twice higher than that of achromatic Talbot patterns [2013 Danylyuk]. Fractional Talbot lithography can be a good alternative to achromatic Talbot lithography, but necessitates even higher degree of control over the proximity gap.

7.1.5 CONCLUSION

Fractional Talbot patterning is studied in a non-paraxial regime. The optical properties of the fractional Talbot image are found to be significantly influenced by the layout of the mask. We utilized a rigorous diffraction simulation to obtain the images with fine details to see the influences of different mask parameters. The dependencies of intensity, contrast and regularity are analyzed depending on pitch, slit-width and absorber thickness. Because EUV radiation interacts strongly with most materials, each particular mask layout has a different fractional Talbot image. However, we observe images with high-density fringes of high quality with this method, resulting in patterns with half-pitch of 11 nm. Future work includes how the contrast and the intensity of fractional Talbot images using phase shift masks can be improved.

7.2 ACHROMATIC TALBOT PATTERNS OF HIGH-RESOLUTION

Scalability limits of the Talbot lithography with plasma-based extreme-ultraviolet sources

Lithography has been faced with a challenge to bring the resolution down to the 10 nm level. One of the promising approaches for such ultra-high resolution printing is the self-imaging Talbot lithography with EUV radiation. However, as the size of structures on the mask approaches the wavelength of the radiation, diffraction influence needs to be evaluated precisely to estimate the achievable resolution and quality of the patterns. In this chapter, the results of FDTD simulations of the diffraction on EUV transmission masks in dependence on the period (pitch) of the mask are presented, with the aim to determine the resolution that can be realistically achieved with the EUV Talbot lithography. The modeled experimental setup is utilizing partially coherent EUV radiation with a wavelength of 10.9 nm from a Xe/Ar discharge plasma EUV source and a Ni/Nb-based amplitude transmission mask. The results demonstrate that the method can be used to produce patterns with resolution down to 7.5 nm half-pitch with 2:1 mask demagnification utilizing the achromatic Talbot effect and TE polarized light.

7.2.1 INTRODUCTION

Due to a limited availability of laboratory scale EUV sources and usually high coherence requirements for interference, the available setups for EUV-IL [2007 Ritucci, 2007 Wachulak, 2009 Auzelyte, 2009 Jiang, 2010 Fukushima] are mostly utilizing synchrotron radiation, which increases their operational costs and limits accessibility. During the last decade a number of interference schemes were investigated at these setups, including Lloyd mirror [2007 Wachulak, 2009 Parisse, 2010 Wachulak], single grating [2009 Auzelyte, 2010 Saib, 2010 Fukushima, 2011 Paivanranta, 2011 Urayama, 2012 Langner] and double grating

[2007 Naulleau, 2008 Shiotani, 2009 Smith] schemes. All of them have rather high requirements on spatial and/or temporal coherence, making them very inefficient for use with available high power laboratory sources.

One can, however, utilize Talbot self-imaging effect to produce an interference pattern with relatively low requirements on coherence, especially in the case of sub-50 nm half pitch structures [2005 Solak]. Moreover, it was shown that it is possible to de-magnify mask structures for up to a factor of 2 illuminating the mask with a broadband radiation [2006 Solak] without additional optical elements.

This approach allows one to minimize usually huge losses in the optical system and relaxes the requirement on the manufacturing resolution of the required transmission masks. The method was successfully demonstrated with synchrotron radiation [2006 Solak], and is a very promising candidate for high resolution printing of periodic arrays with laboratory sources.

However, the de-magnification of the method is limited to a factor of two and it is not clear whether this approach is scalable to sub-10 nm resolutions. As the size of structures on the mask approaches the wavelength of the radiation, the diffraction influence needs to be evaluated precisely to estimate the achievable resolution and quality of the patterns [1993 Noponen, 1999 Wolf].

In this chapter, the results of analytical and numerical analysis of the scalability of Talbot lithography with EUV radiation are presented with a focus on application of the method with partially coherent high power laboratory sources.

7.2.2 TALBOT SELF-IMAGING EFFECT AND ITS APPLICATION TO LITHOGRAPHY

Even though Talbot discovered his effect with polychromatic light, most of the experimental research was performed with monochromatic sources that allowed well defined Talbot patterns to be obtained. It was not until 2000 that it was theoretically and experimentally demonstrated [2000 Guerineau, 2003 Guerineau] that with the help of broadband illumination of spectral bandwidth $\Delta\lambda$, an achromatic and propagation-invariant pattern can be obtained.

The period of the resulting in-plane patterns for one dimensional gratings with rectangular and sinusoidal transmission profiles was found to be two times smaller than the period of the grating itself. However, the peak intensity of the patterns decreased to approximately a quarter of the incoming intensity. The resulting theoretical contrast of the patterns has decreased below 40% for both rectangular and sinusoidal transmission gratings.

First application of this method for EUV-IL was reported in 2005 [2005 Solak], where it was successfully applied to produce 50 nm half-pitch patterns from a 100 nm half pitch transmission mask using synchrotron radiation. The approach was later expanded to allow large area structuring [2012 Wang]. Elsewhere, the Talbot effect was also applied to structuring of high resolution patterns of complex geometry [2009 Isoyan, 2011 Urbanski].

The linear scaling of the minimal required spatial coherence length with the period of structures on the mask opens a window of opportunity for plasma based partially coherent EUV sources. Their practically achievable spatial coherence values in the range of several to several tens of micrometers, which satisfies the requirements for Talbot structuring of patterns with sub-200 nm periods.

The open question, however, is whether this approach can be scaled down to sub-10 nm structuring. The approximations taken within the analytical theories are no longer valid when the size of the structures on the mask starts to be comparable with the wavelength of radiation, i.e. when the boundary influence cannot be neglected in the description of diffraction. Moreover, the analytical theories cannot reliably take into account the influence of polarization, the properties of absorber and the complex mask geometry. Therefore, we employed Maxwell's equations solver utilizing finite-difference time-domain method (FDTD) [2000 Erdmann] to investigate the scalability limits of EUV achromatic Talbot lithography.

7.2.3 METHODOLOGY

In FDTD method optical properties of the mask and the electric and magnetic field components are defined on a grid. In the following simulations [Web DrLiTHO], a cell size in the solver was set to $\lambda/15$, which provides better than 2% accuracy and the integration time was varied to achieve required convergence in all simulations.

The parameters of the lithography system in the simulation were chosen according to the parameters of high power discharge plasma EUV sources [2009 Bergmann] and recently developed transmission mask technology [2012 Brose].

For simulation of the broadband Talbot effect a Xe/Ar mixture spectrum with a peak at 10.9 nm and a 3.2% bandwidth from a laboratory EUV source was used (Fig. 7.2.1). In order to achieve a stable result, the broadband spectrum has to be approximated with a sufficient number of weighted monochromatic waves. In this work, the experimental spectrum form was approximated with ~ 100 wavelengths with 0.02 nm steps.

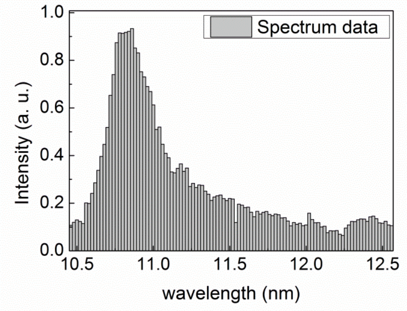

Fig. 7.2.1 The EUV broadband spectrum produced by laboratory source used for simulations

A crucial element for such simulations is the transmission mask. A simulated mask layout is shown in Fig. 7.2.2, repeating the design developed in [2012 Brose]. The intensity of the incident light is set to unity and the extinction coefficient of the membrane is set to 0, so the light intensity stays unity at the plane of conjunction between membrane (Nb) and absorber (Ni). The thickness of the absorber is 100 nm and is kept constant in all simulations.

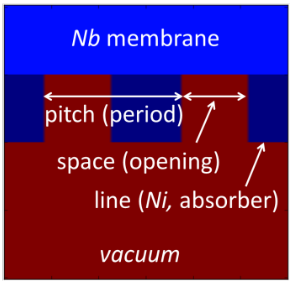

Fig. 7.2.2 The mask layout used in simulations. Optical parameters used: niobium (Nb) membrane n = 0.96228, nickel (Ni) absorber: n = 0.95627 – i0.04792 at 10.9 nm, where n is real and imaginary part of the refractive index [Web Henke]

The period of the pattern on the mask was varied from 10 to 100 nm, corresponding to half-pitch range between 5 and 50 nm. The space to pitch ratio (see Fig. 7.2.2) was set to 0.5 for all simulations except for studies of the influence of the ratio on the pattern's quality.

The FDTD simulations were performed for both transverse electric (TE) and transverse magnetic (TM) polarizations of the incoming radiation. The TE polarization describes linearly polarized light with an electrical field vector directed perpendicular to the plane of incidence, which is defined by vector normal to the plane of the grating and the gratings vector (see Fig. 7.2.3).

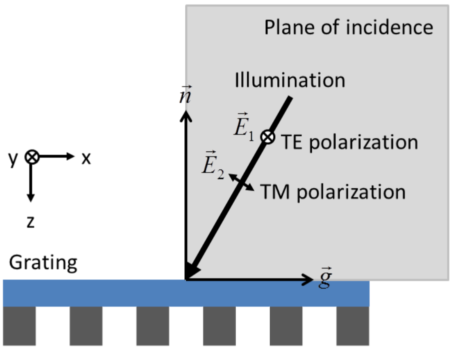

Fig. 7.2.3. Scheme of the setup for polarization dependent simulations

In the case of the TM polarization the magnetic field is transverse to the plane of incidence and the electric field vector is in-plane. Un-polarized radiation was simulated by summing and averaging over intensities produced by both polarizations. The Cartesian coordinate system in the Fig. 7.2.3 describes coordinates used in the presentation of the simulation results. Here z-axis describes distance from the mask in the propagation direction, with zero positioned at the top of the absorber layer.

The contrast was calculated in the resulting aerial image. For the cases where patterns with several peaks of different intensities were observed, the intensity of the lowest peak was used for the calculation of the contrast.

7.2.4 RESULTS AND DISCUSSION

Monochromatic illumination

The first set of simulations was conducted to investigate the scalability of monochromatic Talbot lithography. In this case there is no period demagnification, but pattern contrast values are expected to be significantly higher than in broadband/polychromatic case.

A typical simulated Talbot pattern is shown in the Fig. 7.2.4 for three different polarization cases.

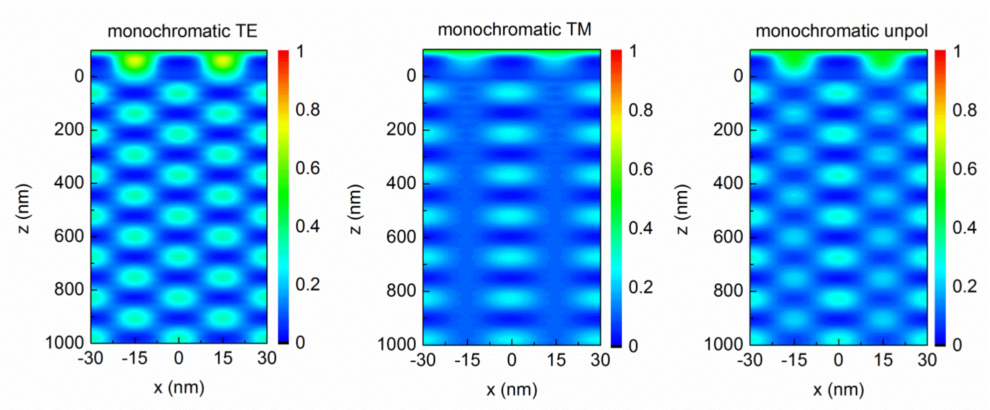

Fig. 7.2.4. Monochromatic Talbot patterns for 15 nm half-pitch for TE (left), TM (middle) and unpolarized (right) radiation.

First thing to note is that the non-shifted Talbot planes are almost absent in the case of TM polarization (Fig. 7.2.4 middle). This means that for non-polarized light, represented here as an average sum of TE and TM polarized intensities there will always exist a difference in intensity of shifted and not shifted Talbot planes. The dependence of Talbot effect on polarization has attracted considerable attention recently [2006 Lu, 2008 Zheng, 2010 Teng]. It was shown that the difference between TM and TE polarization becomes more pronounced for periods comparable to the wavelength of radiation, with TM mode vanishing completely when λ = d [2010 Teng]. In the case of EUV transmission gratings, the thickness of the absorber is normally significantly larger than the wavelength. This may explain the differences observed in diffraction of the TM mode in our simulations in comparison with the results of other authors, performed for gratings significantly thinner than wavelength. Detailed analysis of the polarization dependence will require simulation of different mask designs and will be topic of a future work.

The EUV radiation is relatively easy to polarize by using reflection off a multilayer mirror under Brewster angle [1986 Khandar]. In fact, in many practical EUV systems the radiation is reflected off at least one multilayer mirror before reaching a mask, so, at least in the case of one-dimensional grating, it is possible to realize a TE-mode of illumination.

In this case, the resulting patterns demonstrate excellent contrast all the way down to 10 nm half-pitch (Fig. 7.2.5). The contrast of monochromatic Talbot planes almost does not change until 20 nm half pitch, where it starts to decrease and reaches 70% at the lowest half pitch investigated. The intensity at maximum decreases steadily with pitch size, with accelerated drop below 20 nm half-pitch.

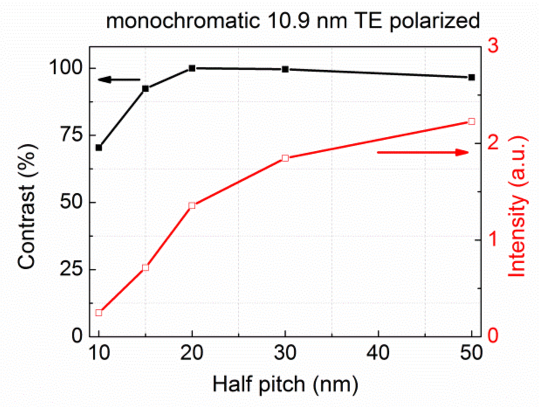

Fig. 7.2.5 Intensity and contrast curves as a function of the half pitch of mask under monochromatic illumination with TE polarized wave at 10.9 nm wavelength; The ratio of space to pitch was kept at 1:2.

It is possible to increase the peak intensity by increasing the opening's size on the mask, while keeping the pitch constant. The results of simulation for 30 nm half-pitch are presented in Fig. 7.2.6.

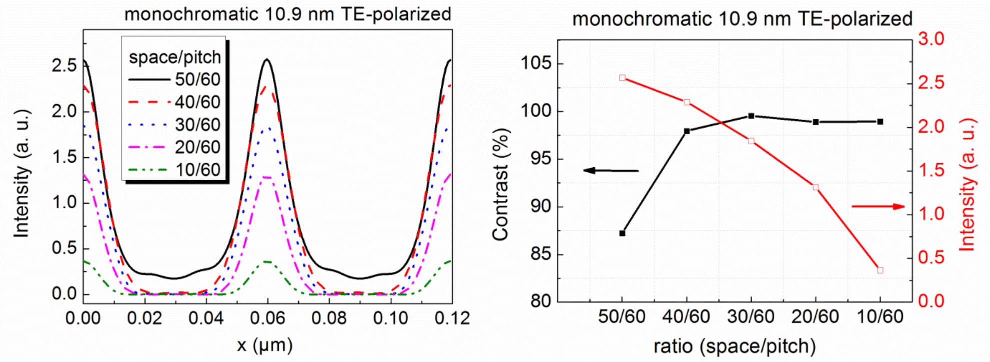

Fig. 7.2.6 Simulated intensity profiles (left) and dependence of maximal intensity and pattern contrast on the ratio of the space to pitch (right)

One can see that increasing the space between the lines above 30 nm helps to increase the intensity, but also leads to the loss of contrast in the image. Still, even for 50 nm spaces the theoretical contrast is above 87 % with more than 28 % increase in intensity in comparison with 50% fill factor gratings, which would allow for significantly higher throughput. At the same time, the increase of the absorber width beyond 50% fill factor decreases the maximal intensity without benefiting the contrast.

Broadband illumination

The broadband illumination is represented in the simulation as an incoherent sum of weighted intensities of monochromatic waves. The shorter wavelength yields a longer Talbot distance, while the longer wavelength yields a shorter Talbot distance. As a result, the different wavelengths mix and form a constant intensity along the propagation axis starting at a specific distance (Talbot mixture length, z_M) [2000 Guerineau].

The simulated propagation for 15 nm half pitch grating is shown in Fig. 7.2.7 for polarized and un-polarized light. Interesting to note that even though the mixture starts to happen at around the distance z_M=5.1 μm, the stability of patterns improves with further increase of the distance. The aerial image cross-sections that are shown in the Fig. 7.2.8 for TE polarized and un-polarized light were obtained at a 6 μm distance, which is maximal simulated distance for this period.

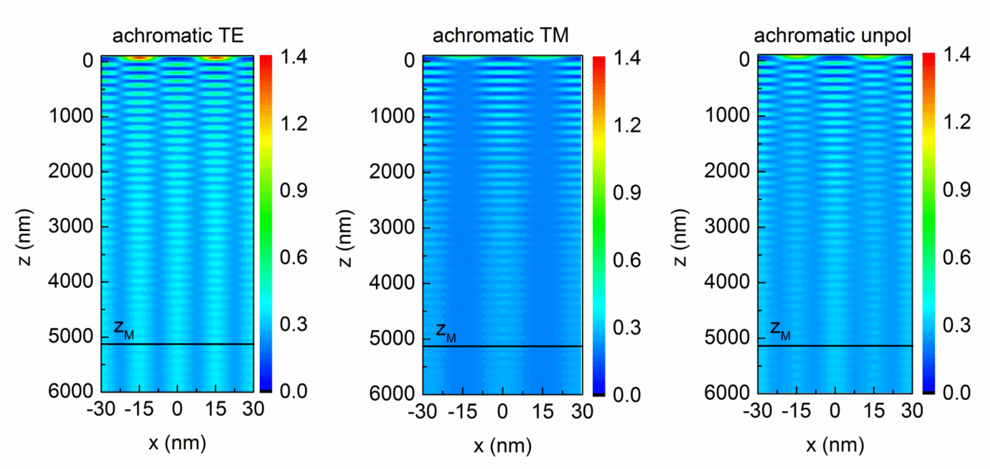

Fig. 7.2.7 Achromatic Talbot patterns with TE, TM and un-polarized illumination (left to right) for 15 nm half pitch grating

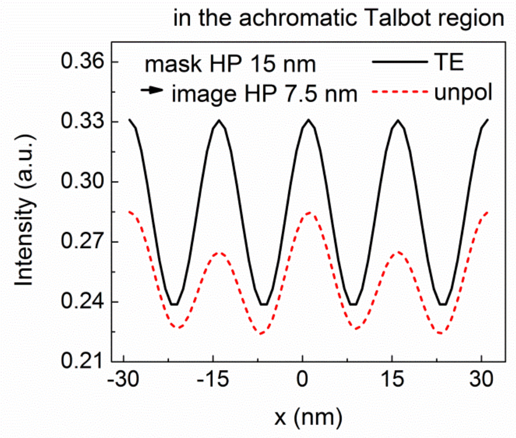

Fig. 7.2.8 The cross-sections of aerial images for achromatic TE and un-polarized illumination at a distance of 6 μm from the grating. The resulting aerial image half pitch is 7.5 nm

As predicted analytically, the doubling of the frequency at this plane is visible, demonstrating 7.5 nm half pitch patterns in the achromatic Talbot region. On the other side, the contrast of the patterns in the case of un-polarized illumination is already below the Rayleigh resolution limit of ~13%.

Since lithography requires sufficient contrast for the image converting to the patterns in resist, the study of the contrast and maximal intensity in dependence on the pitch size was performed. The results are presented in the Fig. 7.2.9.

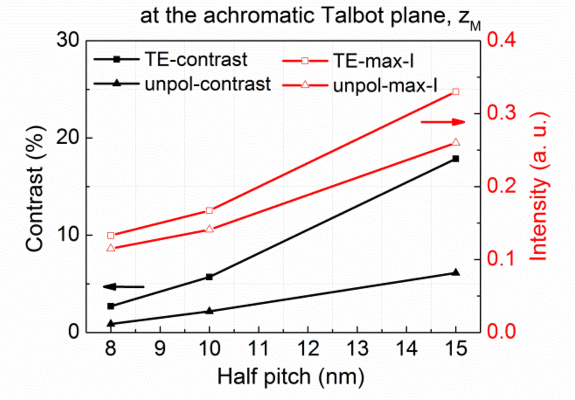

Fig. 7.2.9 Contrast and maximum intensity of achromatic Talbot patterns at the plane of z_M as a function of the half-pitch on the mask. The resulting half-pitch in the aerial image is a half of the masks half pitch

The gradual decrease of the maximum intensity and contrast with half pitch reduction on the mask is clearly visible. The contrast of the areal images is significantly lower than in the case of monochromatic Talbot printing. Using TE polarized light the contrast above ~16% can be maintained down to 15 nm half pitch on the mask, which corresponds to 7.5 nm half pitch on the wafer. For the investigated mask design this is realistically the resolution limit for broadband Talbot lithography at this wavelength. Interesting to note that simulations for 5 nm half pitch on mask have not revealed any demagnification effects in the achromatic Talbot region and only 1:1 self-images of the mask were observed with very low intensity and contrast.[§§§§] For large pitches the contrast and intensity are increasing. Due to memory limitations it was not possible to calculate the propagation beyond 6 μm distance after the mask, which is smaller than corresponding z_M distance. For 25 nm half pitch it was possible to extrapolate the propagation pattern to z_M, yielding contrast of 40.8% and peak intensity of 0.69 for TE polarized light.

Moving the wafer closer to the mask one can also expose the wafer in the quasi-monochromatic Talbot planes even with broadband illumination (see Fig. 7.2.7). In this case the pattern will be transferred from the mask without demagnification and with very narrow depth of field, but with significantly higher contrast.

The results of contrast and intensity simulation at the first Talbot plane can be seen in Fig. 7.2.10. In this case the contrast for TE polarized light for 8 nm half-pitch patterns is above 41% but drops below 10% for the 5 nm half-pitch 1:1 printing. The peak intensity

---

[§§§§] The unrevealing of the de-magnified pattern in the achromatic Talbot region for mask half pitch below 5 nm may be caused by the fact that in the simulation the intensity difference between the I_{max} and I_{min} is not distinguishable, not because of the physical reason but because of the resolution of calculation in the simulation.

also decreases rapidly going into sub-wavelength half-pitch sizes, which, in turn, will increase the required exposure time for such structures.

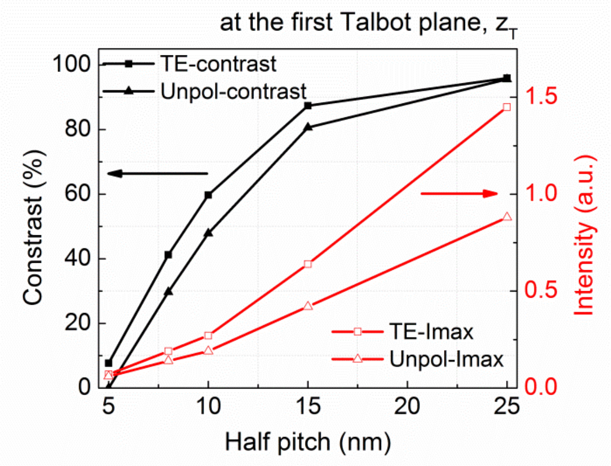

Fig. 7.2.10 The contrast and intensity curves at the first Talbot plane in dependence on the half pitch on the mask

One should not forget that in this case the wafer should be in the sub-micrometer proximity to the mask, which is difficult to realize reliably and the mask should be manufactured with the same resolution as the targeted wafer structures.

7.2.5 CONCLUSION

In conclusion of this chapter, we have theoretically investigated the scalability of Talbot EUV lithography with laboratory EUV plasma sources. FDTD simulations have demonstrated that the structuring with monochromatic and achromatic Talbot lithography can be effectively used with amplitude transmission masks. It was shown that with broadband illumination of a gas discharge plasma source it is possible to utilize achromatic Talbot effect to achieve 2:1 demagnification of masks period. The contrast and intensity of the resulting aerial image were shown to decrease with reduction of the pitch size. The practical resolution limit in the achromatic Talbot regime was estimated to be at 7.5 nm half pitch for TE polarized illumination for the given wavelength of light. 1:1 printing in a monochromatic Talbot configuration allows for higher contrast at small pitches but it is harder to realize experimentally due to higher requirements on masks resolution and smaller required distance between a mask and a wafer.

7.3 TALBOT CARPETS IN NANO-SCALE

Single exposure imaging of Talbot carpets and resolution characterization of detectors for micro- and nano- patterns

In this section, we demonstrate a self-imaging technique that can visualize longitudinal interference patterns behind periodically-structured objects, which are often referred to as Talbot carpets. Talbot carpet is of great interest due to ever-decreasing scale of interference features. We demonstrate experimentally that Talbot carpets can be imaged in a single exposure configuration revealing a broad spectrum of multi-scale features. We have performed rigorous diffraction simulations for showing that Talbot carpet prints can produce ever-decreasing structures down to limits set by mask feature sizes. This demonstrates that large-scale pattern masks may be used for direct printing of features with substantially smaller scales. This approach is also useful for characterization of image sensors and recording media.

7.3.1 INTRODUCTION

We present a submicron patterning method for optical Talbot carpet in a single exposure configuration. We also demonstrate a rigorous simulation for Talbot carpet in nano-scale. In principle, the Talbot carpet originally has an analogy in quantum physics referred to as the "quantum carpet", which describes the behaviour of localized wave packets, which undergo revivals in time [2000 Friesch]. The Talbot carpets are also found in atomic physics [1995 Chapman], in plasmonics [2007 Dennis, 2009 Cherukulappurath], and especially in wave propagation in coherent optics.

A Talbot carpet of light is a longitudinal section (in direction of propagation) of the interference pattern behind a 1-dimensional transmission grating illuminated by a coherent plane wave. An image of the Talbot carpet contains fractional profiles of a master grating at rational multiples of the Talbot distance. It also contains profiles of fractal Talbot patterns at irrational fractions of the Talbot distance [1996 berry, 2001 berry, 2012 Segev].

Accordingly, the Talbot carpet is highly interesting since the scaling down of feature size is among the critical issues and challenges for submicron to nano-patterning [1965 Moor, 2013 ITRS].

In a Talbot image, the repeating patterns are not only seen at positive integer multiples of the Talbot length, $n \cdot z_T$, but also at fractional intervals, $\{(p/q) \cdot z_T/2\}$, where p and q are co-prime positive integer numbers [1996 Berry, 1992 Latimer, 2006 Rosu]. While fractional Talbot patterns are cross-sections of intensity distribution orthogonal to the light propagation axis, patterns at the plane containing the optical axis are referred to as a “Talbot carpet” or “carpet of light” [2001 Berry].

The visualization of the optical Talbot carpet is usually performed by computer integration of images recorded by a digital camera at different distances from the grating [19997 Nowak, 2009 Case, 2000 Guerineau, 2003 Guerineau]. However, in order to obtain the image of the Talbot carpet, a large number of such high-resolution images is required.

First, the measurements were done in the visible spectral range and with a large period grating, which made the measurement simpler. Particularly, in the case of submicron gratings, the spatial resolution of optical detectors is not sufficient, so a good way to image the pattern is to record each plane by exposure of photo-sensitive materials such as photoresists [2015 Mojarad]. However, this is a tedious and time-consuming procedure requiring repeated nano-meter precise positioning of the photoresist plane. Therefore, we consider a single exposure imaging method that can record the high-resolution structure of Talbot carpets over a wide range of propagation distances without missing image planes, which can also become a fundamental technique to investigate and utilize the nano Talbot carpets.

In simulation, we study further for a non-paraxial case of Talbot pattern employing finite-difference time-domain (FDTD) simulation by the “DrLitho” simulator [2006 Erdmann, 2013 Danylyuk]. In this demonstration, extreme ultraviolet (EUV) radiation is used, which can be realized lithographically [2005 Solak]. We analyse image properties especially in the rational and irrational intensity profiles in the Talbot carpet. The simulation results show the single exposure configuration for a Talbot carpet can produce ever-decreasing periodicities in the nano-scale down to the diffraction limit in intensity profiles.

7.3.2 ANALYSIS OF TALBOT CARPET

Images of Talbot carpet

As mentioned, the Talbot pattern is a Fresnel image that can be calculated by the angular spectrum representation within Fourier optics [1996 Goodman]. This solution is valid under the paraxial approximation when $d^2/z > \lambda$. The intensity distribution behind a grating is shown in Fig. 7.3.1. The initial intensity distribution is considered as a binary transmittance, $u(x, z=0) = 1$ within the opening and $u = 0$ within the absorber line (slit width = 0.1 × period), where x is the coordinate perpendicular to the grating rulings and z is the axis of the illuminating light-wave propagation. The object is assumed as an ideal binary periodic grating that is infinitely repeated along the x- and y- axes. The Talbot pattern is formed behind this object through the space.

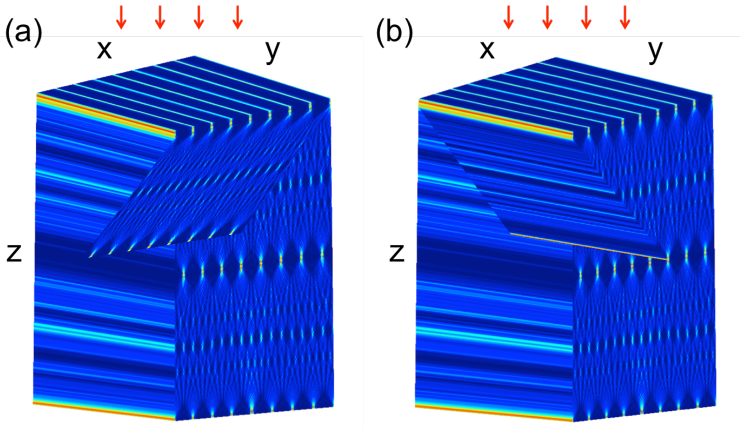

Fig. 7.3.1 Talbot pattern behind a grating in space under coherent plane illumination from top: Traditional Talbot carpet is seen in x-z plane. Both diagonal cross-sections display (a) Talbot carpet, and (b) a pattern consisting of various pitches.

Considering the diagonal cross-sections through the 3-dimensional (3D) image of the Talbot pattern, such a cross-section as shown in Fig. 7.3.1 (a) shows the Talbot carpet stretched in the z-direction in comparison to the conventional Talbot carpet formed just in the x-z plane. This diagonal cross-section contains the complete Talbot carpet, because all details of the intensity distribution at each z-position are included in those tilted 2D images (diagonal cross-section in Fig.7.3.1 (a)). In the space of the Talbot pattern, another diagonal cross-section in Fig. 7.3.1 (b) is the line-and-space image rather than the traditional Talbot carpet image, which consists of gradually smaller (or bigger) pitches between neighbours.

Single exposure imaging of Talbot carpet

The method uses a fact that the Talbot carpet is actually located over x-, y-, z-axes, while the conventional method is to scan the profile in the x-axis through the propagation axis as mentioned (see the axis definition in Fig. 7.3.2). Here we use diagonal cross-sections in the 3D Talbot pattern to obtain a full image of the Talbot carpet. The object in this case is an ideal binary line-space grating, which is infinitely repeated with a certain period. The object has no variation along the y-axis, and so for the interference image behind the grating, no intensity change exists along the y-axis, while the intensity is modified along the x-axis.

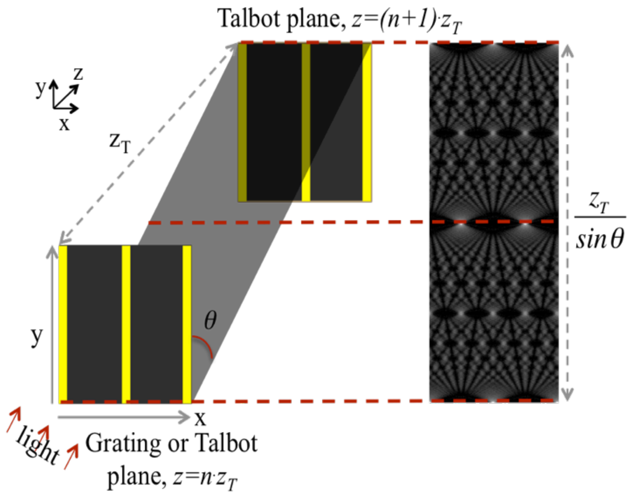

Fig. 7.3.2 The geometrical concept of the single exposure imaging of Talbot carpet

Thus, in the x-y plane at any Talbot distances ($z = n\cdot z_T$, n is positive integer), a cross-section at y = y’ (any value) is identical. A diagonal plane placed with one side at a Talbot plane ($z = n\cdot z_T$) and with its other side at the following Talbot plane ($z = (n+1)\cdot z_T$) with any different y-position as shown in Fig. 7.3.2 contains full information about the Talbot pattern. Therefore, a Talbot carpet can be constructed from the image recorded by a planar detector such as a digital camera or photoresist coated wafers positioned diagonally in the single exposure configuration.

7.3.3 RESULTS

Experimental demonstration: imaging of the Talbot carpet

In this section, we demonstrate imaging of Talbot carpets in experiments. The exposure was performed with plane wave illumination generated by a highly coherent HeNe laser ($\lambda = 632.8$ nm). The incident beam has illuminated a transmission mask that is a laser-milled steel grating consisting of 60 µm pitch and 10 µm slit width. The grating field size in the mask was 10 mm × 10 mm. A high-resolution complementary metal–oxide–semiconductor

(CMOS) image sensor was used to detect the image. The resolution of the image sensor is 1280 × 1024 pixels in 6.6 mm × 5.3 mm area. Fig. 7.3.2 displays the experimental setup showing configuration of the grating mask and the detector. The detector plane was aligned diagonally as in Fig. 7.3.1 (a) with an angle of around $\theta = 45°$.

Fig. 7.3.3 (a) shows the result where the Talbot carpet is obtained by the single exposure configuration. The image is recorded in z range between $z=z_T$ and $z=2\cdot z_T$, which corresponds to a full Talbot period. The intensity discontinuity in the middle of Fig. 7.3.3 (a) occurred due to repositioning of the detector that covers a half of the z_T (~1 mm).

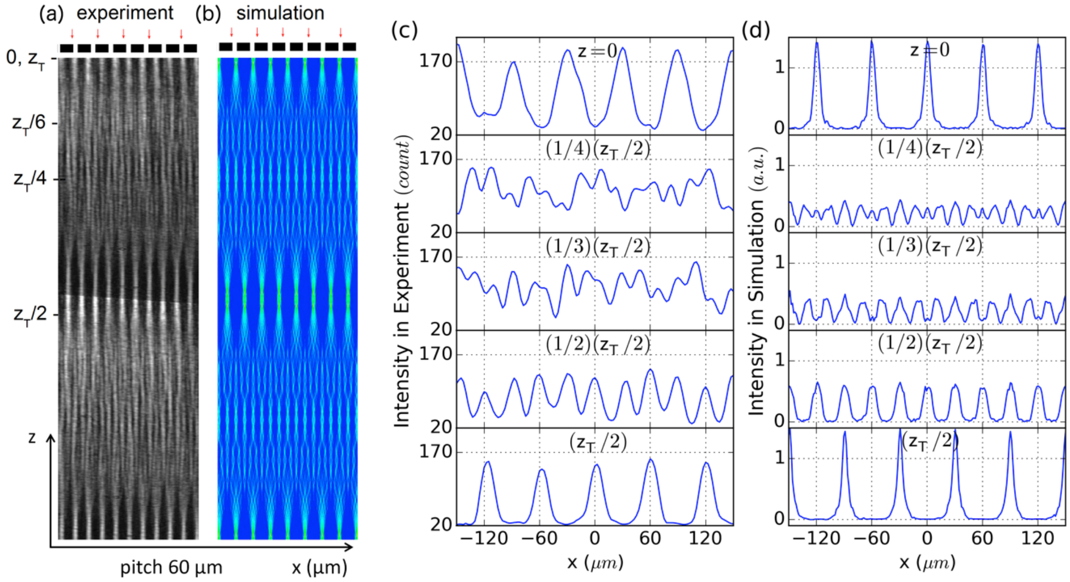

Fig. 7.3.3 (a) The experimental image of Talbot carpet, (b) the simulated image of Talbot carpet and the intensity profiles of (c) experimental and (d) simulated data at several fractions of the Talbot distance.

The resulting image is stretched in propagation direction due to the tilt in comparison to the traditional Talbot carpet formed in the x-z plane. The stretched length (Talbot period) in the tilted plane is magnified by $1/\sin\theta$, where θ is an angle of the detector plane from grating plane. Thus the period of Talbot carpet (z_T) becomes $\{z_T/\sin\theta\}$ in the detector. Intensity profiles of the Talbot carpet in experiment and simulation are plotted in Fig. 7.3.3 (c) and (d) respectively. The spatial frequencies of particular patterns exhibit integer multiples of that of master object at $\{z=(1/M)(z_T/2)\}$, where M is a positive integer, which corresponds to spatial frequency multiplication.

This method allows characterizing the capability of detectors particularly in terms of resolution. In this demonstration, we used a conventional CMOS imaging sensor, which consists of ~ 5.2 μm period between photodiodes. However as can be seen in Fig. 7.3.3 (c), the detector can distinguish the intensity profile up to M=3, while simulation performs up to M=4. It implies that the resolution of the detector is around 20 μm. In principle, at least three pixels are required to detect a pitch, which corresponds to 15.6 μm, but imperfect grating features affect the image contrast. Thus, resolution can be smaller than 20 μm, but not smaller than 15 μm as in theory. The visibilities for intensity profiles in the experiment are compared with the ones in simulation where visibility is defined as: $\{V=(I_{MAX} - I_{MIN})/(I_{MAX} + I_{MIN})\}$. Visibility in the experiment (V_1) is decreased in comparison with visibility in the simulation (V_0) over fractional Talbot patterns. Thus, detection error (%): $\{(1-V_1/V_0)\times 100\}$ is increased as M is increased as shown in Fig. 7.3.4. The error is nearly 40 % for 30 μm period pattern.

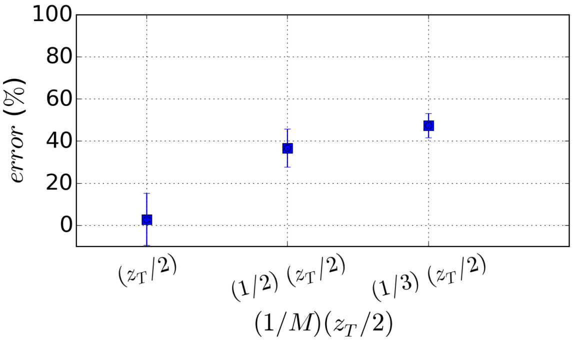

Fig. 7.3.4 Visibility errors by detector for fractional Talbot patterns

While the Talbot carpet is visualized with a detector positioned perpendicular to the rulings and tilted in the y-z plane as shown in Fig. 7.3.1 (a) for a horizontal grating, on the other hand, another pattern can be observed with a detector positioned parallel to the rulings and tilted in the x-z plane as shown in Fig. 7.3.1 (b) [1988 Thomas]. Such a result obtained in our experiment is presented in Fig. 7.3.5 (a). The cross-sectional curves (1D profile) of the tilted image (2D image such as a diagonal section in Fig. 7.3.1 b) are displayed in Fig. 7.3.5 (a) in the range of a half Talbot distance. This profile exhibits various gaps between the peaks through the groove. The gradually increased or decreased gap through the groove is seen in a line-art profile as shown in Fig. 7.3.5 for simulation (top) and experiment (bottom), while the profiles of the fractional Talbot pattern show a regular gap as shown in Fig. 7.3.3 (c, d). The gaps (peak to peak) are magnified by (1/sinθ) in comparison with the gaps in fractional Talbot intensity profiles due to the broadening by tilt.

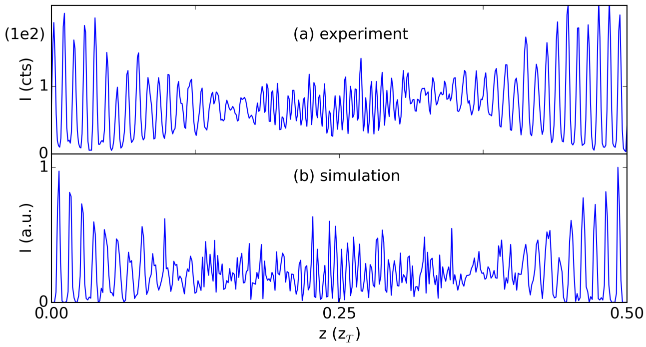

Fig. 7.3.5 Intensity profiles along the groove in the diagonal cross-section in Fig. 7.3.1 (b) in experiment (top) and in simulation (bottom)

Talbot carpet in nanoscale: FDTD simulation

In this section, we demonstrate FDTD simulations with EUV radiation at 13.5 nm wavelength in order to observe the smallest feature in the Talbot carpet. By employing FDTD simulation we can predict the smallest feature in Talbot carpet that will form in the area close to the grating, where the Fresnel-Kirchhoff assumption is not valid. In this regime, the multiple-slits interference influence is reduced but the single slit diffraction features become more important. With slit width approaching the wavelength of light the system is entering a non-paraxial regime requiring rigorous calculation. The optical properties of the Talbot image, particularly the intensity, the contrast and the interference fringes quality are dependent on the geometry of the mask and the choice of materials. The large contrast between the transmission of the opening and of the absorber is required and the transmittance has to be optimized with the efficient thickness of the layers for both substrate and absorber in order to obtain the sharper image of the Talbot carpet. For example, in the model demonstration for the mask, the pitch was 300 nm, the opening-width was 20 nm and the line-width was 280 nm. The gold is deposited as an absorber layer (60 nm) on Si_3N_4 membrane (20 nm). This feature is realistic in current mask fabrication technology for EUV radiation [2012 Brose]. X-ray data for optical properties of materials in [Web Henke] were used in the simulation.

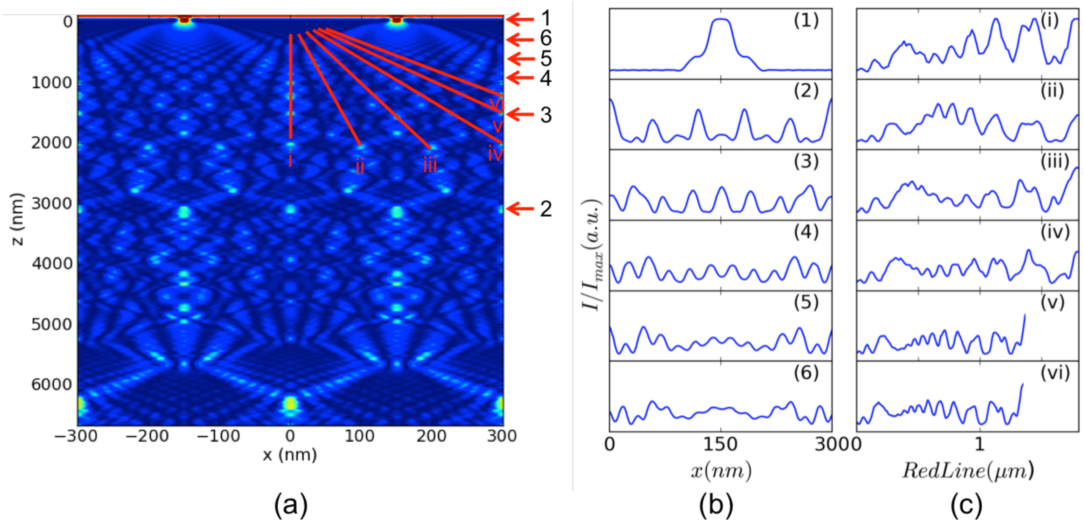

Fig. 7.3.6 (a) Talbot carpet calculated by FDTD simulation: (b) and (c) are intensity profiles along various detecting planes

Fig. 7.3.6 (a) displays the simulated image of the Talbot carpet behind the grating in the range of z = 0 to $z_T/2$ (0 - 6670 nm). The Talbot carpet in nano-scale is obtained in this case. Fig. 7.3.6 (b) and (c) are intensity profiles that are determined at positions marked with red arrows (1)-(6) and red lines (i)-(vi) in Fig. 7.3.6 (a). In both cases, intensity profiles reproduce self-images progressively at smaller scales from 300 nm to 10 nm pitches depending on the detector plane such as planes at normal to z-axis (1-6) or tilted planes (i-vi).

For the case of fractional Talbot pattern as shown Fig. 7.3.6 (b), spatial frequency is multiplied by up to a factor 15, which results in a corresponding half pitch of 10 nm. The visibility was from 2 % at worst and 26 % at best. In Fig. 7.3.6 (c), the fractal Talbot intensity is shown at irrational cross-section as described by Berry [2001 Berry, 1967 Mandelbrot]. In this case, the width of peaks is decreased along the curves until no peak appears. The contrast is also decreasing as the width decreases and it finally becomes zero at some point, which corresponds to the diffraction limit.

7.3.4 DISCUSSION

In comparison to conventional methods, the single exposure imaging method enables fast imaging of Talbot carpets, and also depth of focus becomes less critical, because no differential positioning of the detector is required. The experiment can be performed despite the imperfect quality of the grating due to the fact that the Talbot effect reproduces the self-image with modified quality from the grating [1989 Partorski, 2013 Wen]. This is a well-known effect. However, this is an advantage when applying the method with gratings of smaller pitch.

The single exposure imaging method could be applied for rapid characterization of sources in metrology, where the wave propagation image over near- and far- fields is used for the analysis [2000 Guerineau]. The method also enables printing Talbot carpets on photoresist samples using an interference lithography technique. Nano scale Talbot carpet and fractal Talbot patterning may be feasible utilizing this method.

The rigorous diffraction simulation model has shown that the nanoscale Talbot carpet can be obtained under a coherent extreme ultraviolet illumination. Sub-10 nm scale structures may be realized in this case, while the conventional methods can hardly achieve that. The Talbot effect is valid within the limitation that no evanescent fields are present, and so spatial resolution is limited by diffraction. Thus, a highly efficient diffraction mask and a good coherent illumination exposing large area are required. The standard sample suggested in the FDTD simulation is a good example in this case.

We also suggest that structuring of Talbot carpets can be used for characterization of photoresist. While conventional deep ultraviolet optical lithography meets the demand to continuously shrink device structures, further steps of structure miniaturization can be obtained by EUV lithography [2010 Wagner]. The resolvability of photoresist becomes important in sub-10 nm lithography [2015 Mojarad]. Thus this work may be potentially useful for applications of nano-lithography with highly coherent EUV sources [2014 Chun]. Other possible applications would be nano-structuring of quantum dot arrays, nano-photonic devices, and nano-crystals. [2006 Ozbay, 1996 Krauss, 1988 Reed].

7.3.5 CONCLUSION

We present an imaging technique that can perform visualization of Talbot carpets very simply and also precisely. Talbot carpet includes fractional and fractal patterns that feature ever decreasing periodicities in intensity profiles even though a large-scale period in mask is used. The experiment demonstrates that Talbot carpet as a whole can be reproduced in a single exposure configuration. The conventional Talbot carpet and another cross-sectional pattern are visualised with tilted detectors, where the tilting is in the range for detectable angle. It is shown that the method can be applied for resolution characterization of detectors. The method enables characterizing the resolvability of photoresist with high-resolution Talbot image produced by short wavelength radiation. Talbot carpet in nano-scale can be produced with the method introduced here, while conventional methods can hardly achieve this. We utilize FDTD simulations in order to observe the smallest feature of Talbot carpet in non-paraxial condition. Structures down to 10 nm are achieved using a 300 nm pitch mask and 13.5 nm wavelength illumination. It may be feasible structuring of Talbot carpet in nano scale lithographically as suggested. The method could be potentially useful for characterization of light sources, nano-structuring, or applications in photonic devices.

Conclusion

Summary

In this thesis, interference lithography with extreme ultraviolet (EUV) light is studied. In order to improve the resolution of patterns obtained using different radiation sources in the extreme ultraviolet spectral range, different interference patterning methods are investigated. In experimental study, compact size EUV sources are utilized to demonstrate interference lithography. In simulation study, EUV illumination under specific conditions e.g. regarding coherence or polarization is investigated to demonstrate the interference patterning methods. For lithographic applications of the compact EUV sources, we also analyze the optical properties of three different compact EUV sources for interference lithography with regard to capability and feasibility of nanopatterning.

In experiment, Lloyd's mirror interference lithography (IL) is performed with the monochromatic EUV illumination generated by a high harmonic generation (HHG) source. The feasibility of using HHG for IL is discussed in regard to the achievable resolution and interference area of printed pattern. Contact lithography and proximity lithography are demonstrated with EUV radiation from a discharge produced plasma (DPP) source with Xe/Ar gas mixture to create complex nanoarrays. EUV-Talbot lithography is demonstrated with several optical designs capable of overcoming the limitation of optical properties of particular compact EUV sources. In the result, the interference patterns are reproduced with very fine details on a photoresist. The printed results of 1D, 2D periodic or complex patterns are compared to the theoretical prediction, and good agreement is seen. Also the restorative self-imaging effect has been analyzed for a rough-line grid from the point of view of the fidelity of the image.

In simulation, the scalar diffraction and rigorous diffraction simulation models are used in both the paraxial and non-paraxial regimes. The validity of both approaches is discussed to predict the nanostructures for particular EUV sources. The scalar diffraction simulation is used to demonstrate nanopatterning with compact EUV sources in Fresnel diffraction regime. The optical wave propagation through isolated apertures or gratings of different mask layouts is calculated and compared for both methods in order to verify the validity of the simulation methods for the patterning in nanoscale. Also the rigorous propagation simulations are performed for the fractional Talbot pattern, achromatic Talbot pattern, and

Talbot carpet consisting of ever-decreasing features. The possibilities and limitations of Talbot lithography under EUV illumination are explored.

Outlook

We envision achieving high-density patterns in experiments utilizing the well-defined masks and short-wavelength coherent sources in Talbot lithography. Lloyd's mirror interference lithography using high harmonic generation source is promising technology to obtain sub 20 nm structures in a laboratory setup owing to the high coherence of the radiation. In contact and proximity lithography, the methods can be developed further with the precise distance control and the alignment of the system. Some successful theoretical demonstrations could be experimentally demonstrated including fractional Talbot lithography, achromatic Talbot lithography, and Talbot carpet of nanoscale.

References

1836 H. F. Talbot, “LXXXVI. Facts relating to optical science No IV”, Phil. Mag. Series 3, 9(56), 401-407.

1881 L. Rayleigh, “XXV. On diffraction-gratings, and on some phenomena connected therewith”, Phil. Mag. Series 5, 11(67) 196-205.

1957 B. J. Thompson, E. Wolf, “Two-Beam Interference with Partially Coherent Light”, J. Opt. Soc. Am. 47(10), 895-902.

1957 J. M. Cowley, A. F. Moodie, “Fourier images I - The point source”, Proc. Phys. Soc. B 70(5), 486-496.

1965 G. E. Moore, “Cramming More Components onto Integrated Circuits,” Electronics Magazine 38(8), 114-117.

1965 J. T. Winthrop, C. R. Worthington, “Theory of Fresnel Images. I. Plane Periodic Objects in Monochromatic Light”, J. Opt. Soc. of Am., 55(4), 373-381.

1966 K. Yee, “Numerical solution of initial boundary value problems involving maxwell's equations in isotropic media”, IEEE Trans. Ante. Prop. 14(3) 302-307.

1967 B. Mandelbrot, “How Long Is the Coast of Britain? Statistical Self-Similarity and Fractional Dimension”, Science 156(3775), 636-638.

1967 W. D. Montgomery, “Self-imaging objects of infinite aperture”, J. Opt. Soc. Am. 57(6), 772-775.

1969 R. F. Edgar, “The Fresnel diffraction images of periodic structures”, Opt. Acta.16(3), 281-287.

1971 H. Dammann, G. Groh, M. Kock, “Restoration of Faulty Images of Periodic Objects by Means of Self-Imaging”, Appl. Opt. 10(6), 1454-1455.

1972 D. Spears, H. Smith, “High-resolution pattern replication using soft x rays”, Elec. Letters 8(4), 102-104

1974 E. Hecht, A. Zajac, “Optics”, Addison-Wesley publishing company, Inc.

1974 G. Bjorklund, S. Harris, J. F. Young, “Vacuum ultraviolet holography”, Appl. Phys. Letters 25(8), 451

1975 F. Dill, W. Hornberger, P. Hauge, and J. Shaw, “Characterization of Positive Photoresist”, IEEE Trans. Elec. Devices 22, 445-452.

1975 G. R. Fowles, “Introduction to Modern Optics 2nd edition” (Dover publication, Inc., New York).

1979 D. D. Flanders, A. M. Hawryluk, Henry I. Smith, “Spatial period division - A new technique for exposing submicrometer-linewidth periodic and quasiperiodic patterns”, J. Vac. Sci. Technol. 16(6) 1949-1952.

1980 A. Taflove, “Application of the finite-difference time-domain method to sinusoidal steady-state electromagnetic-penetration problems”, IEEE Trans. Electro. Compatibility, EMC-22(3) 191-202.

1981 K. Patorski, G. Parfjanowicz, “Self-imaging phenomenon of a sinusoidal complex object”, Optica ACTA 28(3), 357-367.

1984 K. Patorski, "Heuristic explanation of grating shearing interferometry using incoherent illumination", Optica Acta 31(1), 33-38.

1984a K. Patorski, P. Szwaykowski, "Optical differentiation of quasi-periodic patterns using Talbot interferometry", Optica Acta, 31(1), 23 -31.

1985 D. S. Burch, “Fresnel diffraction by a circular aperture”, Am. J. Phys. 53, 255.

1985 N. Bolognini, J. Ojeda-Castaneda, E. E. Sicre, "Interferometry based on the Lau effect A quasi-ray description", Optica Acta 32(4), 409-422.

1985 P. Andres, J. Ojeda-Castaneda, J. Ibarra, "Lensless theta decoder", Opt. Comm. 60(4)

1985 V. V. Aristov, S. Aoki, A. I. Erko, S. Kikuta, V. V. Martynov, “Observation of Fourier images in soft x-ray radiation”, Opt. comm. 56(4).

1986 A. Khandar, P. Dhez, M. Berland, "Study of multilayers X-UV polarizers and consequence of the use of partially polarized light on absolute reflectivity measurements," Proc. SPIE 688, 176-183.

1988 A. Heuberger, “X-ray lithography”, J. Vac. Sci. Technol. B 6, 107.

1988 J. Thomas, “Binaere Phasenelemente in Photoresist”, Diploma thesis, Friedrich-Alexander-Universität Erlangen-Nürnberg, Germany.

1988 M. Reed, J. Randall, R. Aggarwal, R. Matyi, T. Moore, A. Wetsel, "Observation of discrete electronic states in a zero-dimensional semiconductor nanostructure", Phys. Rev. Lett. 60(6), 535–537.

1988 M. Reed, J. Randall, R. Aggarwal, R. Matyi, T. Moore, A. Wetsel, "Observation of discrete electronic states in a zero-dimensional semiconductor nanostructure", Phys Rev Lett 60(6), 535–537.

1989 K. Patorski, The self-imaging phenomenon and its applications, Progress in optics XXVII, edited by E. Wolf, pp. 2-108, Elsevier Science Publishers, Warsaw.

1990 A. Lohmann, J. Thomas. "Making an array illuminator based on the Talbot effect." Appl. Optics, 29(29) 4337-4340.

1992 F. Cerrina, “Recent Advances in X-Ray Lithography”, J. J. Appl. Phys. 31, 4178.

1992 P. Latimer and R. F. Crouse, “Talbot effect reinterpreted”, App. Opt. 31(1), 80-89.

1993 B. Henke, E. Gullikson, J. Davis, “X-ray interactions: photoabsorption, scattering, transmission, and reflection at E=50-30000 eV, Z=1-92”, Atomic Data and Nuclear Data Tables, 54(2), 181-342.

1993 E. Noponen, J. Turunen, "Electromagnetic theory of Talbot imaging", Opt. Comm. 98, 132-140.

1993 Z. Jerry, Y. Guo, and F. Cerrina, “Modeling X-ray proximity lithography”, IBM J. Res. Develop., 37 (3), p-331.

1994 M. Wei, D. Attwood, T. Gustafson, E. Anderson, “Patterning a 50nm period grating using soft xray spatial frequency multiplication”, J. Vac. Sci. Technol. B 12(6), 3648

1994 V. Arrizón, J. Ojeda-Castañeda, “Multilevel phase gratings for array illuminators”, Appl. Optics, 33(25), 5925-5931.

1995 M. Chapman, “Near-field imaging of atom diffraction gratings the atomic Talbot effect”, Phys. Rev. A 51(1), R14-17.

1995 S. Okazaki, “Lithography for ULSI”, Proc. SPIE 2438, 18-32.

1996 H. Smith, “X-ray lithography for microelectronics”, Physica Scripta, T61, 26

1996 J. W. Goodman, “Introduction to Fourier Optics 2nd ed.”, McGraw Hill, New York.

1996 J. Zhou, J. Peatross, M. Murnane, H. Kapteyn, “Enhanced High-Harmonic Generation Using 25 fs Laser Pulses”, Phys. Rev. Letters 76, 752.

1996 M. Berry, S. Klein, “Integer, fractional and fractal Talbot effects”, J. of Modern optics 43(10), 2139-2164.

1996 M. V. Berry, S. Klein, “Integer, fractional and fractal Talbot effects”, J. of Modern optics, 43(10), 2139-2164.

1996 T. Krauss, R. M. De La Rue, S. Brand, “Two-dimensional photonic-bandgap structures operating at near-infrared wavelengths”, Nature 383, 699-702.

1997 B. Besold, N. Lindlein, “Fractional Talbot effect for period microlens arrays”, Opt. Eng. 36(4) 1099-1105.

1997 F. Cerrina, “X-Ray Lithography”, in Handbook of Microlithography, Micromachining and Microfabrication, Volume 1: Microlithography, edited by P. Rai-Choudhury (SPIE, Bellingham, WA).

1997 M. C. Marconi, J. L. A. Chilla, C. H. Moreno, B. R. Benware, J. J. Rocca, “Measurement of the Spatial Coherence Buildup in a Discharge Pumped Table-Top Soft X-Ray Laser”, Phys. Rev. Lett. 79(15), 2799-2802.

1997 S. Nowak, Ch. Kurtsiefer, T. Pfau, C. David, “High-order Talbot fringes for atomic matter waves”, Opt. Lett. 22(18) 1430-1432.

1998 B. R. Benware, C. D. Macchietto, C. H. Moreno, J. J. Rocca, “Demonstration of a high average power tabletop soft X-ray laser”, Phys. Rev. Lett. 81(26), 5804-5807.

1999 C. Macchietto, B. R. Benware, J. J. Rocca, "Generation of millijoule-level soft-x-ray laser pulses at a 4-Hz repetition rate in a highly saturated tabletop capillary discharge amplifier". Opt. Letters, 24(16), 1115-1117.

1999 H. Solak, D. He, W. Li, S. Singh-Gasson, F. Cerrina, B. Sohn, X. Yang, and P. Nealey, “Exposure of 38 nm period grating patterns with extreme ultraviolet interferometric lithography”, Appl. Phys. Lett. 75, 2328.

1999 M. Born, E. Wolf, “Rigorous diffraction theory”, Ch. XI in Principles of optics 7th exp. Ed., Cambridge University Press, Cambridge.

1999 Y. Vladimirsky, A. Bourdillon, O. Vladimirsky, W. Jiang, Q. Leonard, “Demagnification in proximity x-ray lithography and extensibility to 25 nm by optimizing Fresnel diffraction”, J. Phys. D: Appl. Phys. 32, L114.

2000 A. Erdmann, C. Friedrich, “Rigorous diffraction analysis for future mask technology”, Proc. SPIE 4000, 684-694.

2000 D. T. Attwood, Soft X-Rays and Extreme Ultraviolet Radiation (Cambridge Univ. Press, Cambridge, UK)”, p. 408

2000 K. Bergmann, O. Rosier, W. Neff, R. Lebert, “Pinch-plasma radiation source for extreme-ultraviolet lithography with a kilohertz repetition frequency”, Appl. Opt. 39(22), 3833-3837.

2000 N. Guerineau, B. Harchaoui, J. Primot, “Talbot experiment re-examined: demonstration of an achromatic and continuous self-imaging regime”, Opt. Communications 180, 199–203.

2000 O. Friesch, W. Schleich, and I. Marzoli, “Quantum carpets woven by Wigner functions,” New J. Phys. 2(1), 4.

2000 S. Mcnab, R. Blaikie, “Contrast in the evanescent near field of lambda/20 period gratings for photolithography”, Appl. Optics 39(1) 20-25.

2000 T. R. Jensen, R. P. Van Duyne, S. A. Johnson, V. A. Maroni, “Surface-Enhanced Infrared Spectroscopy: A Comparison of Metal Island Films with Discrete and Nondiscrete Surface Plasmons”, Appl. Spectrosc. 54 (3), 371.

2001 M. Berry, I. Marzoli, W. Schleich, “Quantum carpets, carpets of light”, Physics World, June, 1-6.

2001 T. Kondo, S. Matsuo, S. Juodkazis, H. Misawa, “Femtosecond laser interference technique with diffractive beam splitter for fabrication of three-dimensional photonic crystals”, App. Phys. Letters 79, 725-727.

2001 Y. Liu, M. Seminario, F. G. Tomasel, C. Chang, J. J. Rocca, D. T. Attwood, “Achievement of essentially full spatial coherence in a high-average-power soft-x-ray laser”, Phys. Rev. A 63(3), 033802.

2002 R. A. Bartels, A. Paul, H. Green, H. Kapteyn, M. Murnane, S. Backus, I. Christov, Y. Liu, D. Attwood, C. Jacobsen, “Generation of Spatially Coherent Light at Extreme Ultraviolet Wavelengths”, Science 297, 376-378.

2003 A. Bourdillon, Ch. Boothroyd, G. Williams, Y. Vladimirsky, “Near field x-ray lithography simulations for printing fine bridges”, J. Phys. D: Appl. Phys. 36, 2471.

2003 G. Brooker, “Modern classical optics” Oxford university press.

2003 K. Crozier, A. Sundaramurthy, G. Kino, C. Quate, “Optical antennas: Resonators for local field enhancement”, J. Appl. Phys. 94(7), 4632-4642.

2003 M. Born, E. Wolf, Principles of optics, (Cambridge, UK) p. 515

2003 N. Guerineau, E. Mambro, J. Primot, “Talbot experiment re-examined: study of the chromatic regime and application to spectrometry”, Opt. Express 11(24), 3310-3319.

2003 S. Teng, L. Liu, J. Zu, Z. Luan, D. Liu, “Uniform theory of the Talbot effect with partially coherent light illumination”, J. Opt. Soc. Am. A 20(9) 1747-1754.

2004 E. Mambro, r. Haidar, N. Guerineau, J. Primot, “Sharpness limitations in the projection of thin lines by use of the Talbot experiment”, J. Opt. Soc. Am. A 21(12), 2276-2282.

2004 Y. Nakata, T. Okada, M. Meada, “Lithographical laser ablation using femtosecond laser”, Appl. Phys. A 79, 1481-1483.

2005 A. Bourdillon, Ch. Boothroyd, “Simulations for printing contacts with near field x-rays”, J. Phys. D: Appl. Phys. 38(16), 2947.

2005 A. Lohmann, H. Knuppertz, J. Jahns, “Fractional montgomery effect: a self-imaging phenomenon”, J. Opt. Soc. Am. A 22(8), 1500-1508.

2005 H. Solak, Y. Ekinci, “Achromatic spatial frequency multiplication A method for production of nanometer-scale periodic structures”, J. Vac. Sci. Technol. B 23(6), 2705-2710.

2005 J. Pankert, K. Bergmann, R. Wester, J. Klein, W. Neff, O. Rosier, St. Seiwert, Ch. Smith, S. Probst, D. Vaudrevange, G. Siemons, R. Apetz, J. Jonkers, M. Loeken, Th. Krücken, P. Zink, "EUV Sources for Lithography, edited by V. Bakshi", (Bellingham, SPIE Press, Washington).

2005 L. Wang, H. Solak, Y. Ekinci Y, "Fabrication of high-resolution large-area patterns using EUV interference lithography in a scan-exposure mode", Nanotechnology 23, 305303.

2005 L. Wang, H. Solak, Y. Ekinci, "Fabrication of high-resolution large-area patterns using EUV interference lithography in a scan-exposure mode", Nanotechnology 23, 305303.

2005 P. Muhlschlegel, H.-J. Eisler, O. Martin, B. Hecht, D. Pohl, "Resonant Optical Antennas", Science 308, 1607-1609.

2005 P. Schuck, D. Fromm, A. Sundaramurthy, G. Kino, W. Moerner, "Improving the Mismatch between Light and Nanoscale Objects with Gold Bowtie Nanoantennas", Phys. Rev. Lett. 94(1), 017402.

2005 S. Brueck, "Optical and interferometric lithography nanotechnology enablers", Proc. Of the IEEE 93(10), 1704-1721.

2006 A. Erdmann, P. Evanschitzky, G. Citarella, T. Fuehner, P. Bisschop, "Rigorous Mask Modeling using Waveguide and FDTD Methods: An Assessment for Typical Hyper NA Imaging Problems", Proc. SPIE 6283, 628319.

2006 A. Sundaramurthy, P. Schuck, N. Conley, D. Fromm, G. Kino, W. Moerner, "Toward Nanometer-Scale Optical Photolithography: Utilizing the Near-Field of Bowtie Optical Nanoantennas", Nano Lett. 6(3), 355-360.

2006 E. Cubukcu, E.A. Kort, K.B. Crozier, F. Capasso, "Plasmonic laser antenna", Appl. Phys. Lett. 89, 093120.

2006 E. Ozbay "Plasmonics: Merging Photonics and Electronics at Nanoscale Dimensions", Science 311 (5758), 189–93.

2006 H. C. Rosu, J. P. Trevino, H. Cabrera, J. S. Murguıa, "Self-image Effects in Diffraction and Dispersion", Electromagnetic Phenomena, 6, 2(17), 216-223.

2006 H. H. Solak, "Nanolithography with coherent extreme ultraviolet light", J. Phys. D: Appl. Phys. 39, R171-R188 (2006).

2006 J. G. Huang, J. M. Christian, G. S. McDonald, "Fresnel diffraction and fractal patterns from polygonal apertures", J. Opt. Soc. Am. A, 23(11), 2768-2774.

2006 L. Wang, S.M. Uppuluri, E.X. Jin, X. Xu, "Nanolithography Using High Transmission Nanoscale Bowtie Apertures", Nano Lett, 6(3), 361-364.

2006 S. Danylyuk, R. Panaitov, G. Pickartz, E. Hollmann, S. Vitusevich, A. Belyaev, N. Klein, "Aluminium nitride–niobium multilayers and free-standing structures for MEMS", Thin Solid Films 515, 489-492.

2006 Y. Lu, C. Zhou, S. Wang, B. Wang, "Polarization-dependent Talbot effect", J. Opt. Soc. Am. A 23(9).

2007 A. Poonawala, P. Milanfar, "Mask Design for Optical Microlithography—An Inverse Imaging Problem", IEEE Trans. on Image Processing 16(3), 774 – 788.

2007 A. Ritucci, A. Reale, P. Zuppella, L. Reale, P. Tucceri, "Interference lithography by a soft x-ray laser beam: Nanopatterning on photoresists", J. Appl. Phys. 102, 034313.

2007 B. Meliorisz, A. Erdmann, "Simulation of mask proximity printing", J Micro/Nanolith. MEMs MOEMS 6(2), 023006.

2007 C. Mack, "Fundamental Principles of Optical Lithography: The Science of Microfabrication", John Wiley & Sons Ltd, England.

2007 C. Volkert, A. Minor, Guest editors, "Focused ion beam microscopy and micromachining", MRS Bulletin 32, 389-399.

2007 D. Gruetzmacher, T. Fromherz, C. Dais, J. Stang, E. Mueller, Y. Ekinci, H. Solak, H. Sigg, R. Lechner, E. Wintersberger, S. Birner, V. Holy, G. Bauer, „Three-Dimensional Si/Ge Quantum Dot Crystals", Nano Letters, vol. 7, no. 10, pp. 3150-3156

2007 G. Druart, N. Guérineau, R. Haïdar, J. Primot, P. Chavel, J. Taboury, "Nonparaxial analysis of continuous self-imaging gratings in oblique illumination", J. Opt. Soc. Am. A, 24(10) 3379-3387

2007 M. Dennis, N. Zheludev, F. Abajo, "The plasmon Talbot effect", Opt. Express 15(15) 9692-9700

2007 P. Naulleau, C. Anderson S. Horne, "Extreme ultraviolet interference lithography with incoherent light", Proc. SPIE 6517, 65172T

2007 P. Wachulak, M. Capeluto, M. Marconi, C. Menoni, J. Rocca, "Patterning of nano-scale arrays by table-top extreme ultraviolet laser interferometric lithography", Opt. Express 15, 3465

2007 P. Wachulak, M. Capeluto, M. Marconi, D. Patel, C. Menoni, and J. Rocca, "Nanoscale patterning in high reolution HSQ photoresist by interferometric lithography with tabletop extreme ultraviolet lasers", J. Vac. Sci. Technol. B 25(6), 2094

2007 S. Teng, X. Chen, T. Zhou, C. Cheng, "Quasi-Talbot effect of a grating in the deep Fresnel diffraction region", J. Opt. Soc. Am. A 24(6) 1656-1665.

2007 Wurm S, "Extreme Ultraviolet Lithography Development in the United States", Jpn. J. Appl. Phys. 46(9B) 6105-6112.

2008 A. Anjos, H. Shahbazkia. "Bi-Level Image Thresholding - A Fast Method", BIOSIGNALS 2, 70-76.

2008 F. Neubrech, A. Pucci, T. Cornelius, S. Karim, A. García-Etxarri, J. Aizpurua, "Resonant Plasmonic and Vibrational Coupling in a Tailored Nanoantenna for Infrared Detection", Phys. Rev. Lett. 101(15), 157403.

2008 G. M. Gallatin, P. Naulleau, D. Niakoula, R. Brainard, E. Hassanein, R. Matyi, J. Thackeray, K. Spear, K. Dean, "Resolution, LER and Sensitivity Limitations of Photoresist", Proc. SPIE 6921, 69211E.

2008 H. Shiotani, S. Suzuki, D. Lee, P. Naulleau, Y. Fukushima, R. Ohnishi, T. Watanabe and H. Kinoshita, "Dual Grating Interferometric Lithography for 22-nm Node", Jap. J. Appl. Phys. 47(6), 4881–4885

2008 J. Powell, "The quantum limit to Moore's law", Proc. IEEE 96(8), 1247-1248.

2008 J. Zheng, C. Zhou, B. Wang, "Phase interpretation for polarization-dependent near-field images of high-density gratings", Optics Communications 281, 3254–3259.

2008 P. Stiles, J. Dieringer, N. Shah, R. Duyne, “Surface-enhanced Raman spectroscopy”, Annu. Rev. Anal. Chem. 1, 601.

2008 S. Kim, J. Jin, Y.-J. Kim, I.-Y. Park, Y. Kim, S.-W. Kim, “High-harmonic generation by resonant plasmon field enhancement”, Nature Lett., 453, 757.

2009 A. Isoyan, F. Jiang, Y. C. Cheng and F. Cerrina, P. Wachulak, L. Urbanski, J. Rocca, C. Menoni, and M. Marconi, “Talbot lithography: Self-imaging of complex structures”, J. Vac. Sci. Technol. B 27(6), 2931-2937.

2009 B. Smith, "Design and analysis of a compact EUV interferometric lithography system", J. Micro/Nanolith. MEMS MOEMS 8(2), 021207.

2009 F. Jiang, Y.-C. Cheng, A. Isoyan, F. Cerrina, "Engineering study of extreme ultraviolet interferometric lithography", J. Micro/Nanolith. MEMS MOEMS 8(2), 021203.

2009 K. Bergmann, S. V. Danylyuk, and L. Juschkin : ‘Optimization of a gas discharge plasma source for extreme ultraviolet interference lithography at a wavelength of 11 nm’, J. Appl. Phys., 106, 073309.

2009 K. Lee, S. Yoon, S. Lee, W. Lee, I.. Kim, C. Lee, “Secondary Electron Generation in Electron-beam-irradiated Solids: Resolution Limits to Nanolithography”, J. of the Korean Phys. Soc. 55(4) 1720～1723.

2009 P. Parisse, D. Luciani, A. D'Angelo, S. Santucci, P. Zuppella, P. Tucceri, A. Reale and L. Ottaviano, “Patterning at the nanoscale: Atomic force microscopy and extreme ultraviolet interference lithography”, Materials Science and Engineering: B, 165(3), 227-230.

2009 P. Zuppella, D. Luciani, P. Tucceri, P. Marco, A. Gaudieri, J. Kaiser, L. Ottaviano, S. Santucci, A. Reale“Large area interference lithography using a table-top extreme ultraviolet laser: a systematic study of the degree of mutual coherence”, Nanotechnology 20, 115303.

2009 R. Adato, at al., “Ultra-sensitive vibrational spectroscopy of protein monolayers with plasmonic nanoantenna arrays”, PNAS, 106 (46), 19227.

2009 S. Cherukulappurath, D. Heinis, J. Cesario, N. F. Hulst, S. Enoch, R. Quidant, “Local observation of plasmon focussing in Talbot carpets”, Opt. Express 17(26), 23772-23784.

2009 V. Auzelyte, C. Dais, P. Farquet, D. Grützmacher, L. Heyderman, F. Olliges, C. Padeste, P. Sahoo, T. Thomson, A. Turchanin, C. David, H. Solak, "Extreme ultraviolet interference lithography at the Paul Scherrer Institut", J. Micro/Nanolith. MEMS MOEMS 8(2), 021204.

2009 W. Case, M. Tomandl, S. Deachapunya, M. Arndt, “Realization of optical carpets in the Talbot and Talbot-Lau configurations”, Opt. Express 17(23), 20966-20974.

2010 A. Erdmann, P. Evanschltzky, T. Fuehner, “Mask diffraction analysis and optimization for extreme ultraviolet masks”, J. Micro/Nanolith. MEMS MOEMS 9(1), 013005.

2010 B. Lukyanchuk, N. Zheludev, S. Maier, N. Halas, P. Nordlander, H. Giessen, Ch. Chong, Nature Materials 9 (9), 707.

2010 C. Wagner, N. Harned, “EUV lithography: Lithography gets extreme”, Nature Photonics 4, 24-26.

2010 D. Alessi, D. Martz, Y. Wang, M. Berrill, B. Luther, J. Rocca, “Gain-saturated 10.9 nm tabletop laser operating at 1 Hz repetition rate”, Opt. Letters, 35(3), 414-416.

2010 G. Tallents, E. Wagenaars, G. Pert, “Lithgraphy at EUV wavelengths”, Nat. Photonics 4, 809-811.

2010 H. Levinson, “Principles of Lithography”, (SPIE, Bellingham, Washington).

2010 J. Kim, I. Cho, S. Lee, H. Kang, R. Conley, C. Liu, A. Macrander, D. Noh, “Observation of the Talbot effect using broadband hard x-ray beam”, Opt. Express 18(24) 24975-24982.

2010 J. Schmidt, “Numerical Simulation of Optical Wave Propagation with Examples in MATLAB”, (SPIE Press, Washington).

2010 M. Saib, C. Constancias, P. Michallon, B. Dalzotto, M. Besacier, "Disturbance Effects in Extreme Ultraviolet Interferometric Lithography Affecting Interference Fringes", J. J. Appl. Phys. 49, 06GD04.

2010 P. Wachulak, M. Marconi, C. Menoni, J. Rocca, H. Fiedorowicz, A. Bartnik, "Imaging and Patterning on Nanometer Scale Using Coherent EUV Light", Acta Physica Polonica A 117(2), 403-407.

2010 S. Teng, W. Guo, C. Cheng, "Polarization dependence of the quasi-Talbot effect of the high-density grating", J. Opt. Soc. Am. A 27(3), 366-371.

2010 Y. Fukushima, N. Sakagami, T. Kimura, Y. Kamaji, T. Iguchi, Y. Yamaguchi, M. Tada, T. Harada, T. Watanabe, H. Kinoshita, "Development of extreme ultraviolet interference lithography system", J. J. Appl. Phys. 49, 06GD06.

2010 Y. Fukushima, Y. Yamaguchi, T. Kimura, T. Iguchi, T. Harada, T. Watanabe and H. Kinoshita, "EUV Interference Lithography for 22 nm Node and Below", J. of Photopolymer Sci. and Tech. 23(5), 673-680.

2010 Y. Sonnefraud, N. Verellen, H. Sobhani, G. Vandenbosch, V. Moshchalkov, P. Dorpe, P. Nordlander, S. Maier, “Experimental Realization of Subradiant, Superradiant, and Fano Resonances in Ring/Disk Plasmonic Nanocavities”, ACS Nano 4(3), 1664-1670.

2011 A. Erdmann, F. Shao, V. Agudelo, T. Fühner, P. Evanschitzky, “Modeling of mask diffraction and projection imaging for advanced optical and EUV lithography”, J. Modern Optics 58(5-6), 480-495.

2011 B. Päivänranta, A. Langner, E. Kirk, C. David, Y. Ekinci, "Sub-10 nm patterning using EUV interference lithography", Nanotechnology 22, 375302.

2011 D. Voelz, “Computational Fourier Optics”, SPIE Press, Washington.

2011 H. Solak, C. Dais, F. Clube, "Displacement Talbot lithography: a new method for high-resolution patterning of large areas", Opt Express, 19(11), 10686-10691

2011 I. Wathuthanthri, W. Mao, C.-H. Choi, “Two degrees-of-freedom Lloyd–mirror interferometer for superior pattern coverage area”, Opt. letters 36(9), 1593-1595.

2011 J. G.-Jacob, B. Mills, T. Butcher, R. Chapman, W. Brocklesby, J. Frey, “Gas jet structure influence on

high harmonic generation", Opt. Express 19(10) 9801-9806.
2011 K. Koshelev, M. Mohammad, T. Fito, K. Westra, S. Dew, M. Stepanova, "Comparison between ZEP and PMMA resists for nanoscale electron beam lithography experimentally and by numerical modeling", J. Vac. Sci. Technol. **29**(6), 06F306, 1-9.
2011 L. Novotny, N. van Hulst, "Antennas for light", Nature Photonics 5, 83-90.
2011 L. Urbanski, M. Marconi, A. Isoyan, A. Stein, C. Menoni, J. Rocca, "Analysis of a scheme for de-magnified Talbot lithography", J. Vac. Sci. Technol. B 29(6) 06F504.
2011 T. Urayama, T. Watanabe, Y. Yamaguchi, N. Matsuda, Y. Fukushima, T. Iguchi, T. Harada and H. Kinoshita, "EUV Interference Lithography for 1X nm", J. of Photopolymer Sci. and Tech. 24(2) 153-157.
2012 A. Langner, B. Paivanranta, B. Terhalle and Y. Ekinci, "Fabrication of quasiperiodic nanostructures with EUV interference lithography", Nanotechnology 23, 105303.
2012 K. Okamoto at al., "Effect of Ultrahigh-Density Ionization of Resist Films on Sensitivity Using Extreme-Ultraviolet Free-Electron Laser", Appl. Phys. Express 5, 096701.
2012 L. Urbanski, A. Isoyan, A. Stein, J. Rocca, C. Menoni, M. Marconi, "Defect-tolerant extreme ultraviolet nanoscle printing", Opt. lett. 37(17) 3633-3635.
2012 L. Urbanski, M. Marconi, L. Meng, M. Berrill, O. Guilbaud, A. Klisnick, J. Rocca, "Spectral linewidth of a Ne-like Ar capillary discharge soft-x-ray laser and its dependence on amplification beyond gain saturation", Phys. Rev. A 85(3), 033837.
2012 L. Wang, H. H. Solak and Y. Ekinci, "Fabrication of high-resolution large-area patterns using EUV interference lithography in a scan-exposure mode", Nanotechnology 23,305303.
2012 M. Hofmann, R. Kampmann, S. Sinzinger, "Perturbed Talbot patterns for the measurement of low particle concentrations in fluids", Appl. Optics, 51(10), 1605-1615.
2012 M. Kim, T. Scharf, C. Menzel, C. Rockstuhl, H. Herzig,"Talbot images of wavelength-scale amplitude gratings", Opt. Express 20(5) 4903-4920.
2012 M. Segev, M. Soljačić, J. Dudley, "Fractal optics and beyond", Nature photonics 6, 209-210.
2012 S. Brose, S. Danylyuk, L. Juschkin, C. Dittberner, K. Bergmann, J. Moers, G. Panaitov, St. Trellenkamp, P. Loosen, D. Grützmacher, "Broadband transmission masks, gratings and filters for extreme ultraviolet and soft X-ray lithography", Thin Solid Films 520, 5080–5085.
2012 T. Sato, "High-Order Approximation of the Talbot Distance for Lithography", Appl. Phys. Express 5, 092501.
2012 Y. Hua, J. Suh, W. Zhou, M. Huntington, T. Odom, "Talbot effect beyond the paraxial limit at optical frequencies", Opt. Express 20(13) 14284-14291.
2013 I. Wathuthanthri et al.: Adv. Funct. Mater 23, 608-618.
2013 J. Wen, Y. Zhang, and M. Xiao, "The Talbot effect: recent advances in classical optics, nonlinear optics, and quantum optics", Advances in Optics and Photonics 5(1), 83–130.
2013 J. Wen, Y. Zhang, M. Xiao, "The Talbot effect: recent advances in classical optics, nonlinear optics, and quantum optics", Adv. Opt. Photon. 5(1), 83-130.
2013 R. Peeters, ASML, SPIE Advanced Lithography, San Jose CA, 8679-50.
2013 S Danylyuk, H. Kim, S. Brose, C. Dittberner, P. Loosen, T. Taubner, K. Bergmann, L. Juschkin, "Diffraction-assisted extreme ultraviolet proximity lithography for fabrication of nanophotonic arrays", J. Vac. Sci. Technol. B 31, 021602.
2013 S. Danylyuk, P. Loosen, K. Bergmann, H. Kim and L. Juschkin: 'Scalability limits of Talbot lithography with plasma-based extreme ultraviolet sources', J. Micro/Nanolith. MEMS MOEMS. 12(3), 033002.
2013 The international technology roadmap for semiconductors, "http://www.itrs.net".
2013 W. Li, V. Esquiroz, L. Urbanski, D. Patel, C. Menoni, M. Marconi, A. Stein, W. Chao, E. Anderson, "Defect-free periodic structures using extreme ultraviolet Talbot lithography in a tabletop system", J. Vac. Sci. Technol. B, 31(6) 06F604 (1-7).
2014 H. Kim, W. Li, S. Danylyuk, W. S. Brocklesby, M. Marconi, L. Juschkin, "Fractional Talbot lithography with extreme ultraviolet light", Opt. Letters, 39(24), 6969-6972.
2014 HZB, http://www.helmholtz-berlin.de
2014 J. Chun, S. Jen, K. Petrillo, C. Montgomery, D. Ashworth, M. Neisser, T. Saito, L. Huli, D. Hetzer, "SEMATECH's Cycles of Learning Test for EUV Photoresist and its applications for Process Improvement", Proc. of SPIE 9048(90481Z) 1-15.
2014 N. Mojarad, D. Fan, J. Gobrecht, Y. Ekinci, "Broadband interference lithography at extreme ultraviolet and soft x-ray wavelengths", Opt. Letters 39(8), 2286-2289.
2014 S. Seal, B. Karn, "Safety aspects of nanotechnology based activity",Safety Science 63, 217–225.
2015 K. Miyazaki, G. Miyaji, T. Inoue, "Nanograting formation on metals in air with interfering femtosecond laser pulses", Appl. Phys. Lett. 107, 071103.
2015 N. Mojarad, J. Gobrecht, Y. Ekinci, "Beyond EUV lithography: a comparative study of efficient photoresists performance", Sci. Reports 5, 9235, 1-7.
2015 T. Sato, A. Yamada, T. Suto, R. Inanami, K. Matsuki, S. Ito, "Printability of defects in Talbot lithography." Microelectronic Engineering, 143, 21-24.
2015 W. Karim, S. Tschupp, M. Oezaslan, T. Schmidt, J. Gobrecht, J. Bokhoven, Y. Ekinci, "High-resolution and large-area nanoparticle arrays using EUV interference lithography", Nanoscale, 7, 7386-7393.
Web Henke, X-Ray database, henke.lbl.gov/optical_constants
Web Dowcorning, E-beam Resists, www.dowcorning.com
Web DrLiTHO, www.drlitho.com
Web Zeon, www.zeon.co.jp

Appendix

The Van Cittert-Zernike Theorem

In the case of an extended source, the complex degree of coherence is described by the van Cittert-Zernike theorem. The theorem states the complex degree of coherence between two points in a plane of observation.

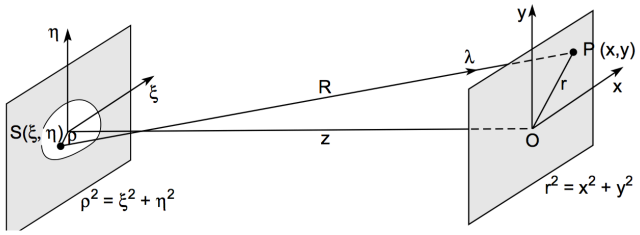

Fig. A1 The geometrical arrangement with the source (ξ, η) and the observation planes (x, y), ρ is radius of the circular disk source.

The normalized degree of coherence measured at two points in a plane of observation (x-y) is given by:

$$\mu_{12} = \frac{\langle E_1(t) \cdot E_2^*(t) \rangle}{\sqrt{\langle |E_1|^2 \rangle} \cdot \sqrt{\langle |E_2|^2 \rangle}} \tag{A1}$$

where μ is mutual coherence degree, E_1 and E_2 are the electric wave fields.

(a) The degree of coherence of a point source (ideal) is reduced to:

$$\mu_{OP} = e^{-i\psi} J_0(0) = e^{-i\psi}. \tag{A2}$$

It describes the correlation between two points (O, P) at the observation plane, where the phase difference $\psi = kr^2/2z = kz\theta^2/2$, $k = 2\pi/\lambda$, $r = (x^2+y^2)^{1/2}$, z is the distance of observation plane from the source plane, θ is the angle measured from the optical axis to the point P, and $J_0(0) = 1$. [1999 Attwood]

(b) The degree of coherence for the source of Gaussian intensity distribution:

$$\mu(\theta) = e^{-i\psi} e^{-(ka\theta)^2/2} \tag{A3}$$

where a is standard deviation of the Gaussian spectrum of the source.

(c) A pinhole illuminated by incoherent source:

$$\mu(\theta) = e^{-i\psi} \frac{2J_1(\nu)}{\nu} \tag{A4}$$

where $J_1(\nu)$ is a Bessel function of the first order where $\nu = ka\theta$, and $\psi = kz\theta^2/2$, which is phase difference.

Characterization of EUV power using CCD

One simple method to characterize the EUV radiation is based on calculating photon number for the known efficiencies of the detection.

$$N_{ph/s} = \frac{S_{CCD} \cdot \sigma}{\eta_{QE} \cdot (E_{ph}/3.65\ eV) \cdot \eta_g \cdot T_f \cdot \eta_R \cdot t_{exp}} \tag{A5}$$

- $N_{ph/s}$: The number of photons per second
- S_{CCD}: counted signal on the detector
- σ: the CCD sensitivity in electrons per count
- η_{QE}: quantum efficiency of the CCD
- E_{ph}: the photon energy in eV (E_{ph}/3.65 eV is the number of electrons released per photon at a band-gap energy of 3.65 eV)
- η_g: the grating diffraction efficiency
- T_f: the filter transmissions
- η_R: reflection coefficient of a SiO_2 surface in case of Lloyd mirror IL
- t_{exp}: exposure time

Fourier integral theorem

$$\begin{aligned} f(t) &= \frac{1}{\sqrt{2\pi}} \int_{-\infty}^{+\infty} g(\omega) e^{-i\omega t}\, d\omega \\ g(\omega) &= \frac{1}{\sqrt{2\pi}} \int_{-\infty}^{+\infty} f(t) e^{i\omega t}\, dt \end{aligned} \tag{A6}$$

Functions f(t) and g(ω) are called Fourier transform and inverse Fourier transform.